Computational and Experimental Investigations of Hemocompatibility in Ventricular Assist Devices

---

Dissertation

zur

Erlangung der naturwissenschaftlichen Doktorwürde
(Dr. sc. nat.)

vorgelegt der

Mathematisch-naturwissenschaftlichen Fakultät

der

Universität Zürich

von

Lena Alexandra Wiegmann

von

Zürich ZH

Promotionskommission

Prof. Dr. Vartan Kurtcuoglu (Leitung der Dissertation und Vorsitz)
Prof. Dr. Max Gassmann
Prof. Dr. Dagmar Iber
Dr. Diane de Zélicourt
PD Dr. Oliver Speer

Zürich, 2018

i.Acknowledgements

First of all, I would like to thank Prof. Dr. Vartan Kurtcuoglu for accepting me as his PhD student, for his guidance, but also the freedom he granted me during my doctoral studies. My gratitude goes to Dr. Diane de Zélicourt for her continuous supervision, support and inspiration. Further, I would like to thank Prof. Dr. Max Gassmann, Prof. Dr. Dagmar Iber and PD Dr. Oliver Speer for serving in my PhD committee and for their helpful suggestions during the committee meetings.

I thank my colleagues at the Interface group for providing a friendly, open and supportive working environment and the entire J-floor and Institute of Physiology for their readiness to help and the insights into very different aspects of research.

Further, I wish to thank my collaborators, without whom this thesis would not have been possible. I thank the pd|z Medtech group for hosting me at their offices and especially Seraina Dual and Stefan Boës for their friendship, encouragement and collaboration. I owe my thanks to the Erythrocyte Laboratory, especially Dr. Julia Eekels and PD Dr. Oliver Speer, and the Hematology Laboratory, especially Séverine Gilloz, at the Kinderspital Zürich for their advice and all the help with my experiments. I also want to thank Andrea Vögeli and Dr. Jeroen Goede from the Kantonsspital Winterthur for helping with the ektacytometry measurements. Further, I would like to thank Brigitte Herzog for her straightforward assistance at numerous instances, Georgios Stefopoulos for his help with the micro-channels and Dr. Thomas Schweizer for the access to and support with the rheometer. I also thank Dr. Bente Thamsen and Dr. Marcus Granegger for sharing their knowledge about VADs, their inputs and help. I would also like to thank Dr. Ivan Cimrak for his excellent support on the cell simulations. In addition, I wish to express my gratitude to all blood donors for my experiments.

Moreover, I want to thank my students, Bettina Gübeli, Cornelia Burri, Alexandra Studer, Kristina Koch and Floni Sadiku, for their motivation and contribution to the project. I was glad to be part of the OctoVAD project team and want to thank the other PhD students and Dr. Gregor Ochsner for their endorsement, friendship and the retreats.

I am very thankful for the financial support provided by the Stavros Niarchos Foundation and the Forschungskredit of the University of Zurich. I would also like to acknowledge the project lead and support by the Zurich Heart consortium and the Hochschulmedizin Zurich.

Finally, I am infinitely grateful for the unconditional love and support by my parents, siblings and Tim, without whom I would not be who I am today.

Zürich, May 2018

Lena Wiegmann

ii.Abstract

While heart failure is a global health burden, patient numbers by far exceed the number of available donor organs and mechanical circulatory support constitutes an important treatment option. Ventricular Assist Devices (VADs) are fully implantable blood pumps and improve patient outcome considerably compared to pharmacologic therapy. However, despite technological advances, patients still suffer from high rates of complications. The main adverse events include infections, bleedings and thromboembolic events, such as strokes and pump thromboses, and severely limit patients' survival and quality of life. Many of these complications are linked to the hemocompatibility of the device, which in turn is closely related to the flow conditions within the VAD.

A characteristic of the flow in VADs are high shear stresses, which occur due to the fast spinning rotor. These supra-physiological shear stresses have been shown to damage blood cellular components, including erythrocytes, platelets and proteins relevant for normal coagulation. Experimental characterization of the shear-mediated damage to blood cells has been a topic of intense research, but the highly dynamic loading patterns in VADs have been a limiting factor. A necessary prerequisite for such experiments is the knowledge about possible confounding factors, such as mechanical damage due to handling and processing in the experimental context. To address this topic, we conducted a study in which we characterized the influence of laboratory procedures on red blood cell damage. The results obtained therein lay the basis for single cell experiments that will enable a thorough quantification of mechanical blood cell damage.

While experimental data are needed to link shear stress levels to biological damage, computational models are necessary to probe the local hemodynamics inside the VAD. Here, we devised a high-resolution computational fluid dynamics framework and applied it to blood pump geometries during the design phase, as well as to the latest clinical VAD. During the development of a new pump, the rotor geometry shall be optimized towards maximal efficiency, while at the same time, hemocompatibility is of critical relevance. In the second here presented study, we therefore systematically investigated the influence of selected design parameters on hemodynamics and hydraulic performance. These results are relevant in view of the conflicting design choices that need to be considered in VADs. In the third part of this thesis, we investigated the flow features inside the Heartmate 3 (Abbott, USA) and interpreted these structures in light of clinical experience. Specifically, we focused on the impact of an automatic speed modulation ('Artificial Pulse') on the flow and compared it to the native cardiac pulsatility.

Overall, this thesis provides insights into flow-related aspects of hemocompatibility relevant for the development of next-generation ventricular assist devices. Aiming at a reduction of the rate of complications, these developments shall ultimately improve patients' quality of life.

iii.Zusammenfassung

Weltweit übersteigt die Zahl der Patienten mit schwerer Herzinsuffizienz die verfügbaren Spenderorgane. Mechanische Herzunterstützungssysteme (engl. Ventricular Assist Devices, VADs) sind implantierbare Blutpumpen, die sich als Alternativtherapie etabliert und die Überlebenswahrscheinlichkeit und Lebensqualität dieser Patienten verglichen zur rein medikamentösen Behandlung stark verbessert haben. Trotz technologischem Fortschritt führen VADs allerdings zu einer Reihe von ernsthaften Komplikationen. Dazu gehören Infektionen, Blutungen, Schlaganfälle und Pumpenthrombosen, die die Lebenserwartung und –qualiät der Patienten stark einschränken. Viele dieser Komplikationen stehen in Zusammenhang mit der Hämokompatibilität der Blutpumpen, die wiederum eng mit den Strömungsbedingungen im Inneren der Geräte verbunden ist.

Charakteristisch für die Strömung in VADs sind durch die schnelle Rotordrehung bedingte hohe Schubspannungen. Diese supra-physiologischen Schubspannungen schädigen diverse Bestandteile des Blutes, insbesondere Erythrozyten, Thrombozyten und Gerinnungsproteine. Schubspannungsinduzierte Blutschädigung wurde schon vielfach experimentell untersucht, dabei stellen jedoch die schnellen Dynamiken in VADs eine grosse Herausforderung dar. Für entsprechende Versuche ist insbesondere das Wissen um mögliche Störfaktoren unabdingbar, zum Beispiel die mechanische Schädigung durch Handhabungs- und Verarbeitungsschritte. Dieses Thema wird in der ersten hier präsentierten Studie behandelt, in der wir den Einfluss von Standard-Laborverfahren auf die Schädigung von roten Blutzellen untersucht haben. Diese Resultate bilden die Grundlage für Experimente an einzelnen Zellen, welche wiederum eine umfangreiche Untersuchung von mechanischer Blutschädigung ermöglichen.

Experimentelle Daten ermöglichen die Quantifizierung des Verhältnisses von Schubspannungen zu biologischem Schaden. Gleichzeitig werden numerische Simulationen benötigt, um die lokalen Strömungs- und Spannungsfelder im Inneren der VADs zu bestimmen. Zu diesem Zweck haben wir ein hochauflösendes numerisches Strömungsmodell entwickelt und in Blutpumpen angewendet. Während der Designphase eines neuen VADs ist das Ziel, die Rotorgeometrie auf maximale Effizienz zu optimieren und gleichzeitig den kritischen Aspekt der Hämokompatibilität zu beachten. In der zweiten hier präsentierten Studie haben wir daher systematisch den Einfluss verschiedener Designparameter auf die Hämodynamik und die hydraulische Leistung untersucht. Diese Ergebnisse sind insbesondere im Hinblick auf die sich teilweise widersprechenden Designentscheidungen in VADs relevant. Im dritten Teil dieser Arbeit haben wir dann die Strömung im Inneren des jüngsten klinisch zugelassenen VADs, dem Heartmate 3 (Abbott, USA), untersucht und im Kontext der klinischen Erfahrungen mit dieser Pumpe interpretiert. Im Besonderen haben wir dabei den Einfluss der eingebauten automatischen Drehzahlregelung, dem sogenannten „künstlichen Puls“, untersucht und mit dem natürlichen Herzzyklus verglichen.

Zusammenfassend werden in dieser Arbeit Einblicke und Erkenntnise über strömungsbedingte Aspekte der Hämokompatiblität im Hinblick auf die Entwicklung der nächsten Generation von mechanischen Herzunterstützungssystemen präsentiert. Langfristig ist das Ziel, die Komplikationsrate deutlich zu reduzieren und so die Lebensqualität der VAD-Patienten entscheidend zu verbessern.

Table of Contents

1 Introduction

1.1 Ventricular assist devices

Heart failure is a global burden affecting approximately 38 million people worldwide [1] and transplantation is the gold standard for end-stage heart failure patients. Since patient numbers by far exceed the number of available donor organs, mechanical circulatory support is the therapy of choice both as a bridge to transplant and as a destination therapy, improving outcome considerably compared to pharmacologic heart failure therapy [2]. Ventricular assist devices (VADs) are blood pumps implanted in the left ventricle and anastomosed to the aorta (left VAD, LVAD) or the right ventricle and the pulmonary artery (right VAD), thus supporting the native pumping function of the heart. Most VADs implanted today are continuous-flow (or rotary) pumps as opposed to pulsatile (or volume-displacement) pumps due to their advantageous clinical performance [3]. Figure 1 illustrates the placement and design of the Heartmate 3 (HM3, Abbott, St. Paul MN, USA) as an example rotary VAD.

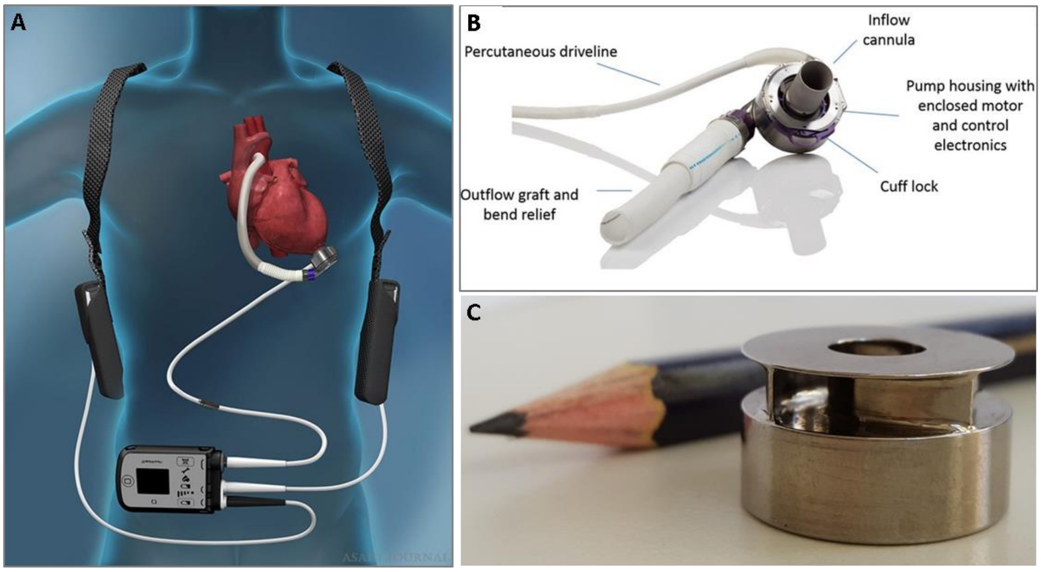

Figure 1: Illustration of placement, peripheral components, full pump and rotor of the Heartmate 3 as an example VAD. A: The inlet of the pump is placed into the left ventricle and anastomosed to the aorta. A percutaneous driveline connects the pump to the controller and battery, which are located outside the body. Reprinted from [4] with permission. B: Implanted components of the Heartmate 3. Reprinted from [4] with permission. C: Impeller of the Heartmate 3. Source: Dr. B. Thamsen, with permission.

Patients eligible for a mechanical circulatory support therapy are usually classified as Class III or IV according to the New York Heart Association (NYHA), which describes symptoms limiting daily activity despite optimal adjustment of therapy with approved medications [5]. To provide additional differentiation and allow optimal patient selection, they are further classified according to their Interagency Registry for Mechanically Assisted Circulatory Support (INTERMACS) profile [5], as listed in Table 1. Based on data collected until 2015, 26% of the VAD patients were listed for transplantation, 23% were on a bridge to candidacy and almost 50% received their pump as a destination therapy [6]. Less common device strategies are bridge to recovery and bridge to decision.

Profile	Description
1	Critical cardiogenic shock, *“crash and burn”*
2	Progressive decline on inotropic support, *“Sliding on inotropes”*
3	Stable but inotrope dependent, *“Dependent stability”*
4	Resting symptoms home on oral therapy
5	Exertion intolerant
6	Exertion limited, *“Walking wounded”*
7	Advanced NYHA Class III symptoms

Table 1: INTERMACS profiles [5]

1.1.1 Selected aspects in VAD design

Continuous-flow VADs can further be subdivided in axial and centrifugal (or radial) pumps, which describes the fluid mechanic design of their rotor. In an axial pump, inlet and outlet of the rotor lie in one axis, and the rotor acts like a propeller in a pipe. In a centrifugal pump, the rotor acts as a spinning disk with blades accelerating blood in a direction tangential to the blade tips. Generally, axial pumps have smaller diameters and require higher rotational speed for the same hydraulic output. Due to their design, centrifugal pumps feature a designated secondary flow path, which refers to fluid surrounding the rotor flowing along the pressure gradient back towards the pump inlet, against the main direction of flow. This phenomenon principally does not occur in axial pumps, even though some backflow is possible [7], and has been shown to increase the overall time required to washout the pump [8].

A crucial component for VAD performance is the rotor bearing. Here, multiple bearing types exist [9]: Pivot bearings facilitate a mechanical support of the impeller, for example through ball-and cup bearings. Their advantages are the low complexity, small size and constant gaps between rotor and housing for all speeds and operating conditions, while disadvantages include problems with wear, potential heat generation and stagnating regions prone for thrombus formation [9]–[11].

Due to these disadvantages, bearing concepts enabling full suspension of the rotor were developed for newer generation VADs. One such example are hydrodynamic bearings, in which the rotor is lifted by hydrodynamic forces in a thin fluid film between rotor and stator. Advantages of such a concept are the absence of contact between surfaces, which precludes life-limiting wear, and their relatively low complexity and high reliability. Disadvantages include the thin fluid film, inside which high forces act on the blood that potentially lead to blood damage. The width of this gap varies based on the operational point, but can become so small that it only fits a few red blood cells [12]. Additionally, rotor and housing are in contact when there is no relative motion, which requires specific surface properties for smooth starting and stopping [9].

A third option are fully magnetic levitation systems, in which the impeller is suspended using active feedback control and electromagnets. The advantages of such a contactless design are likewise the absence of life-limiting wear and additionally the possibility to design relatively large clearance gaps, which reduces the stresses therein. A drawback is the high complexity of such a system, which might require additional approaches to make it fail-safe. For example, electromagnetic levitation systems can be backed up with a hydrodynamic bearing [9].

While the clearance gaps between rotor and housing are to some degree predefined by the bearing system, there is some margin in their design. In their dimensioning, designers face conflicting requirements: small gaps generally increase the hydraulic efficiency by reducing hydraulic losses due to backflow, while large gaps reduce the maximal stresses acting on the blood cells. On the other hand, larger gaps in centrifugal designs increase the secondary flow rate, which exposes more blood to that potentially damaging environment. This topic is further discussed in chapter 3.

For centrifugal pumps, an additional aspect is the design of the impeller, which in VADs is either semi-open or shrouded. Here, “shrouded” refers to a cover plate that is added on top of the blades. Shrouded impellers are advantageous in that they allow for inclusion of rotor magnets, enable large gaps between rotor and housing [13] and separate primary and secondary flows, but at the same time increase the area of interaction between blood and artificial material and pose challenges in manufacturing [14].

Further important geometric aspects in centrifugal pump design are the blade thickness, outlet width, number of blades and blade curvature [14]. Here, the experiences gained with industrial centrifugal pumps can be adopted to find an ‘optimal’ design [15]–[17], bearing in mind that industrial pumps are often used for flows of different orders of magnitude than VADs and without the additional complexity of required biocompatibility.

1.1.2 Complications in VADs

Even though VADs considerably improve patient survival and quality-of-life, they still come with high rates of complications [6]. Generally, the rates of adverse events decrease after the first quarter post implantation and the two most common complications are bleeding and infection. During the first three months post implantation, they occur at a rate of 16.2 and 13.6 events/100 patient months, respectively, while these rates decrease to 4.1 and 4.6 events/100 patient months for the remainder of the first year after implantation [6]. Other serious and frequent complications are cardiac arrhythmias, respiratory failure, strokes and other neurological events, and renal dysfunction.

Infection is often caused by the percutaneous driveline, and has also been linked to a reduced immune response in VAD patients [18]. Nonsurgical bleeding occurs in the form of epistaxis, gastro intestinal (GI) bleeding, bleeding of the mediastinum and thorax, and intracranial hemorrhage [19], of which the high rates of GI bleeding are especially relevant, worrisome and frequently investigated [20], [21]. Bleeding is supposedly linked to shear-mediated damage to platelets and blood proteins [22] and will be discussed in more detail in chapter 1.3.2. Arrhythmias were speculated to be caused by subendocardial ischemia, intrinsic arrhythmogenicity associated with myocyte remodeling and fibrosis, or the effect of intravenous inotropic therapy [23]. Respiratory failure often occurs in the immediate postoperative period and is considered to be caused by the body adapting to the operative stress [24]. The high rates of strokes in VAD patients is a topic under intense research [25]–[27], and survival free of disabling stroke was included in the primary endpoint of the MOMENTUM 3 study, which intended to evaluate safety and effectiveness of the HeartMate 3 [28]. Renal function can improve under VAD therapy due to the improved perfusion, but at the same time, patients regularly develop acute kidney injury after implantation [29], [30].

It was found that the number of strokes during the first three months carried the highest hazard ratio for subsequent mortality [6]. Overall, these complications lead to high readmission rates and impaired quality-of-life. Figure 2 depicts the freedom from a major adverse event, which is below 50% six months post implantation. Altogether, the high occurrence of complications and the substantial impact on patients' lives highlights the need for further improvement both on the technical, i.e. the device itself, and the clinical side of the treatment [31].

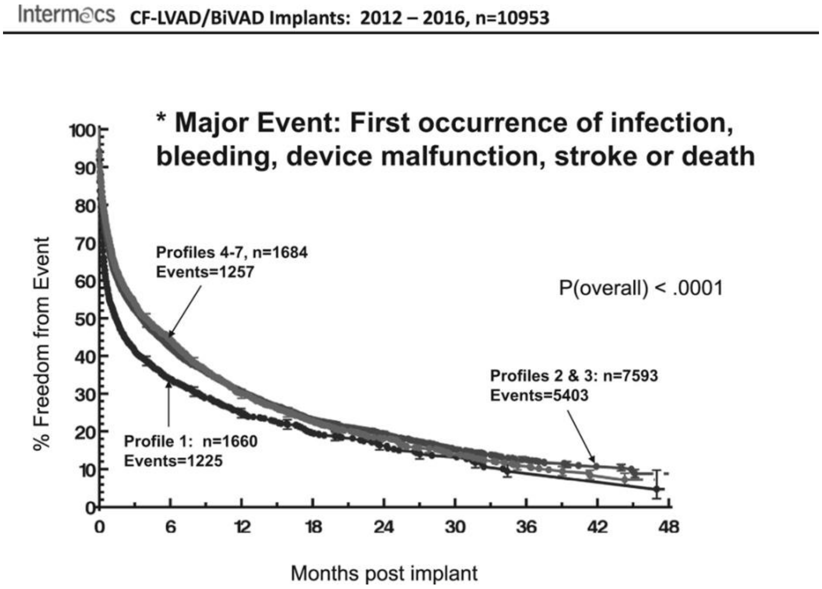

Figure 2: Freedom from the combined major event of first infection, bleeding, device malfunction, stroke, or death. Profiles 1-7 refer to INTERMACS profiles [5], with profile 1 being the most severe condition ("critical cardiogenic shock"). CF-LVAD, continuous flow left ventricular assist device; BiVAD, biventricular assist device. Reprinted from [6] with permission

1.1.3 Selected clinical VADs

The Heartmate II (HMII, Abbott, St. Paul MN, USA) is an axial pump and its internal construction is shown in Figure 3A. Owing to its axial design, there are no dedicated secondary flow paths and the pump speeds are relatively high (up to 15’000 rotations per minute (rpm)). It features pivotal bearings, and is one of the most commonly implanted VADs [11], [32].

The Heartware HVAD (HVAD, Medtronic, Minneapolis MI, USA) is a centrifugal pump with a hydrodynamic axial bearing, enabling a contact-free impeller suspension [33], [34]. Its maximal pump speed is 4000 rpm and the rotor and housing are shown in Figure 3B. The HVAD includes an optional cyclic controlled speed modulation algorithm (‘Lavare Cycle’), during which the rotational speed decreases by 200 rpm, followed by an increase by 400 rpm, before the set speed is retained. This feature lasts for three seconds and is automatically repeated once per minute. It was intended to reduce potential blood stasis by altering left ventricular filling and pump flow [33]. This feature can be controlled by the clinician and is available only in CE- mark countries [35].

The Heartmate 3 (HM3) is the latest FDA-approved VAD and is likewise a centrifugal pump (Figure 3B). In contrast to the HVAD and its predecessor, it is fully magnetically levitated with a so-called MagLev bearing [36]. Its operating speed is between 3000 and 9000 rpm [4]. Similar to the HVAD, it contains an automatic speed modulation. The HM3’s artificial pulse varies the pump speed every two seconds, aimed at a prevention of the formation of zones of recirculation and stasis [4]. During the artificial pulse, the speed is reduced by 2000 rpm, followed by an increase of 4000 rpm. This entire modulation lasts for 350 ms. Additional features of the HM3 are sintered blood-contacting surfaces and relatively wide gaps in comparison to other VADs (~500 µm for the HM3 [4], ~22 µm for the HVAD [12], ~100 µm for the HMII [37]).

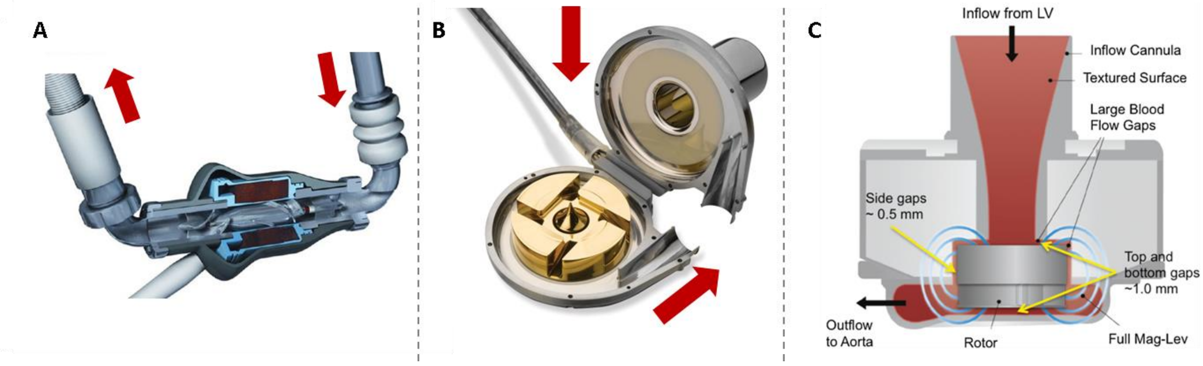

Figure 3: Selected clinical VADs. A: Heartmate II. Blood is entering on the right hand side and leaving towards the aorta on the left hand side, as indicated by the red arrows. Reprinted from [38] with permission. B: Heartware HVAD. Blood is entering through the inflow cannula, which is located axially above the rotor if the pump is closed, and leaves through the radial outlet as indicated by the red arrows. Reprinted from [39] with permission. C: HeartMate 3. Blood flow is indicated with black arrows. Reprinted from [40] with permission.

From a clinical perspective, similarities, but also differences between the devices have been noted. In a comparative study between HMII and HVAD patients, Lalonde et al. found that survival, perioperative bleeding, renal dysfunction, liver dysfunction and infection were similar between the two VADs [41]. Patients with an HVAD implanted however had significantly increased rates of GI bleeding and hemorrhagic strokes. The authors concluded that a refinement in the patient management may be devised [41]. In a multi-institutional analysis, Stulak et al. confirmed the increased incidence of strokes for HVAD patients, but found a higher rate of percutaneous driveline infections in HMII patients [42]. Also, problems with pump thromboses occurred with the HMII [43], [44]. The rate of GI bleeding was similar for the two devices. Within the MOMENTUM 3 study, the HM3's performance was compared to its predecessor, the HMII, and it turned out that the primary endpoint of 2 years survival free of disabling stroke or pump replacement occurred in 79.5% of the HM3 vs. 60.2% of the HMII patients [45]. The HM3 outperformed the HMII in the rate of disabling strokes (10.1% vs 19.2%) and rate of pump thrombosis (1.1% vs. 15.7%), but the rates of death, overall strokes and bleeding were similar for the two pumps.

1.2 Hemocompatibility in VADs

1.2.1 Clinical considerations

Clinically, pre-implant risk factors for increased mortality are higher age, female gender and a more severe condition as specified by the INTERMACS profile [6]. The highest risk of death is associated with the need for a biventricular support and pre-implant dialysis. Interestingly, there is no difference in the time to first pump-related infection, time to stroke and time to first rehospitalization between patients classified with different severity of heart failure [6]. In contrast, in a combination of multiple adverse events, patients in cardiogenic shock at implant were more at risk than patients with INTERMACS levels 2-7 [6].

Multiple of the complications that frequently occur in VAD patients are linked to the hemocompatibility of the pump. These include especially bleedings and strokes, both hemorrhagic and ischemic, but also pump thrombosis and hemolysis. Several aspects are considered to contribute to the blood pump hemocompatibility: The interaction between the pump's artificial material and blood components is one of the three pillars of Virchow's triad for thrombosis [46]. VADs today are mostly manufactured from titanium alloys, which are considered sufficiently biocompatible with concomitantly preferable mechanical properties [47]. Still, titanium is not completely inert and circulating platelet adhesion proteins, such as fibrinogen, can adhere to the artificial material [48], [49]. It has also been shown that contact proteins set off chain reactions that additionally contribute to clot growth [50]. In an attempt to increase hemocompatibility, some devices (such as the HM3) have sintered blood-contacting surfaces, which shall promote the formation of a pseudointima on the luminal surface hindering blood-metal interaction [49].

Further, the interaction of the pump with the ventricle and connecting vessels are important aspects in VAD-related hemocompatibility. As various surgical strategies for VAD implantation exist [51] and patient variability further increases heterogeneity, aspects influencing the interface between the pump and anatomical structures might contribute to clinical outcomes. Both inlet and outlet cannulation influence potential thrombus formation and end-organ perfusion [52]. For example, surgical grafting position was shown to influence wall shear stresses and coronary and cerebral blood flow [53]. The positioning of the inflow cannula was demonstrated to be linked to the functioning aortic valve [54]. Variations in cannula geometry have further been revealed to cause changes in intraventricular flow resulting in different stagnation volumes [55].

The patients' inflammatory state influences the interaction between VAD and native circulation [26]. Heart failure patients were shown to have a-priori increased levels of oxidative stress, which in combination with non-physiological shear in the VAD might be responsible for increased levels of leukocyte activation after implantation [56]. The inflammatory cytokine response was also linked to impaired erythropoiesis in VAD patients [57].

Additionally, VAD patients receive combined anti-coagulation and anti-platelet therapy [58], where the exact protocols depend on the clinical center, device type and patient status.

Naturally, these interventions critically influence bleeding- and thrombosis-related adverse events [59].

Finally, hemocompatibility is impacted by the blood flow features within the VAD itself. Propulsion of blood with a spinning rotor leads to supra-physiological stresses and zones of flow stasis can develop inside the pump. These aspects will be introduced in more detail below.

Overall, while it is undisputed that the occurrence of hemorrhagic and thromboembolic complications is coupled via complex physiological cascades, the detailed mechanisms to date are not yet fully understood [26] and balancing bleeding and clotting is still an ongoing challenge [25].

1.2.2 Mechanistic view – relevance of flow features inside the VAD

Due to the fast spinning rotor (thousands of rotations per minute for centrifugal VADs) and small gaps (as small as 22 µm [12]), shear stress levels in VADs can be in the order of hundreds of Pascal (Pa), which is orders of magnitude above physiological stress values (usually below 7 Pa [60]). These elevated stresses affect erythrocytes, platelets, leucocytes and proteins. For example, high stresses cause rupture of erythrocytes, resulting in hemolysis, with toxic effects on the circulation. Shear-mediated activation of platelets further leads to a procoagulant state. Low-level hemolysis has also been shown to contribute to this procoagulant state, increasing the risk of thrombotic complications [61]. Shear stress also interferes with the coagulation capability of blood by impairing von Willebrand factor (VWF) function [62], [63], which is believed to be linked to the bleeding problems in VAD patients [22], [64].

In turn, a minimum shear stress is necessary to prevent cell aggregation and cell-fibrinogen interaction and thus to allow blood to flow [65], [66]. Stresses below that minimum can occur locally in regions of stagnation and recirculation. Virchow identified blood flow stasis along with vascular endothelial injury and hypercoagulability as the major contributors to thrombosis in his famous triad of thrombosis. VADs may contribute to two of these pro-thrombotic factors by, on the one hand, altering blood composition or blood component functionality and, on the other, giving rise to regions of recirculation or stagnation due to geometric features or operating conditions. Consequently, reduction of these regions of flow detachment has been identified as key optimization objective in the field of blood recirculating devices [67], [68].

Finally, an aspect currently debated is the impact of low pulsatility in centrifugal flow VAD support [69]. In patients with remaining cardiac activity, this pulsatility does not disappear altogether, but is reduced by the VAD depending on the device's design characteristics. This reduced pulsatility in continuous-flow VAD-supported patients has been linked to increased rates of angiodysplasia predisposing patients to gastrointestinal bleedings [20], aortic insufficiency [70] and reduced myocardial recovery [71]. These findings have motivated the development of artificial pulse features [4] and physiologic control algorithms [72].

Accordingly, from a fluid dynamic perspective, challenges in VAD hemocompatibility raise interest mainly in two types of fluid dynamic phenomena within the pump itself: supra-physiological stresses for their damage potential to blood cellular and non-cellular components as well as low flow zones for their role in thrombus formation and growth. The last aspect, decreased pulsatility, is in turn a problem that requires a more global (or full-body) perspective on the hemodynamics.

1.3 Shear-mediated damage

Multiple experimental studies have been performed to shed light on the interplay between stresses and cell injury. This knowledge is the basis for the development of numerical models predicting damage levels.

1.3.1 Red blood cells

Red blood cells (RBCs) constitute the majority of blood cells. They are vital for oxygen delivery to the body tissues, and relevant for multiple other physiological mechanisms [73]–[75]. The mechanical properties of their membranes are central to this function, allowing RBCs to undergo considerable deformations [76] and impaired RBC deformability is relevant in multiple pathological phenotypes [77]. These deformations can be triggered by external stressors, such as the osmotic environment or mechanical forces acting on the membrane [78], [79], and allow RBCs to travel through the smallest capillaries. If, however, these forces exceed the loading capacity of the membrane, pore formation occurs [80] or the membrane completely ruptures [78], thereby releasing all cytosolic content, including hemoglobin, to the plasma. The clinical consequences of hemolysis and extracellular plasma hemoglobin include anemia, hemoglobinuria, dystonias and clotting disorders [81], [82].

Stresses occurring in medical implants, such as artificial heart valves or VADs, often are far beyond the physiological loading levels. Consequently, the reaction of erythrocytes to these stresses has been investigated by multiple groups, often in in-vitro experiments using viscometers or micro-channels [83]–[87]. Experiments suggest that thresholds for RBC rupture and hemolysis depend on exposure time, but are generally above 150 Pa [88]. Still, sublethal damage could occur below these stresses [89].

Yet, even though the relevance of the dynamics of the loading on cells has been recognized already in early experiments [78], [79], so far only few studies exist that quantify the impact of shear magnitudes, frequencies and exposure times independently. Zeng et al. found that there were distinct modes of RBC motion following high shear gradients at the entrance to a constriction [90] and Zhao et al. noticed dynamic responses following high shear gradients warranting further investigations [80]. On a similar line, there are multiple studies on the effect of temporal and spatial gradients on endothelial cells [91]–[94], highlighting the potential impact of dynamic forces on biological cells.

Consequently, there is a need for experimental setups enabling the independent characterization of erythrocyte damage following a range of shear stress magnitudes, gradients and exposure times. Micro-channels could be suited for such an application due to their small size facilitating single cell experiments and their flexibility in geometry allowing for precise control of the stresses acting therein. These experiments require profound knowledge of the baseline conditions, i.e. the mechanical cell damage that could occur during necessary preparation steps for the experiment. Such laboratory procedures frequently include pipetting, mixing and centrifugation procedures, all of which expose cells to mechanical forces. Knowledge about the contribution of these different forces to the measurement endpoints is a necessary prerequisite to the correct interpretation of results. Yet, to date, little data is available addressing this topic.

1.3.2 Platelets and von Willebrand factor

Experiments on stress levels and exposure times critical for platelet activation showed that the critical stresses are generally lower than those for erythrocytes. Early studies identified the relevance of the complex mechanisms involved in shear stress induced platelet signaling, aggregation and adhesion [95], [96] and provided first experimental estimates on their interplay [96]. Later, Ding et al. investigated shear levels between 25 and 350 Pa for exposure times between 39 ms and 1.5 s in a Couette viscometer and identified a power-law based quantitative relationship to platelet activation [97]. In a similar setup, the dynamic component of platelet activation was also investigated [98], [99], notably for smaller stresses (< 7 Pa) and longer exposure times (minutes). After application of triangular and square stress waveforms of varying frequency and duration, resulting platelet activation was larger for higher frequencies, higher stresses and longer exposures [98]. Similarly, Consolo et al. recently identified the high frequency components of shear stress acting on platelets as major determinant of their activation [100]. While platelet activation would lead to an increased clotting risk, high-shear was also found to lead to shedding of platelet surface receptors [101]. The latter could be associated with platelet dysfunction and result in bleeding complications in VAD patients.

The von Willebrand factor (VWF) is a blood protein expressed by vascular endothelial cells and megakaryocytes and essential during normal coagulation [102]. According to clinical findings, VAD patients often suffer from acquired von Willebrand disease, which is linked to bleeding complications, similar to patients with artificial valves implanted [22]. Interestingly, this effect was shown to arise soon after VAD implantation [22], [103], [104], to resolve after device explantation [105], [106] and was not observed in patients receiving a heart transplant [22], [107]. Thus, a close link between the flow in the device and acquired von Willebrand disease seems to exist. As are other blood components, VWF is susceptible to supra-physiological shear stress, which leads to conformational changes and subsequent proteolytic cleavage [108]. This results in a loss of high-molecular-weight multimers of the VWF and finally in decreased VWF-dependent platelet adhesion. Experimental studies quantifying this effect revealed that critical shear levels for VWF damage appear to be even lower than for platelets and erythrocytes [108]–[110].

1.3.3 Mathematical models for shear-mediated blood damage

Experimental studies are the basis for numerical models aimed at predicting expected damage for a certain stress level. In combination with computational models that allow for the quantification of these shear stresses, as introduced in chapter 1.4, these models could be applied to quantify expected damage levels e.g. in a cardiovascular implant.

Giersiepen et al. [111] were the first to suggest the use of power-law based models of the form:

$$D = C \cdot \tau^{\alpha} \cdot t^{\beta} \tag{1}$$

where D is a damage metric, τ is the shear stress, t is exposure time and α, β, C are experimentally derived constants.

Various sets of experimentally determined constants have been published since then, accounting either for hemolysis or platelet activation [97], [99], [112], [113]. In an attempt to model RBC damage, Yeleswarapu et al. suggested the concept of damage accumulation for stresses above a threshold, which reduces to a power law model for constant stress levels [114]. Garon and Farinas later published a method to compute the expected hemolysis as a Eulerian quantity rather than in a Lagrangian formulation to ease comparison to experimental data [115]. Conceptually, a Lagrangian specification follows an individual parcel through space and time, whereas a Eulerian formulation considers a specific spatial location through which the fluid passes over time. Still, these models come with inherent limitations, some of which were discussed in [113]. In contrast to the earlier stress-based models, strain-based approaches were suggested to better reflect the deformation capability of cells. Arora et al. proposed a tensor-based measure based on modelling the deformation of RBCs as neutrally buoyant liquid droplets [116]. This work was later extended to a more realistic representation of the RBC shape [117]. On similar lines, Chen and Sharp presented a strain-threshold based model calibrated with images of deformed cells [118]. A current review of computational hemolysis models is provided in [119].

Mathematical modeling of thrombus formation is more challenging, since it is a multi-physics and multi-scale problem: it describes a coupled problem of flow dynamics, cell and chemical transport, platelet activation, adhesion and cohesion, as well as growth of the resulting thrombus [120]. The spatial scales therein range from millimeters to nanometers, the timescales range from minutes to milliseconds [120]. The isolated aspect of shear-induced platelet activation has been investigated in light of dynamic loading patterns based on the power-law approach [98], [99], [121] and applied to heart valves [122]. Still, these models do not account for a large part of the thrombus formation process, but they do cover the part that may be most relevant in VAD patients. More complex models were published by Goodman et al., coupling fluid flow with chemical processes and including transport of species resulting in sets of convection-diffusion-reactions [123] and similar by Menichini and Xu [65]. Reviews on the multiscale modelling of thrombus formation are provided in [124], [125].

Overall, while the computational models allow for an estimate of expected damage levels, they often fail to actually predict measured values of hemolysis or platelet activation in VADs [98], [126]. Consequently, also prediction of clinical outcomes related to hemocompatibility is still an ongoing challenge. Various reasons might contribute to that situation: Firstly, it was shown that besides stress magnitudes, also its gradients have an impact on cells [100], [127], [128], which the above mentioned models only partly account for. Secondly, experimental studies so far did not address the effect of damage accumulation and relaxation on a larger timescale, referring to repeated exposure to damaging stress regimes while passing through a cardiovascular implant with periods of possible relaxation in between. Furthermore, shear-based models additionally require an adequate prediction of the deformation of cells, which is challenging. Finally, other aspects such as blood-material or cell-cell interaction, physiological compensation mechanisms and patient specificity are not accounted for in these models.

1.4 Computational modelling of blood flow

While experimental studies are needed to understand the biological consequences of stress and other flow features, numerical modelling of the flow fields within the VAD is necessary to identify and quantify these structures in the first place. Computational fluid dynamics (CFD) simulations in general aim at deriving a quantitative description of the velocity and pressure fields in fluid flows. Their governing principles and the application to VADs will be introduced in the following.

1.4.1 Principles of computational fluid dynamics simulations

In CFD simulations, Navier-Stokes equations are solved on discretized grids in space and time. For VADs, the fluid (blood) is typically assumed to be incompressible and Newtonian and external body forces are neglected. Under these assumptions, the Navier-Stokes equations reduce to:

$$\nabla \cdot u = 0 \tag{2}$$

$$\rho \frac{\partial u}{\partial t} + \rho u (\nabla \cdot u) = -\nabla p + \mu \nabla^2 u \tag{3}$$

where ρ is the fluid density, u the fluid velocity, t is time, p is pressure and μ is the dynamic viscosity. Equations (2) and (3) respectively describe the conservation of mass and momentum.

For turbulent flows, a time-averaging of the equations is commonly employed, resulting in the Reynolds-averaged Navier-Stokes equations. Here, the solution is decomposed in a time-averaged (mean) and a fluctuating component. The resulting mass and momentum equations in tensor notation are as follows

$$\frac{\partial \bar{u}_i}{\partial x_i} = 0 \tag{4}$$

$$\rho \frac{\partial \bar{u}_i}{\partial t} + \rho \bar{u}_j \frac{\partial \bar{u}_i}{\partial x_j} = \frac{\partial}{\partial x_j}\left[-p\delta_{ij} + \mu \left(\frac{\partial \bar{u}_i}{\partial x_j} + \frac{\partial \bar{u}_j}{\partial x_i} \right) - \rho \overline{u_i' u_j'} \right] \tag{5}$$

where $\bar{u}$ is the mean fluid velocity, δ_{ij} is the Kronecker delta and *u'* is the fluctuating component of the mean fluid velocity.

The resulting nonlinearity needs to be resolved by modelling the fluctuating part of the velocity as a function of the mean flow. This so called “closure problem” is addressed by the Boussinesq hypothesis, introducing a turbulent eddy viscosity ν_t:

$$-\overline{u_i' u_j'} = -\frac{2}{3} k \delta_{ij} + \nu_t \left(\frac{\partial \bar{u}_i}{\partial x_j} + \frac{\partial \bar{u}_j}{\partial x_i} \right) \tag{6}$$

where k is the turbulent kinetic energy.

There exist a variety of turbulence models, which provide approximations of the turbulent eddy viscosity. Generally, their applicability depends on the specific problem that is to be modelled. For VADs, the k-ω Shear Stress Transport (SST) model by Menter [129] is commonly employed [130], even though no direct measurements of turbulent structures in VADs have yet been published to validate the resulting turbulent flow (see section 1.4.3). In the k-ω SST model, ν_t is modelled as

$$\nu_t = \frac{a_1 k}{\max(a_1 \omega, S F_2)} \tag{7}$$

where ω is the specific dissipation rate, a_1 is a closure coefficient, F_2 is a blending function and S is the mean strain rate tensor.

In a next step, the governing partial differential equations are transformed into a system of algebraic equations to allow their evaluation at discrete locations on a meshed geometry. Here, a common choice is the finite volume method, which formulates divergence terms as surface integrals and is commonly applied in CFD simulations. Details on the resulting equations can be found in [131].

1.4.2 Application of CFD simulations in VADs

CFD simulations are a powerful tool on the path to more hemocompatible VADs since they provide an insight into the flow structures inside the pump under various conditions, which is not generally possible in experiments. CFD analyses further allow for quantitative approximations of velocities, pressures, shear stresses, forces and cell residence times. Even though in principle, experimental methods visualizing and quantifying flow structures do exist [159], [160], the high frequencies necessary to resolve the flow field inside a VAD seriously limit such measurements in rotary blood pumps. Additionally, the non-transparency of the pump itself restricts standard experimental methods, which usually rely on optical measurements. On the contrary, global flow parameters, such as head pressure and mean flow rate, can readily be measured in in-vitro setups as in [161]. The data obtained in these mock-loop measurements is a valuable source for validation of CFD simulations. In contrast to experiments, numerical simulations enable fast iterations of geometry features without the need to fabricate new devices for each geometrical design variation that is to be investigated. On the other hand, CFD analyses of devices as complicated as VADs are computationally expensive, meaning that their execution can take days to weeks on computational clusters of hundreds of CPUs or months on personal computers, which limits their applicability.

1.4.3 Selected modelling aspects relevant for VADs

The main assumptions in equations (2) - (5) are firstly the absence of external body forces, secondly blood being incompressible and thirdly blood being modelled as a single phase Newtonian fluid. While the first two are deemed acceptable, the latter assumption is more critical. In fact, blood clearly has multiple phases, namely the plasma and its cellular contents.

More detailed, the cellular phase could also be divided into the different cell types. Several groups have worked on modelling the cellular phase more accurately, mostly with a focus on red blood cells [132]–[134]. While the simulation of the dynamics of single cells has been accomplished, these models come with clear computational challenges. Replicating physiological hematocrits alone is computationally costly and has so far only been achieved in small geometries such as micro-channels or small tubes [135]. An application to geometries as large and complex as a VAD is still an ongoing challenge and has not yet been published. Given its multi-phase nature, also the modelling of blood as a Newtonian fluid is a simplifying assumption. The suspended erythrocytes cause a non-Newtonian, viscoelastic, shear-thinning behavior. The latter was shown to be caused by the formation of cell aggregates, called rouleaux structures, for low shear rates, which break up in higher shear rates [136], [137]. Thus, the apparent viscosity of blood decreases with increasing shear rate. Important contributors to blood viscosity are also the RBC deformability and, on a macroscopic level, the hematocrit [138]. Depending on the exact situation studied, accounting for the non-Newtonian properties of blood in CFD studies is necessary. Naturally, this is the case for situations dealing with relatively low shear situations, such as in the grafts and connecting vessels of VADs [53], in volume-displacement pumps [139] or in the arterial system [140]. In turn, it has been shown that the non-Newtonian properties of blood become negligible for shear rates larger than 100 s^{-1} [141]. Since shear rates in centrifugal VADs are generally above that value, modelling the fluid as Newtonian is deemed acceptable in these simulations.

Turbulence modelling in VADs has long been under debate and to date, no true measurements of turbulent structures inside a blood pump exist. Since VADs operate in the transitional to low Reynolds number turbulence regime, depending on the device type and operating condition, researchers have either used laminar models or traditional two-equation models [130]. Many studies have applied the k-ε model, in which the transport of the turbulent kinetic energy k and its dissipation rate ε are modelled [142], [143], and have also claimed that it provides the best fit to experimental data [144]. An alternative often employed is the k-ω model, where ω is the specific dissipation rate. A limitation of the k-ω model is its sensitivity to inlet free-stream turbulence properties, which is overcome by the shear stress transport (SST) formulation [145]. The k-ω SST model switches to k-ε behavior in the free stream, and at the same time provides improved solutions over the k-ε model for low Reynolds number flows and boundary layers [130]. It is thus equally applied in many studies using CFD in VADs and was shown to yield better agreement to particle image velocimetry measurements, albeit very rough ones, than the k-ε formulation [146]. Beyond the fluid dynamic effects of turbulence, the biological effect of turbulence on cells is still a matter of debate. While initially it was believed that turbulent Reynolds stresses directly damage blood [147], [148], it was argued that Reynolds stresses are rather a statistical measure than a true stress and thus inappropriate for direct assessment of mechanical load on cells [88], [149]. Topics of ongoing discussion include the questions whether the smallest eddies are indeed the most damaging ones, how viscous stresses on the cell membrane caused by turbulent eddies can be estimated and how the high concentration of cells affects this situation [88], [150]–[152].

Additional important aspects in CFD are spatial and temporal discretization. The solution domain needs to be divided into a finite number of small control volumes, which is then referred to as the "computational mesh". While the computational mesh needs to be fine enough to resolve the relevant flow features, the number of cells directly affects the required computational power. VAD geometries are relatively complex and regions, in which high gradients are expected need to be appropriately refined. These typically include near-wall zones and the blade channels, as well as the small clearance gaps. To ensure that the obtained flow solution is independent of the mesh size, grid independence studies need to be conducted. The use of an inappropriate grid torpedizes efforts to obtain a physically correct solution as it was highlighted by an FDA-initiative, in which experimental measurements were compared to CFD results by various groups for an idealized medical device [153], [154]. Figure 4 illustrates the computational meshes used in chapters 3 and 4 in this thesis as examples for a surface and a (projected) volume mesh.

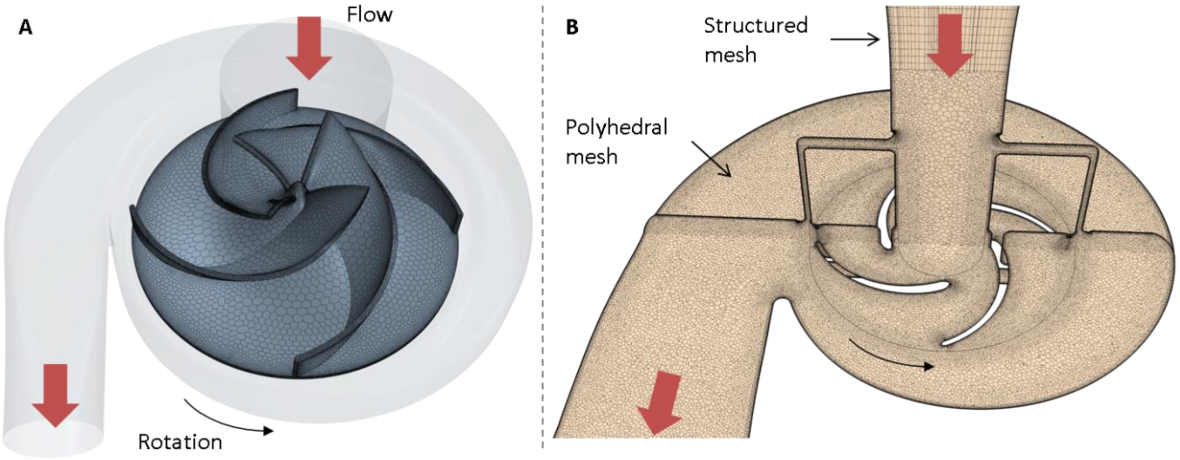

Figure 4: Illustration of computational meshes. A: Surface mesh on the rotor for the generic pump design used in chapter 3. B: Cut planes through the volume mesh of the Heartmate 3 as used in chapter 4. The inlet cannula is meshed in a structured fashion, while the majority of the domain has a polyhedral mesh. Red arrows indicate the flow direction, the black arrows indicate the rotation of the impeller.

Similarly to the spatial grid, a discretization in time is required for unsteady problems as the blood flow in VADs. The time step has to be small enough to capture the relevant dynamics in the flow, while at the same time computational effort needs to be reasonable. In the case of VADs, the fastest dynamics originate from the impeller rotation. Depending on the pump, rotational speed in centrifugal VADs is between 3000 and 8000 rpm. Time steps of approximately 2° of rotation are good practice [155]–[157], corresponding e.g. to $6.67\cdot10^{-5}$ s for a speed of 5000 rpm. Similar to grid independence, the time step independence of the solution is confirmed for each study.

Another aspect of modeling in the context of CFD in VADs is the coupling between fluid flow and rotor position. To date, variations in gap size, as they occur in hydrodynamic and electromagnetic bearings for different operating points, are not accounted for. Even though a coupling would principally be possible and is performed for other cardiovascular implants [99], [158], this was so far neglected in simulations of rotary blood pumps. However, since changes in rotor position result in changes in shear stresses and possibly other flow features, which in turn influence hemocompatibility, accounting for these variations might be necessary in the future.

1.4.4 Current state of research for CFD simulations in VADs

Today, CFD simulations are very commonly applied in the VAD community both for the development of new pumps as well as to explore existing VADs and their behavior [130], [162]. During the design phase, CFD fosters optimization of the geometry and often includes numerical modelling of blood damage as introduced in chapter 1.3.3. For example, Korakianitis and Mozafari et al. made use of the vast knowledge on larger-scale industrial centrifugal pumps and systematically investigated the effect of variations in geometry on hydraulic performance and hemolysis [16], [17]. They found that 5 or 6 blades and a blade outlet angle of 15-35° were optimal considering hydraulic performance and predicted hemolysis. Similarly, Arvand et al. compared different rotor designs in light of their hydraulic and hemolytic properties [13]. Here, the focus was again on the hydraulic and hemolytic properties and three specific impeller designs were compared. Graefe et al. specifically assessed the effect of pump gap sizes on hemolysis [163], while Chan et al. focused on the effect of blade geometry on blood trauma [164]. Automated optimization methods based on CFD have been proposed by Yu et al. for axial blood pumps [165] and similarly also by Wu et al. for hydro turbines, but with potential application to VADs [166]. Besides in studies on generic pump designs, CFD simulations have also been applied to optimize specific geometries, such as for the PediaFlow device (Launchpoint Technologies Inc, Goleta CA, USA) [167]–[169], the Sputnik device (JSC ZITC, Moscow, Russia) [170], [171], the HeartQuest device (Salt Lake City UT, USA) [142], [172] or the EVAHEART (Evaheart Inc, Houston TX, USA) [173].

Application of CFD further enables the investigation of the link between flow patterns and clinically or experimentally observed aspects of hemocompatibility: Fraser et al. assessed mechanical blood damage parameters in three clinical and two investigational VADs using CFD [174], as did Chen et al. [175]. On similar lines, Thamsen et al. investigated the flow fields inside two clinical VADs in light of their hemocompatibility observed clinically [7]. Closely related, the impact of outflow grafting positions of an HVAD on vessel wall shear stress was investigated in [53].

1.4.5 Open questions in CFD simulations in VADs

While CFD per se is well established, there are still multiple aspects warranting further research in the application to VADs. Firstly, blood pumps naturally operate in a highly dynamic environment, including the patient-specific remaining native cardiac pulsatility. Commonly, however, boundary conditions in CFD simulations are prescribed as static, not accounting for the changes in pressures and flow rate during diastole and systole. This is especially relevant for studies investigating pump performance during the design phase, since the VAD will cover a variety of operating points once implanted in the patient, and in light of artificial pulse algorithms implemented in some of the current clinical VADs [4], [35]. This aspect is often insufficiently taken care of, frequently due to restrictions in computational power [176], [177]. Secondly, proper turbulence modelling in VADs is still under debate due to the lack of experimental data as mentioned above [178]. Finally and most importantly, numerical damage models are not yet capable of accurately predicting the different aspects of impaired hemocompatibility in VADs and clearly warrant additional research [26].

1.5 Thesis Objectives

This PhD project aimed at investigating blood pump hemocompatibility from both the experimental and the computational perspective. It was embedded in the *Zurich Heart* Project [179], which is a multidisciplinary research collaboration aiming at the development of technologies for next generation VADs.

To that end, we developed on the one hand a computational framework to probe the local hemodynamics in VADs under physiological operating conditions, and on the other hand conducted in vitro experiments to elucidate and quantify the behavior of erythrocytes under mechanical stress.

On the experimental side, we aimed at an in-depth understanding of RBC mechanical damage in a highly dynamic environment. Experimental setups suitable to investigate that behavior involve preparatory and processing steps and even though these inherently impose mechanical stresses on the cells in focus, little was known about their impact on the experimental endpoints. We aimed to fill this knowledge gap with our study quantifying the mechanical damage of human RBCs by standard laboratory procedures and published it in *Frontiers of Physiology* [180]. It corresponds to chapter 2 of this thesis. We found that centrifuging, vortexing, pipetting and high static pressures influenced markers of mechanical blood damage. These effects should be carefully quantified and taken into account in experimental protocols. This study lays the basis for experiments investigating mechanical RBC damage in dynamic conditions, as they occur in VADs.

On the numerical side, we applied our computational framework to study the effect of design variations on aspects of hemocompatibility and applied it to clinically used VADs. First, we were interested in the utilization of CFD for the systematic optimization of the VAD impeller geometry with respect to hydraulic performance and indicators of hemocompatibility. Thereto, we investigated the influence of selected design parameters of a blood pump in view of their efficiency and hemodynamic characteristics. We utilized a geometry based on an industrial pump design guideline [15] and characterized the effect of alterations in gap sizes, number of blades and shroud design. This work was published in *Annals of Biomedical Engineering* [181] and constitutes chapter 3 of this thesis.

Next, we applied our high-resolution CFD framework to probe the fluid dynamics of the Heartmate 3, the latest clinical VAD. Here, we intended to understand the relation between geometrical and operational features, the resulting flow fields and clinical experience. Specifically, we investigated the effect of the HM3's artificial pulse, and compared it to the native cardiac pulsatility in light of flow conditions relevant for hemocompatibility. With this study, we aimed at generating knowledge that can be employed in the development of next generation VADs and their operational features. This work has been submitted to *Artificial Organs* and corresponds to chapter 4 of this thesis.

Ultimately, the experimental insights shall be combined with the computational framework to accurately predict various types of blood damage associated with a given VAD design. This, we believe, will be a necessary next step in the development of VADs with better hemocompatibility, which in turn will benefit patients' survival and quality of life.

2 Influence of Standard Laboratory Procedures on Measures of Erythrocyte Damage

This chapter has been published as:

Wiegmann L, de Zélicourt DA, Speer O, Muller A, Goede JS, Seifert B and Kurtcuoglu V, „Influence of Standard Laboratory Procedures on Measures of Erythrocyte Damage” *Front. Physiol.*, vol. 8, p. 731, 2017.

2.1 Abstract

The ability to characterize the mechanical properties of erythrocytes is important in clinical and research contexts: to diagnose and monitor hematologic disorders, as well as to optimize the design of cardiovascular implants and blood circulating devices with respect to blood damage. However, investigation of red blood cell (RBC) properties generally involves preparatory and processing steps. Even though these impose mechanical stresses on cells, little is known about their impact on the final measurement results. In this study, we investigated the effect of centrifuging, vortexing, pipetting and high pressures on several markers of mechanical blood damage and RBC membrane properties. Using human venous blood, we analyzed erythrocyte damage by measuring free hemoglobin, phosphatidylserine exposure by flow cytometry, RBC deformability by ektacytometry and the parameters of a complete blood count. We observed increased levels of free hemoglobin for all tested procedures. The release of hemoglobin into plasma depended significantly on the level of stress. Elevated pressures and centrifuging also altered mean cell volume and mean corpuscular hemoglobin, suggesting changes in erythrocyte population and membrane properties. Our results show that the effects of blood handling can significantly influence erythrocyte damage metrics. Careful quantification of this influence as well as other unwanted secondary effects should thus be included in experimental protocols and accounted for in clinical laboratories.

Keywords: Red blood cells, erythrocytes, centrifugation, vortexing, pipetting, free hemoglobin, ektacytometry

2.2 Introduction

Erythrocytes, or red blood cells (RBCs), constitute the majority of blood cellular components and are responsible for the vital transport of oxygen and carbon dioxide throughout the body. The mechanical properties and physical integrity of the erythrocyte plasma membrane are central to this function, allowing RBCs to undergo considerable deformations and travel through the smallest capillaries. In converse, impaired RBC membrane properties and deformability yield severe pathological phenotypes, including sickle cell anemia, spherocytosis, stomatocytosis and elliptocytosis. Beyond hereditary diseases, blood damage is also often an acquired condition due to cardiovascular implants such as artificial heart valves or ventricular assist devices [182], [183]. The ability to characterize RBC mechanical properties is therefore important in both clinical and research contexts: firstly, to diagnose and monitor hematological disorders and, secondly, to understand hemolysis pathways and optimize the design of implantable or extracorporeal devices in order to minimize the induced blood damage.

Mechanical forces acting on RBCs range from those found physiologically in the cardiovascular system to pathophysiological stresses present in implants or during (inappropriate) handling. The range of the cells' reaction naturally also varies from deformation to changes in volume to cell rupture. The essential role in volume homeostasis of Piezo1, a mechanically activated cation channel in the RBC membrane, was recently shown [184]. Activation of Piezo1 due to mechanical loading leads to Ca^{2+} influx, which in turn triggers the dehydration of the cells. This mechanism of volume reduction in response to stress could improve the RBCs' ability to travel through the smallest capillaries [184] and was also hypothesized to promote oxygen/CO_2 exchange in the periphery, which was observed following mechanical stimulation of RBCs [185]. If the stresses acting on the cell exceed its loading capacity, pore formation [80] or complete membrane rupture [78] occurs, and all cytosolic content including hemoglobin is released into the plasma.

In clinical laboratories, several parameters are carefully and specifically analyzed to judge a patient's hematological status. Standardized operating procedures, careful selection of controls and participation in round robin tests ensure a high quality and reproducibility of the results [186]–[188]. At the same time, protocols involve several preparation and intermediate steps, such as pipetting, mixing and centrifuging, which impose mechanical stresses on the cells. Little is known about their influence on the final laboratory results.

This similarly holds true for in vitro experiments for research purposes and the systematic investigation of shear stress effects on cell integrity [80], [189]. To reproduce mechanical stresses in artificial organs such as ventricular assist devices or across artificial heart valves, researchers often rely on in vitro systems such as viscometers or microchannels [83]–[86]. Yet, irrespective of proper control of the shear stress levels within the actual experimental apparatus, these experiments again include handling steps for the preparation of cells, for their placement in the apparatus and for preparation of samples for subsequent analysis. Secondary experimental effects, inherent to the geometric configuration and setup of the apparatus, may also influence the measurement end-points. One such example is the occurrence of high pressures required to drive blood through microchannels. A thorough understanding of the contribution of these different forces to the measurement endpoints is therefore of critical importance for the interpretation of the results and optimization of the laboratory procedures. Still, to date, little literature is available addressing this.

Damage due to centrifugal forces has been demonstrated on different cell lines, but not on erythrocytes [190], [191]. Similarly, the effect of pipetting and elevated pressures was studied on other cell types [93], [192]. Various mixing methods were compared [193], identifying vortexing as the most stress intensive method. However, the induced cell damage was not quantified. For RBCs, the influence of standard laboratory procedures on hemolysis has mostly been studied in the context of transfusion medicine. Delay between collection and separation, large variation in centrifuging speeds, rapid anticoagulation, as well as shaking and mixing were found to yield increased levels of hemolysis in blood bags [194]. Along the lines of testing handling artifacts on RBCs, the effect of different modes of transportation, reflected in variations in anticoagulation and temperature in simulated shipment conditions, was investigated in [195].

While these studies clearly indicate that potentially any handling associated with large forces may be detrimental to cells, it remains unclear to what extent and in what fashion RBCs will incur damage. Next to hemolysis, mechanical stress-induced changes to the plasma membrane deserve attention. Here we address this knowledge gap by investigating the effect of centrifuging, vortexing, pipetting and high pressures on several markers of mechanical blood damage and erythrocyte membrane properties.

2.3 Material and Methods

2.3.1 Subjects

We used venous whole blood of 22 healthy volunteers. Blood was collected with a syringe from a venous catheter (20G) in an antecubital vein. It was anticoagulated either with lithium heparin or ethylenediaminetetraacetic acid (EDTA) depending on the subsequent analysis. The study was approved by the Ethics Commission of the Canton of Zurich, and conformed to the Declaration of Helsinki. Subjects gave written informed consent to participation. The collected samples were randomly assigned to experimental setups and analyses and each donor's blood was used for multiple experiments. Experiments were started immediately after drawing blood and performed at room temperature. The experimental order was randomized and the last experiment was always completed within a maximum of 2 hours of blood draw. Blood awaiting experimental testing was kept at 4°C to minimize changes in hemorheological properties [196]. The analysis procedures as described in 2.3 were initiated right after the end of the experiments and completed within a maximum of 6 hours. The experimental and analysis workflows are explained in the next sections.

2.3.2 Experimental Setups

Figure 5 provides an overview of the experimental setups presented in this study. We investigated the effect of pressure, centrifuging, vortexing and pipetting, and for each one of these four methods tested a range of setup parameters such as stressor magnitude or exposure time. Centrifuging and pipetting are routinely used both in hematology and research laboratories. Although vortexing is usually avoided in RBC handling, it was nevertheless included here to explore the upper bound of applied stresses in a laboratory context. Finally, repeated exposure to pressure plateaus was motivated by the conditions typically experienced by RBCs in experimental microchannel setups. Detailed descriptions of the different experimental conditions are provided in the following subsections.

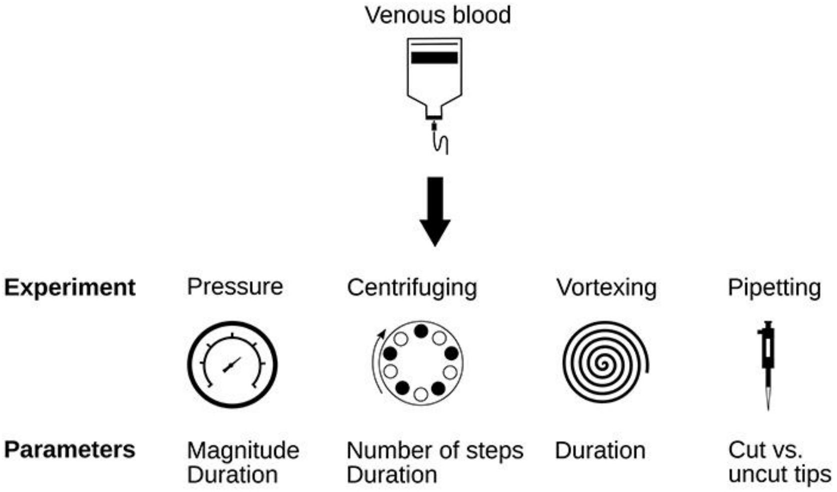

Figure 5: Overview over the experimental setups presented in this study

2.3.2.1 High pressure

In-vitro microchannel setups typically involve repeated cell exposure to high pressures, required to drive the cell suspension through channels and constrictions. To assess the effect of these repeated pressure exposures independently of other forces, notably independently of shear stresses, the samples were exposed to pressure sequences in custom-built pressure chambers driven by compressed nitrogen. A pressure sequence consisted of square pressure waveforms including 10 repeated cycles of high and low pressures. High pressure plateaus (P_{high}) were maintained for a duration T_{high}, where P_{high} was set to either 3, 5 or 7 bars and T_{high} to 1 or 30 seconds for short or long exposures, respectively. T_{high} and P_{high} remained constant within a given experimental sequence. In all sequences, samples were allowed to recover for 30 seconds at low (ambient) pressure between two consecutive high pressure plateaus. Pressure was monitored with a pressure sensor (PBT, Sick AG, Waldkirch, Germany).The number of tested samples is indicated in the respective figure caption in the results section. Controls for this experiment were kept at room temperature in petri dishes (Fisher Scientific, Waltham MA, USA) as used in the pressure chambers for 5 minutes (short exposure experiment) respectively 10 minutes (long exposure experiment).

2.3.2.2 Centrifugation

All centrifugation experiments were performed in the same benchtop centrifuge (Eppendorf Centrifuge 5415D, Eppendorf AG, Hamburg, Germany) at 900g, a centrifuging speed that was chosen according to a diagnostic standard operation procedure at the erythrocyte laboratory, University Children’s Hospital, Zurich. Samples were centrifuged for 5 or 10 consecutive minutes; 1, 2 or 4 times in a row. Energic mixing is required to resuspend the pellet before analysis or the next centrifugation cycle. In these experiments, the samples were vortexed for 2s after each centrifugation. Controls were kept at room temperature in Eppendorf tubes as used in the experiments and vortexed for 2s before analysis. The number of tested samples is indicated in the figure caption in the results section. Per design, comparison of the controls vs. single centrifugation elucidates damage induced by centrifugation only, while comparison against samples centrifuged 2 to 4 times, demonstrates the damage induced by repeated centrifuging and mixing/vortexing cycles (see also Section 4 for in depth discussion).

2.3.2.3 Vortexing

Vortexing was included as representative of extreme stressors on RBCs. Samples were placed into 1.5ml Eppendorf tubes and vortexed once for 20s or 40s in a standard laboratory vortexer (Genie, VWR International, Rednor, USA). The number of tested samples is indicated in the figure caption in the results section. Controls were kept at room temperature in the same Eppendorf tubes without vortexing.

2.3.2.4 Pipetting

To test whether cutting the front end of pipet tips makes pipetting less harmful for red blood cells, we compared samples that were pipetted in and out 10 times in a row with and without cut tip to controls. The repeated exposure was carried out to amplify possible effects on the cells. Pipet tips used were standard 1000 µl tips (Tip One, Starlab, Milton Keynes, United Kingdom). Cut tips were cut 7 mm above the tip end. The number of tested samples is indicated in the figure caption in the results section. Controls were kept at room temperature in the same Eppendorf tubes as used in the experiments.

Naturally, all experiments involved one pipetting step before and after the experiment. It was pursued as gently as possible to keep forces on the cells as low as possible. As a reference, the pipetting rate used in the pipetting experiments was 639 µl/s (51.1 ± 1.1 s for 10 consecutive cycles of pipetting 1000 µl), compared to a rate of 392 µl/s for the gentle pipetting. Since these gentle pipetting steps are also applied on every control sample, the measured differences are not affected.

2.3.3 Analyses

Figure 6 provides an overview of the analyses conducted in this study. We analyzed multiple parameters indicative for mechanical blood damage and RBC membrane properties.

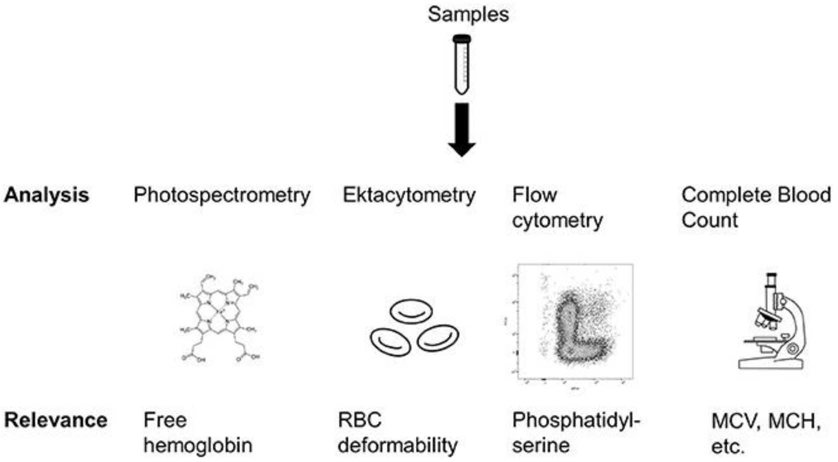

Figure 6: Overview of the analyses performed in this study. Abbreviations: MCV- Mean cell volume, MCH- Mean corpuscular hemoglobin

2.3.3.1 Free hemoglobin

The samples were anticoagulated using lithium heparin. To avoid additional mechanical stresses, plasma separation was not achieved via centrifuging but via sedimentation for 180 min. The sedimentation period was started immediately after finishing the experiments. After separation, the plasma was pipetted gently and frozen at -20°C for later analysis.

Free hemoglobin (Hb) in plasma was measured using photospectrometry at 415 nm, 450 nm and 700 nm and the final Hb concentration was calculated according to [197]:

$$C_{Hb}\,[\text{mg/ml}] = 1.55 \cdot A_{415} - 1.3 \cdot A_{450} - 1.24 \cdot A_{700} \tag{8}$$

The first term represents the known absorption coefficient of hemoglobin, while the second and third term correct for absorption by bilirubin and turbidity. Note that this formulation can yield negative values, which clinically are cut-off and represented by a concentration of 0 mg/ml free hemoglobin. In this study, we kept the original values (whether positive or negative) in order to maintain a valid distribution for subsequent statistical analysis. Triplets of each sample were measured. The reported value corresponds to the arithmetic mean of the three measurements.

2.3.3.2 Ektacytometry

Ektacytometry is currently the most widely used technique for the measurement of RBC deformability [196]. Clinically, it is applied for the diagnosis of several erythrocyte membranopathies, such as hereditary spherocytosis, stomatocytosis and ellipsocytosis. Here, we used this method to detect changes in the general deformation behavior of the cells. In an ektacytometry measurement, EDTA anticoagulated whole blood is mixed with viscous solutions of different osmolalities, and the elongation index (EI) of the red blood cells under constant shear is measured using laser diffraction. The minimal osmolality with measurable EI (Omin) corresponds to the osmotic fragility measured in other applications. All measurements were performed in a Lorrca Maxsis Osmoscan (RR Mechatronics, Hoorn, The Netherlands). Blood samples were analyzed according to the standard protocol for this machine, which involves mixing of the sample in iso-osmolar polyvinylpyrrolidone solution (RR mechatronics) before analysis.

2.3.3.3 Phosphatidylserine expression

Phosphatidylserine is a membrane phospholipid and its externalization a marker for macrophage clearance [198]. Therefore, it is also interpreted as a marker of red blood cell damage [199]. We measured its expression levels using flow cytometry using a protocol similar to the one described in [200].

Normal sample preparation Blood was anticoagulated using lithium heparin. Erythrocytes were labelled using allophycocyanin (APC) anti-human CD235ab antibody staining and PS expression was measured using fluorescein isothiocyanate (FITC) labelled annexin V. All reagents were ordered from BioLegend Europe (London, United Kingdom). Cells were incubated for 20 minutes in complete darkness after mixing 5 µl of APC-CD235ab and FITC-annexin V with 95 µl of annexin binding buffer and 5 µl of whole blood. 400 µl of buffer where then added and everything was mixed using the vortex before the solution was transferred to Falcon polystyrene tubes (Fisher Scientific, Waltham MA, USA), which were prefilled with 500 µl of the same buffer.

Controls We used the following controls: an unstained tube, an APC negative control, a FITC negative control, the two Fluorescence Minus One (FMO) controls and a fully stained control with a 50/50 mixture of normal and PS-positive blood. For the APC negative control, we used a peripheral blood mononuclear cell (PBMC) solution. The unstained control was intended to detect the level of background fluorescence of the system. The FITC negative control contained phosphate buffered saline (PBS) buffer instead of annexin V binding buffer. In the FMOs and the all-in control, we used blood that was prepared to contain an increased amount of PS-positive cells. Details of these protocols are described hereafter.

Preparation of PS-positive blood Blood was treated with *N*-Ethylmaleimide (NEM) (Sigma-Aldrich, St. Louis, Missouri, USA), which inhibits the aminophospholipid translocase, and afterwards mixed with calcium ionophore A23817 (Sigma-Aldrich), to induce membrane lipid scrambling [200]. After washing the cells once with PBS, 10mM NEM buffer solution was added to resuspend the cell pellet. The solution was then incubated for 30min, and afterwards centrifuged for 5 min at 835g to remove the supernatant. After another washing step, the cell pellet was resuspended in 2mM calcium buffer solution and incubated during 3 min at 37°C. 6 µl of 1mM calcium ionophore solution (in DMSO) were then added and incubated during 1 hour at room temperature. Thereafter, the solution was centrifuged for 5 min at 835g to remove the supernatant. The cells were washed once with 2.5mM EDTA buffer solution and three times with cell staining buffer (BioLegend Europe). The cell pellet was then resuspended in 0.3ml PBS and used as what is described here as “PS-positive blood”.

Preparation of PBMCs A solution of peripheral blood mononuclear cells was produced using Ficoll-Paque separation. Whole blood was diluted in 2-4x 2mM EDTA buffer (pH 7.2). For the density gradient centrifugation, 5ml of Ficoll (GE Healthcare, Little Chalfont, United Kingdom) were filled into a 15ml tube, afterwards 7ml of the diluted blood was added. After centrifugation at 800g for 20min, PBMCs were gently pipetted off, washed with PBS and the cell pellet resuspended in PBS.

Flow cytometry The flow cytometric analysis was performed in a BD FACS Canto II (BD Biosciences, Franklin Lakes, New Jersey, USA). In our gating strategy, we initially gated for singlets using forward scatter height vs. width. Afterwards, we selected APC-positive cells (erythrocytes) and, finally, compared the number of FITC-positive cells across samples.

2.3.3.4 Complete Blood Count (CBC)

A routine CBC was conducted using an Advia 2120i system (Siemens Healthcare, Erlangen, Germany) in all samples that also underwent ektacytometry testing.

2.3.4 Statistics

Numerical values are reported as either absolute or normalized by their respective control to account for inter-subject variability. Statistical analyses were conducted using the IBM SPSS Statistics 23 software (IBM Corporation, Armonk, USA). We performed a linear mixed model analysis with the subject as random effect. Post-hoc analysis was according to Tukey-HSD [201] . P-values below 0.05 are considered significant and are indicated in the respective figures.

2.4 Results

2.4.1 Pressure

We exposed the samples to a series of high pressure peaks, lasting 1s or 30s each. Exposure to high pressures significantly increased plasma free hemoglobin (Figure 7A,B). The higher the pressure level, the more hemoglobin was released from the RBCs. While the magnitude of the pressure had a significant effect on free Hb levels, there was no difference between the two exposure times suggesting that the duration of the exposure did not play a major role. Increasing pressures were also associated with a significant decrease in mean cell volume (MCV, Figure 7C). The mean corpuscular hemoglobin (MCH, Figure 7D) decreased with increasing pressure, but this decrease was not statistically significant, while the mean corpuscular hemoglobin concentration (MCHC, Supplementary Figure 1A) stayed constant. Neither the ektacytometric measurement nor the phosphatidylserine expression showed any differences for samples exposed to elevated levels of pressure compared to controls (Supplementary Figure 4A and 8A).

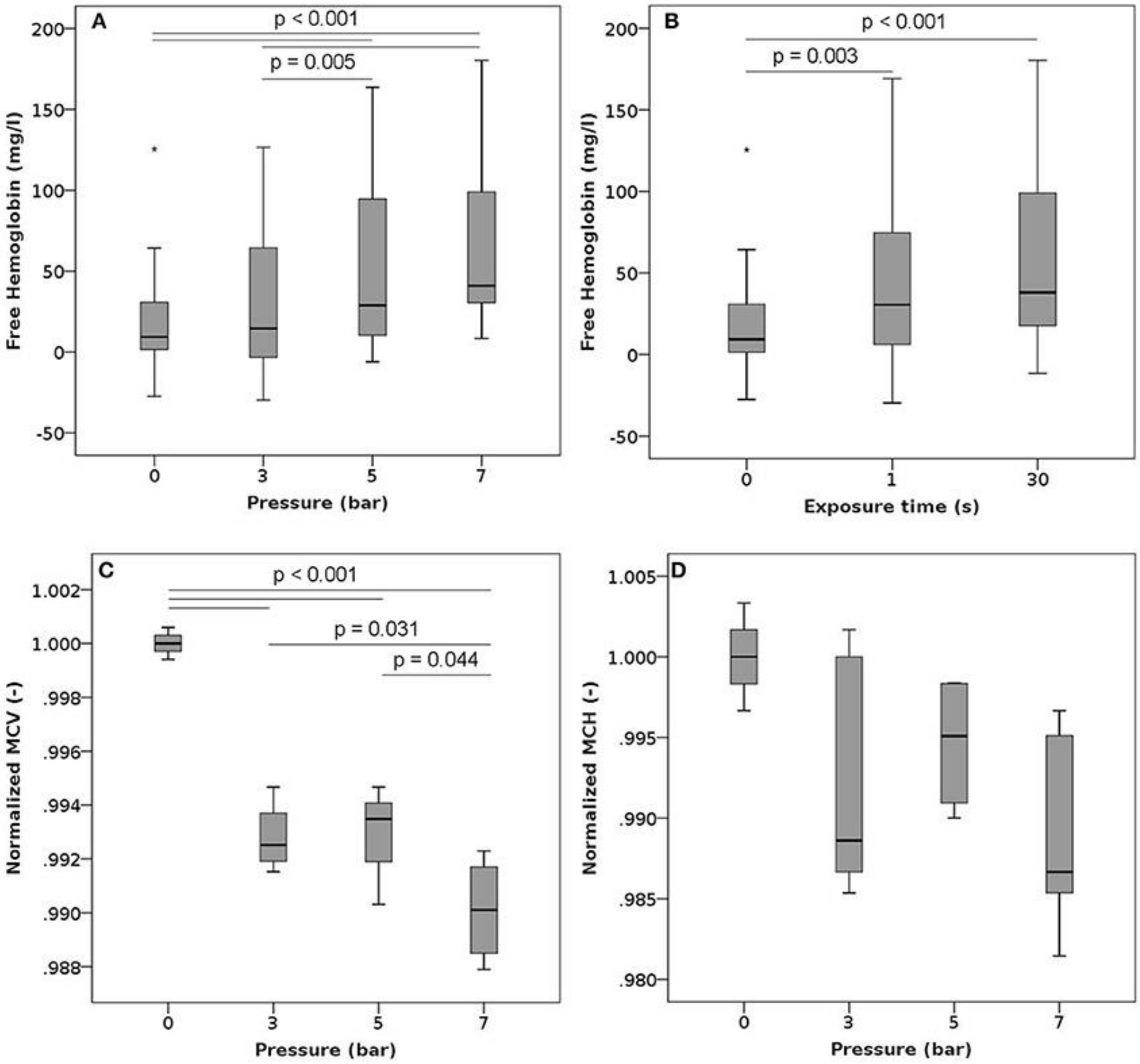

Figure 7: Free hemoglobin, MCV and MCH after exposure to high pressure. Blood samples were exposed to high pressures (varying between 3 and 7 bars) 10 times (single exposure duration of 1 or 30s) with a 30 seconds recovery period between two consecutive exposures. (A): Free hemoglobin as a function of the pressure level (irrespective of the exposure time) n = 18, 22, 20 and 21 for high pressures of 0, 3, 5 and 7 bar, respectively. (B): Free hemoglobin as a function of the exposure duration (irrespective of the pressure level) n = 18, 33 and 30 for exposures of 0, 1 and 30 s, respectively. (C): Normalized mean cell volume as a function of the pressure level (exposure time 1s). Reported values have been normalized by the mean of the corresponding control measurements. n = 4, 4, 3 and 4 for high pressures of 0, 3, 5 and 7 bar, respectively. (D): Normalized mean corpuscular hemoglobin as a function of the pressure level (exposure time 1s). Reported values have been normalized by the mean of the corresponding control measurements. n = 4, 4, 3 and 4 for high pressures of 0, 3, 5 and 7 bar, respectively.

2.4.2 Centrifugation

In these experiments, we centrifuged samples at 900g for either 5 minutes or 10 minutes. Sample centrifugation increased the plasma free hemoglobin from a mean baseline value of 61 mg/l to 79 mg/l (Figure 8A). This behavior was observed for samples centrifuged for 5 minutes as well as for those centrifuged for 10 minutes. Overall, we observed higher absolute free Hb values for samples centrifuged for 5 minutes.

The mean cell volume increased slightly with centrifugation (Figure 8B), while MCH (Figure 8C) and MCHC (Figure 8D) did not change significantly, though showing a trend to increase. Neither phosphatidylserine expression nor parameters measured in ektacytometry were influenced by centrifugation (Supplementary Figure 5B and 8B).

To assess the influence of more than one centrifugation step, the samples had to be resuspended in between centrifugations by a short vortexing step. Consequently, we measured a combined effect of centrifuging and vortexing for these samples. Free Hb increased with an increasing number of centrifugation and resuspension steps (Supplementary Figure 9A), while maximum deformability as measured by ektacytometry, EI_{max}, slightly decreased (Supplementary Figure 9D).

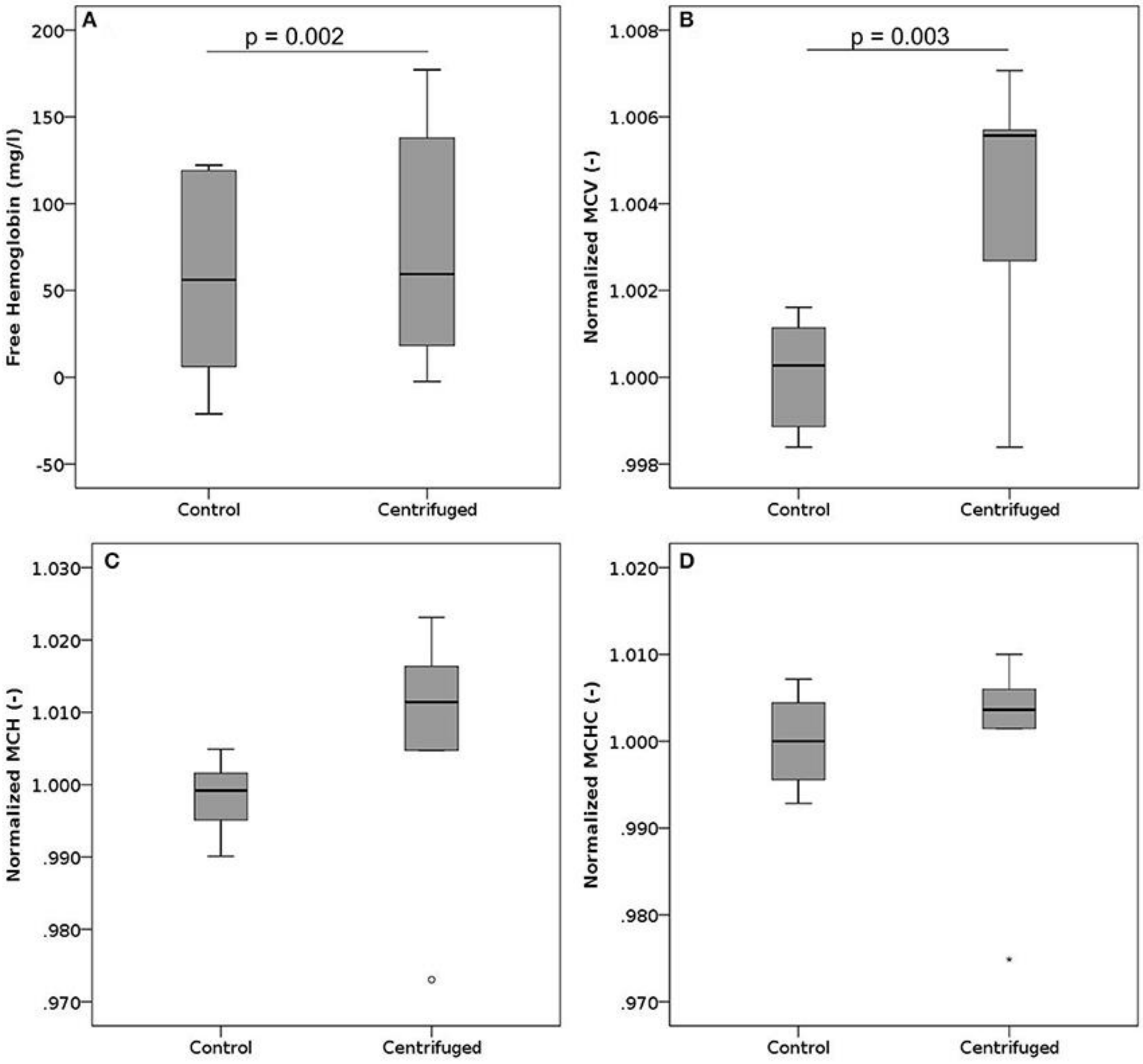

Figure 8: Free hemoglobin, MCV, MCH and MCHC after centrifugation. Blood samples where centrifuged at 900 g . (A): Free hemoglobin after centrifugation for 5 or 10 minutes. The black line indicates the median, while the mean values are 61 mg/l and 79 mg/l for controls and centrifuged samples, respectively. n per group = 12. (B): Normalized mean cell volume after centrifugation for 5 minutes. Reported values have been normalized by the mean of the corresponding control measurements. n per group = 6. (C): Normalized mean corpuscular hemoglobin after centrifugation for 5 minutes. Reported values have been normalized by the mean of the corresponding control measurements. n per group = 6. (D): Normalized mean corpuscular hemoglobin concentration after centrifugation for 5 minutes. Reported values have been normalized by the mean of the corresponding control measurements. n per group = 6.

2.4.3 Vortexing

In these experiments, blood samples were vortexed for either 20 seconds or 40 seconds. Such vortexing led to significant increase in plasma free hemoglobin (Figure 9), resulting in the highest levels of free hemoglobin in plasma observed within this study. This increase in released Hb was strongly dependent on the duration of vortexing. None of the characteristics measured within the complete blood count, ektacytometry and measurement of PS-expression showed any significant changes after vortexing (Supplementary Figure 2, 6 and 8B).

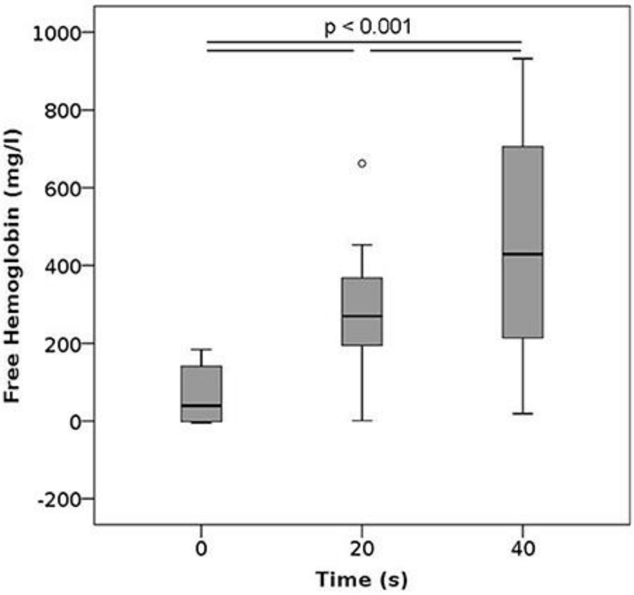

Figure 9: Free hemoglobin after vortexing as a function of the vortexing time. n per group = 12.

2.4.4 Pipetting

To test the effects of pipetting and strategies proposed to potentially moderate them, we pipetted the samples 10 times in a row using either normal or cut pipet tips. Pipetting induced a statistically significant increase in free hemoglobin compared to controls irrespective of the tip used (Figure 10), and there was no difference between samples that were pipetted with normal or cut tips. No changes were noted in the ektacytometry curves, phosphatidylserine expression or in any of the parameters measured within the CBC (Supplementary Figure 3, 7 and 8C).

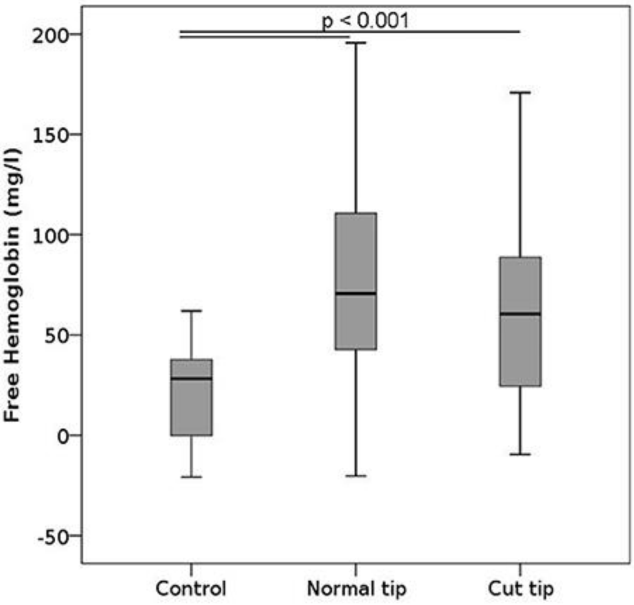

Figure 10: Free hemoglobin after pipetting. Blood samples were primed and relieved from the pipet 10 consecutive times. The pipet tip was either normal or cut 7 mm away from the leading edge. n per group = 12.

2.5 Discussion

While the connection between mechanical forces and hemolysis is well acknowledged, it has mostly been considered in research applications, for example to investigate shear stress-induced hemolysis in cardiovascular implants. However, RBC exposure to supra-physiological forces does not only occur in implants, but also during blood handling. Here we have investigated hemolytic and other stress-induced changes to RBC caused by exposure to high pressures, centrifuging, vortexing and pipetting, thereby surveying the main mechanical stressors in laboratories and experimental blood handling.

Our results show that high pressures, centrifuging, vortexing and pipetting all yield increased levels of free hemoglobin, implying that the forces associated with these methods already translate into hemolytic damage. Among these methods, vortexing whole blood samples led to the highest increase in plasma free hemoglobin, with values reaching a mean of 260 and 400 mg/l after vortexing for 20 and 40 seconds, respectively. Similar findings have been made in orbital shakers, wherein lysis occurred after some time, possibly due to prolonged fatigue [202]. Vortexing as well as shaking impose shear stresses on the cells, which RBCs are generally vulnerable to [85]. Numerical simulations of the flow fields induced by rotators, orbital shakers, magnetic stirrers and vortex mixers identified vortexing as the method that induced the largest shear stresses within the samples [193]. While vortexing RBCs is generally avoided in hematology laboratories, we investigated it here as a representative of extreme stresses on the cells. As evidenced by our results, these stresses are clearly detrimental. Since we did not observe an effect on mean cell volume or MCH, the release of hemoglobin induced by vortexing seems to be governed by complete lysis of the cells, irrespective of their size. Even though vortexing durations of 20 or 40s are long in an experimental context, these results clearly show that vortexing per se is harmful to red blood cells and should be avoided not only in clinical laboratories, but also in research applications.

Pipetting also induces shear forces on the cells, the magnitude of which increases as the pipette tip diameter decreases. Using large pipettes and cutting the foremost edge of the pipette tip to increase the tip diameter had thus been suggested as a means to reduce the stress on cells and mechanical damage [203], [204]. Investigating the effect of repetitive pipetting with standard or cut tips, our results confirmed that pipetting increases free hemoglobin compared to controls, but did not reveal any significant differences between the types of pipette tip used. The suction area of the cut tips was a factor of 14 larger than that of the regular tips, which may not have had a strong enough effect to be detected with our sample size. Alternatively, it is also possible that even though the shear stresses were significantly reduced in the cut pipet tips, the effect on erythrocyte lysis was counterbalanced by the creation of sharper edges. The latter option would point towards the need to round the edges after cutting. However, we do not have enough evidence to favor one interpretation over the other. We thus conclude that pipette tip sectioning does not appear to be effective in reducing pipetting induced hemolysis and may therefore not be a useful addition to the analysis workflow.

In the pressure experiments, plasma hemoglobin increased with higher pressure plateaus, but not with longer exposure times. The recovery pressure and time over which the pressure was varied were constant throughout the experimental conditions. Accordingly, the pressure gradient increased with increasing high pressure levels. Independence from the exposure time may thereby point to the temporal pressure gradients, more than to the absolute pressure values, as the predominant factor for the observed increase in plasma hemoglobin. This hypothesis is in accordance with previous findings in other cell lines. Pressure gradient, and not exposure duration, has been put forth as a primary determinant of epithelial cell damage [93]. The fact that RBCs might be sensitive to pressure gradients thus warrants particular attention in research settings: For example, if high pressures are required to drive blood through a microchannel, then the rate of pressure changes along the channel should be considered in addition to the shear stresses experienced by the cells in the test section.

Our experiments revealed lysis and changes of mechanical properties after centrifuging red blood cells, even though the applied centrifugal force (900g) was at the lower end of the spectrum of commonly used forces in laboratories. This is especially noteworthy given that centrifugation is very commonly performed both in laboratory practice as well as in research experiments in preparatory steps. Between two consecutive centrifuging steps, cells were resuspended with a short vortex period, which is likely to have increased blood damage. Consequently, the results for multiple centrifugation steps reflect a combined effect of centrifuging and resuspension (Supplementary Figure 9). However, since we already observed a statistically significant increase in free hemoglobin between controls and one centrifugation step (mean 61 mg/l to 79 mg/l, $p = 0.002$), with both control and experiment including one vortexing event, it is reasonable to state that centrifugation is by itself a process that induces blood damage. It is difficult to estimate the level of damage induced by experiments published in literature a posteriori, as these often only report the centrifugation speed (rpm) instead of the relative centrifugal forces (rcf), which, without knowledge of the rotor diameter, do not reveal the applied forces [80], [83], [189]. The need to consider such “processing lesions” in addition to the well-known storage lesions was already pointed out by Urbina et al. who noted that the centrifuging performed to extract erythrocyte concentrate from whole blood donations changed RBC shape and MCH [205].

We also observed overall higher values of free hemoglobin for samples centrifuged for 5 minutes compared to those centrifuged for 10 minutes. This may be due to an unintended bias towards male subjects in these samples (100% male subjects in samples selected for the 5 mins centrifuging steps vs. 25% male subjects for the samples selected for 10 mins). It is known that females have 80% more young RBCs and 85% fewer old RBCs than males [206], and that old RBCs have a significantly increased mechanical fragility and rigidity compared to young ones [207]. Older RBCs are thus more susceptible to damage, which may explain the higher values of plasma free Hb noted in the 5 minutes, males-only, group. We also observed an increased amount of PS-positive cells in this subject group, which supports this interpretation. The results shown for the other experimental procedures (pressure, pipetting, vortexing) were not affected by this sex bias, since the study used a paired design wherein the blood from each donor was exposed to all tested conditions, including control.

Vortexing and pipetting did not yield any notable changes in the ektacytometry curves, phosphatidylserine expression or in any of the parameters measured within the CBC

(Supplementary Figure 2-3 and 6-8). For pipetting, this absence of notable changes may be explained by the relatively low overall damage level that was measured. However, this does not hold true for vortexing, which induced significantly elevated levels of plasma hemoglobin. This may suggest that the noted cell damage resulted from complete cell lysis affecting RBCs uniformly, irrespective of their size and age.

In contrast to the above, centrifuging and elevated pressures were also associated with changes in RBC properties (Figure 7 and Figure 8). Centrifuging induced a subtle increase in mean cellular volume, pointing at a destruction of older and smaller RBCs. Also, the maximum deformability decreased with an increasing number of combined resuspension and centrifuging steps Supplementary Figure 9D), a behavior that was not observed in the experiments solely involving vortexing (Supplementary Figure 6D). While the magnitude of the noted changes in mean cellular volume and maximum deformability remained small, these two observations combined are of relevance for both clinical laboratories and researchers: they suggest that even if the remaining cells maintain sufficient membrane integrity not to release significant amounts of intracellular hemoglobin, their mechanical properties may still be altered by repeated centrifugation and resuspension. This finding is also supported by Urbina et al. who observed significant morphological changes, including the appearance of abnormal shapes (echinocytes), after centrifugation [205].

Elevated pressures, on the other hand, led to a decrease of mean RBC volume, a trend towards decreasing MCH and constant MCHC compared to controls. One possible interpretation of the decrease in volume may be the destruction of larger cells. This would be in contrast to previous reports that suggested that mechanical stresses, albeit mostly shear stresses, would affect smaller, older cells first and thus lead to increased MCV [208]. Alternatively, this observed cell shrinkage could also point towards a channel-mediated loss of cytosolic content due to the mechanical load [184]. Since we also observed increased levels of plasma free Hb, it could be hypothesized that the weaker cells suffer from complete lysis, while the remainder of the RBC population reacts with cell shrinkage following Ca^{2+} influx [209]. Otherwise, high pressures have been noted to alter the permeability of the bilayer cell membrane [210], such that cytosolic content, including hemoglobin, could be released into the plasma without full cell lysis. Compared to the conditions explored here, those experiments were conducted at extreme pressure levels (250-1500 bar). Yet, the simultaneous reduction in corpuscular volume and increase in free Hb observed in our pressure experiments could hint at a similar mechanism.

From a clinical perspective, one limitation of this study is the sole investigation of hematologically healthy patients. It might be of interest to characterize whether RBCs with known membrane alterations, such as in patients with sickle cell disease or hereditary spherocytosis, react differently to the same levels of centrifuging, vortexing and pipetting. Determining whether or not different RBC properties are associated with different reactions to standard procedures would be of relevance for the diagnosis workup, as this could interfere with correct interpretation of results and introduce a bias in the comparison of a given patient’s hematological characteristics against standard healthy values. From an experimental perspective, a limitation of this study is the limited applicability of quantitative results to other experimental protocols or setups. This study should thus primarily raise awareness that both preparatory steps as well as secondary factors inherent to an experimental setup should be systematically checked for their influence on the selected study endpoints. Finally, given the small magnitude of the noted changes in CBC parameters, one should also carefully consider potential artifacts introduced by the measurement method. The Advia hematology system uses optical scattering as working principle. We confirmed the trends of increasing MCV after centrifuging and decreasing MCV after exposure to high pressures also in an impedance-based system (Sysmex NX-100, Sysmex K.K., Kobe, Japan), indicating that the noted differences in MCV, although arguably small, were not artefactual. However, manual analysis may be needed for a conclusive answer.

2.6 Conclusion

Within a standard laboratory workflow, there are multiple steps that expose cells to mechanical stress. Here, we investigated the effect of centrifuging, vortexing, pipetting and pressure on human red blood cells. All procedures significantly increased the free hemoglobin in plasma, the measured hemolysis increasing with the vortexing time or the applied pressure. Elevated pressures and centrifugation also altered mean cell volume and mean corpuscular hemoglobin. Careful quantification of the influence of these steps as well as of other unwanted secondary effects should be included in experimental protocols and should be checked for in clinical laboratories.

2.7 Supplementary Material

2.7.1 Results of Complete Blood Count

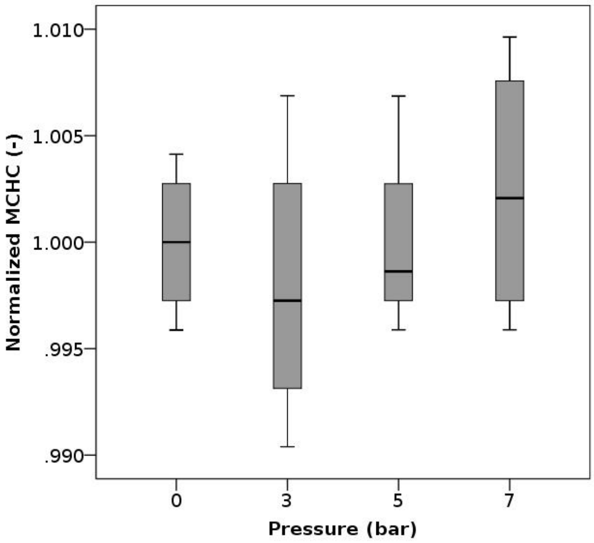

Supplementary Figure 1: Normalized mean corpuscular hemoglobin concentration as a function of the pressure level after exposure to high pressure. Blood samples were exposed to high pressures 10 times (single exposure duration of 1 s) with a 30 s recovery period between two consecutive exposures. Reported values have been normalized by the mean of the corresponding control measurements. n = 4, 4, 3, 4 for high pressures of 0, 3, 5, and 7 bar, respectively.

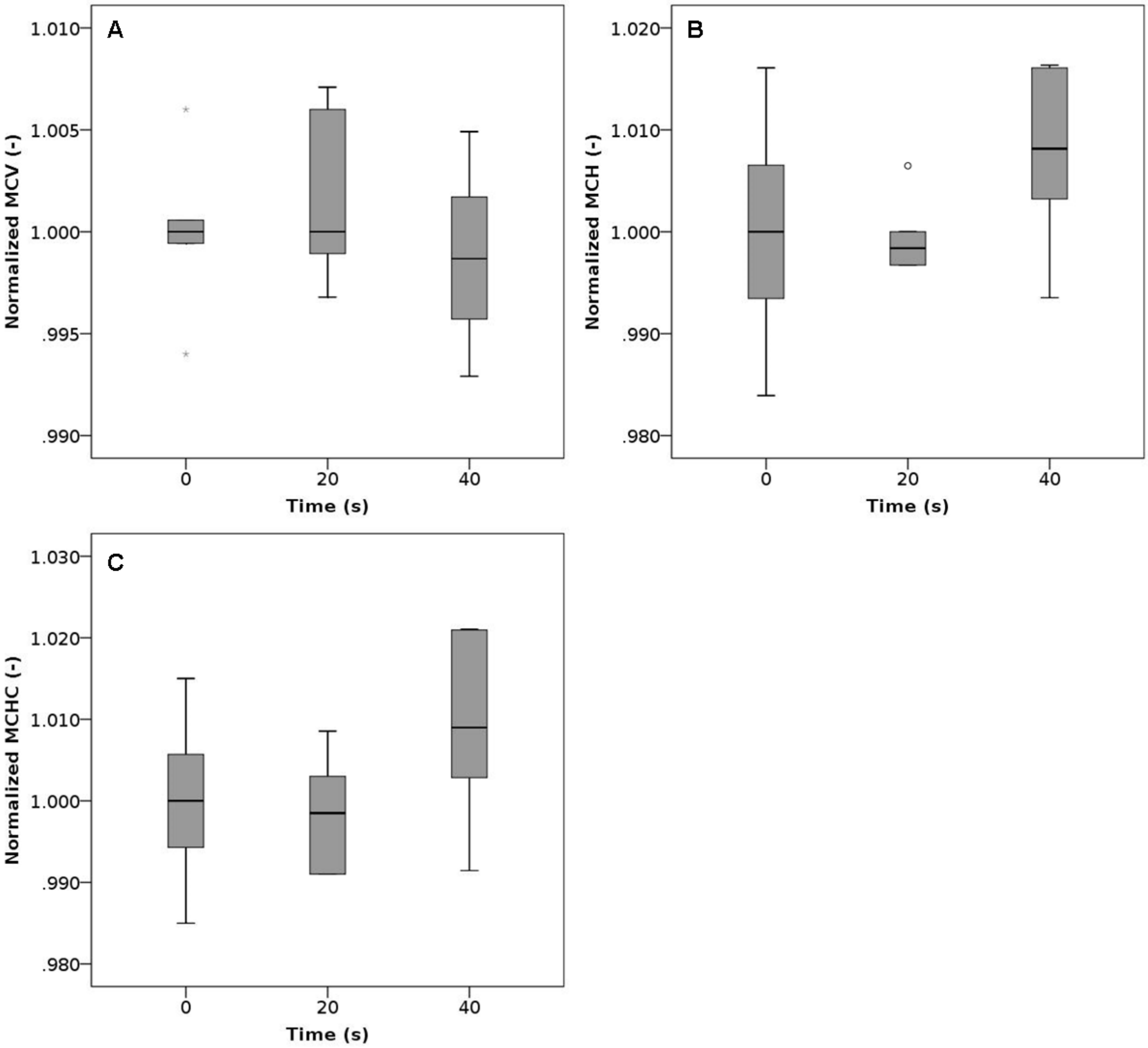

Supplementary Figure 2: Results of complete blood count after vortexing. (A): Normalized mean cell volume as a function of the vortexing time. (B): Normalized mean corpuscular hemoglobin as a function of the vortexing time. (C): Normalized mean corpuscular hemoglobin concentration as a function of the vortexing time. Reported values have been normalized by the mean of the corresponding control measurements. n per group = 6, for all graphs.

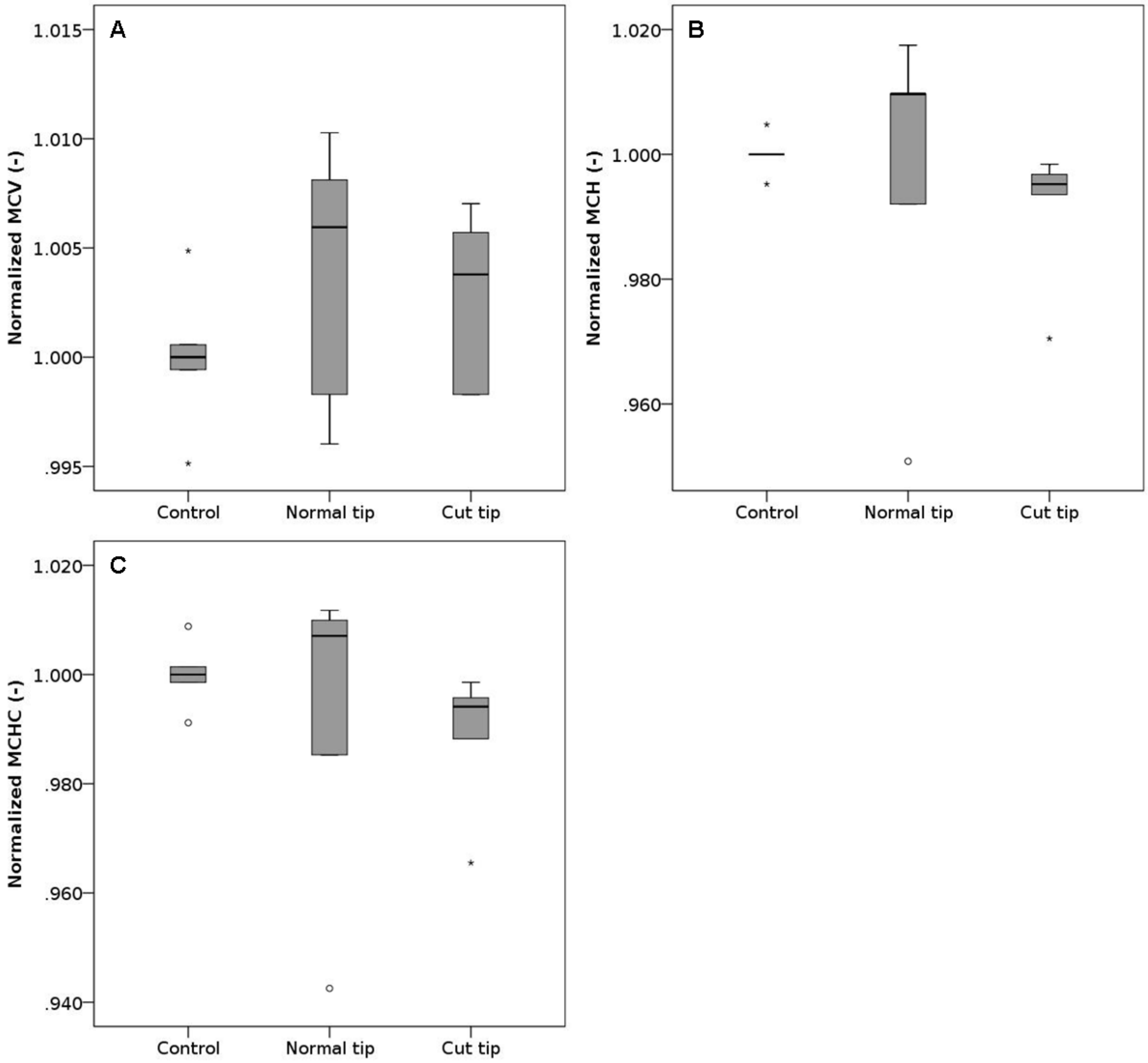

Supplementary Figure 3: Results of complete blood count after 10 times pipetting using normal or cut tips. (A): Normalized mean cell volume. (B): Normalized mean corpuscular hemoglobin. (C): Normalized mean corpuscular hemoglobin concentration. Reported values have been normalized by the mean of the corresponding control measurements. n per group = 5, for all graphs.

2.7.2 Results of ektacytometry measurements

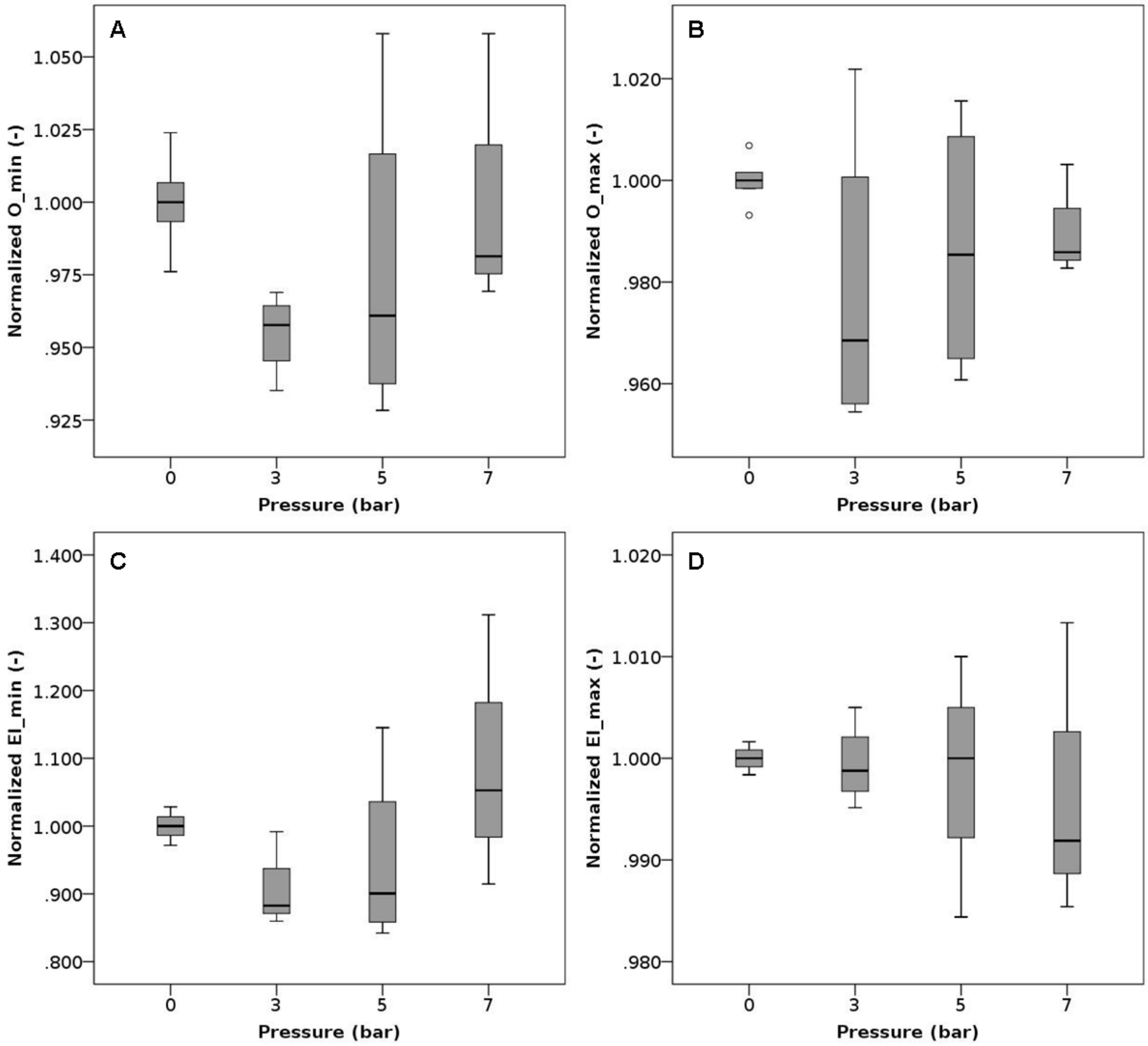

Supplementary Figure 4: Results of ektacytometry measurements after exposure to high pressure. Blood samples were exposed to high pressures 10 times (single exposure duration of 1 s) with a 30 s recovery period between two consecutive exposures. (A): Normalized Omin as a function of the pressure level. Omin is the osmolality at which the minimal elongation index EImin is measured. (B): Normalized Omax as a function of the pressure level. Omax is the osmolality at which the maximal elongation index EImax is measured (C): Normalized minimal elongation index EImin as a function of the pressure level. (D): Normalized maximal elongation index EImax as a function of the pressure level. Reported values have been normalized by the mean of the corresponding control measurements. n = 5, 4, 4, 3 for high pressures of 0, 3, 5, 7 bar respectively, for all graphs.

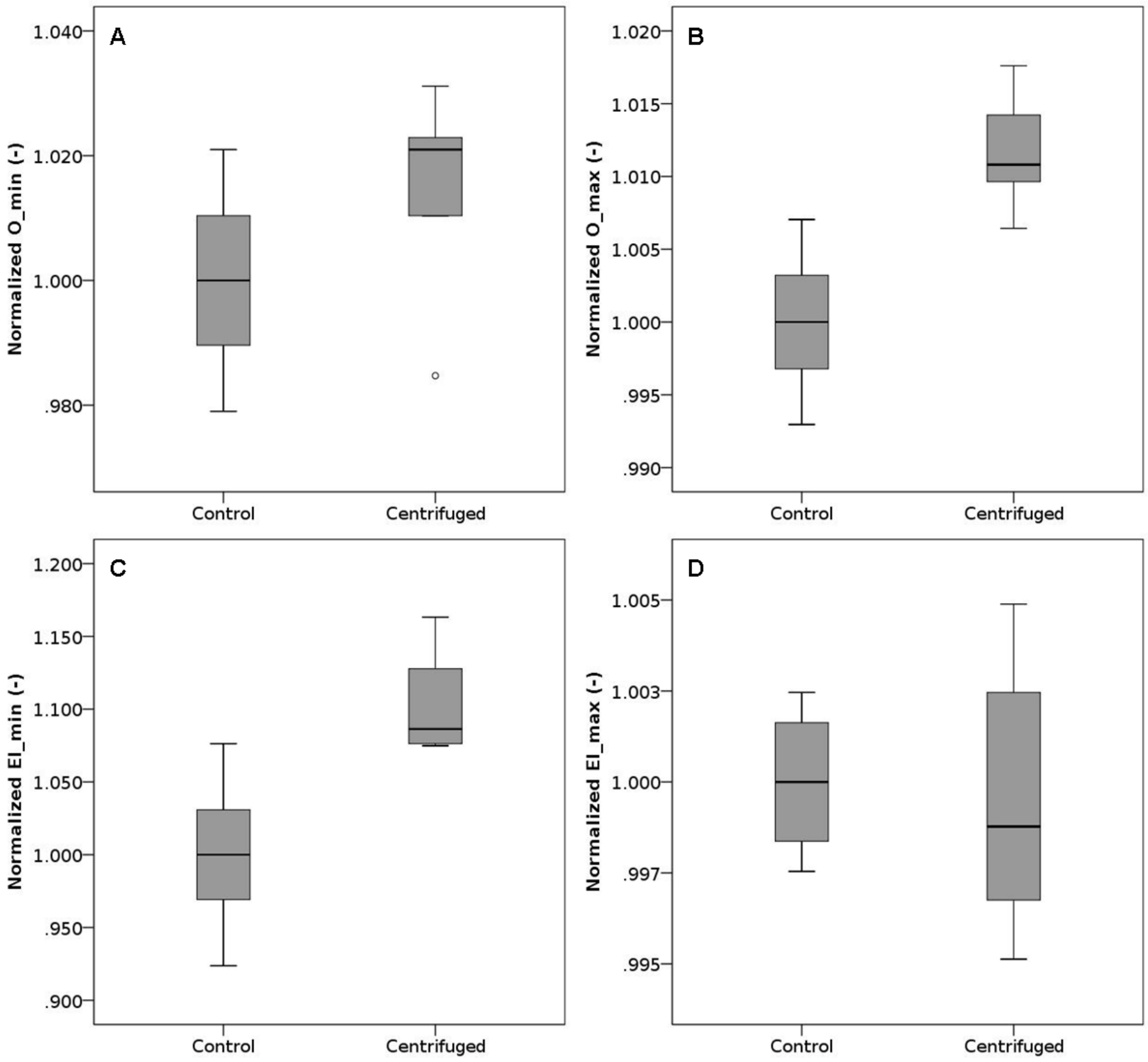

Supplementary Figure 5: Results of ektacytometry measurements after centrifugation at 900g for 5 minutes. (A): Normalized Omin. Omin is the osmolality at which the minimal elongation index EImin is measured. (B): Normalized Omax. Omax is the osmolality at which the maximal elongation index EImax is measured (C): Normalized minimal elongation index EImin. (D): Normalized maximal elongation index EImax. Reported values have been normalized by the mean of the corresponding control measurements. n per group = 6, for all graphs.

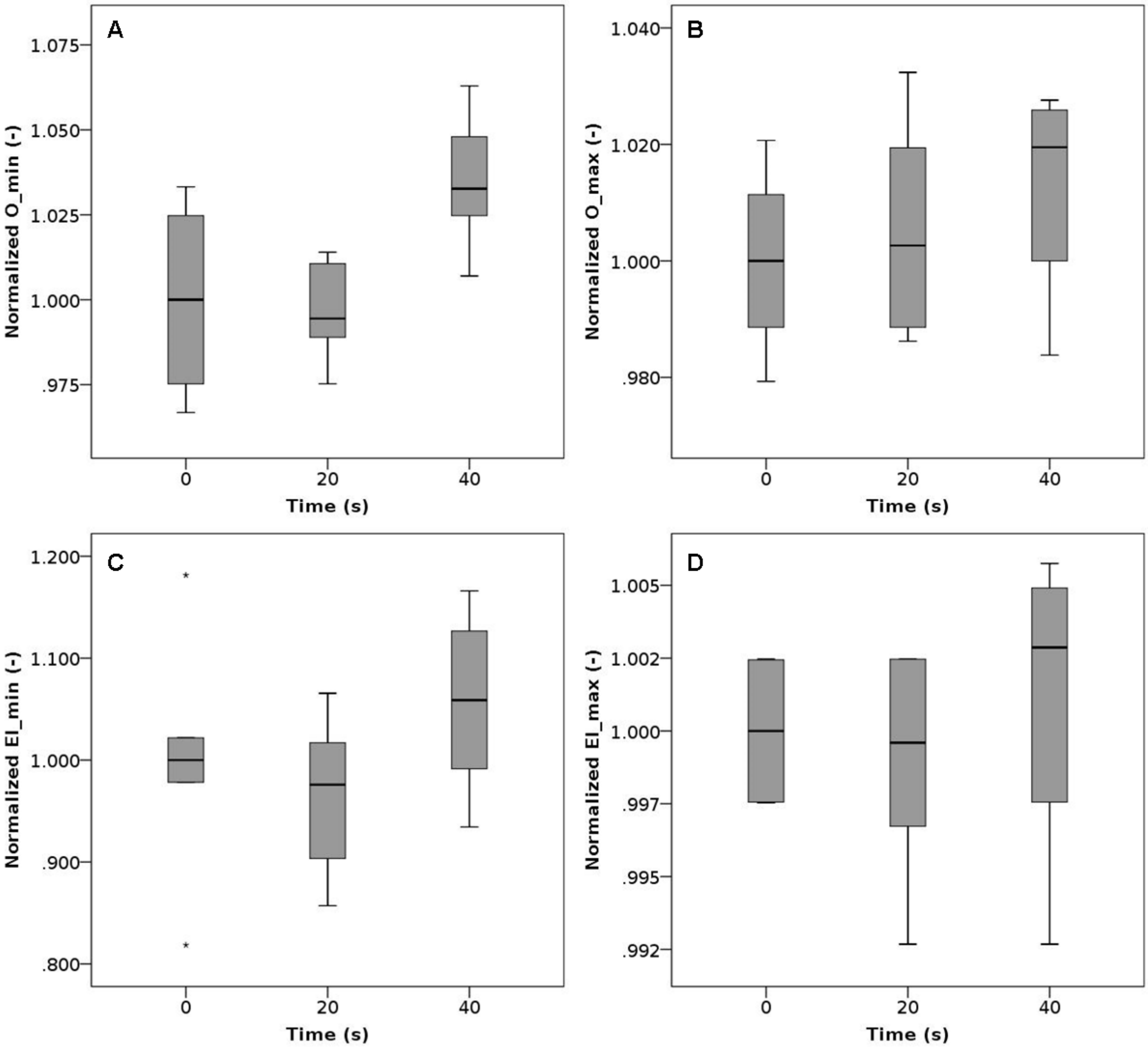

Supplementary Figure 6: Results of ektacytometry measurements after vortexing. (A): Normalized Omin as a function of the vortexing time. Omin is the osmolality at which the minimal elongation index EImin is measured. (B): Normalized Omax as a function of the vortexing time. Omax is the osmolality at which the maximal elongation index EImax is measured (C): Normalized minimal elongation index EImin as a function of the vortexing time. (D): Normalized maximal elongation index EImax as a function of the vortexing time. Reported values have been normalized by the mean of the corresponding control measurements. n = 5, 6, 6 for vortexing of 0s, 20s and 40s, respectively, for all graphs.

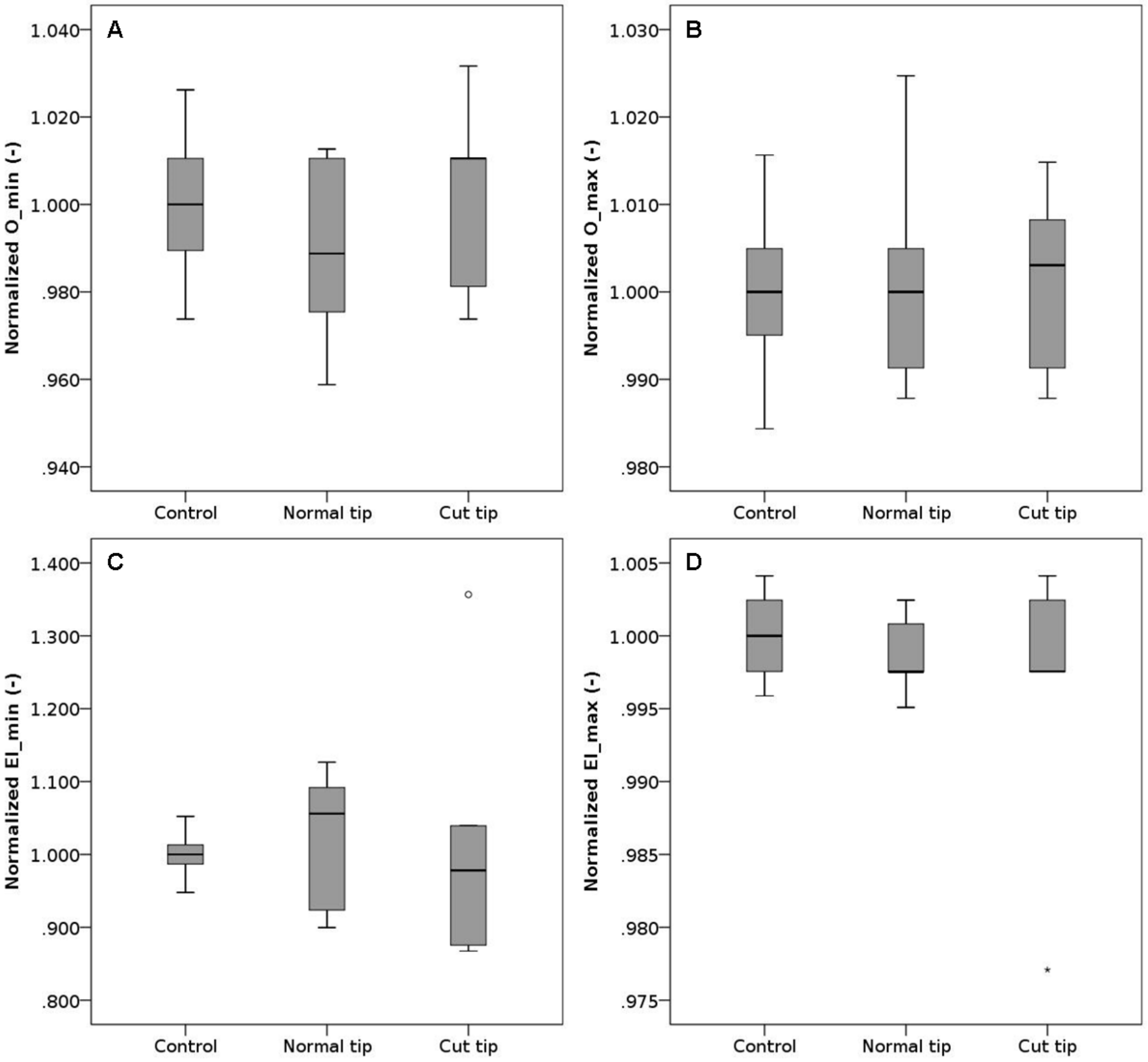

Supplementary Figure 7: Results of ektacytometry measurements after pipetting with normal versus cut tips. (A): Normalized Omin after pipetting with normal vs. cut tips. Omin is the osmolality at which the minimal elongation index EImin is measured. (B): Normalized Omax after pipetting with normal vs. cut tips. Omax is the osmolality at which the maximal elongation index EImax is measured. (C): Normalized minimal elongation index EImin after pipetting with normal vs. cut tips. (D): Normalized maximal elongation index EImax after pipetting with normal vs. cut tips. Reported values have been normalized by the mean of the corresponding control measurements. n per group = 5, for all graphs

2.7.3 Results of phosphatidylserine measurements

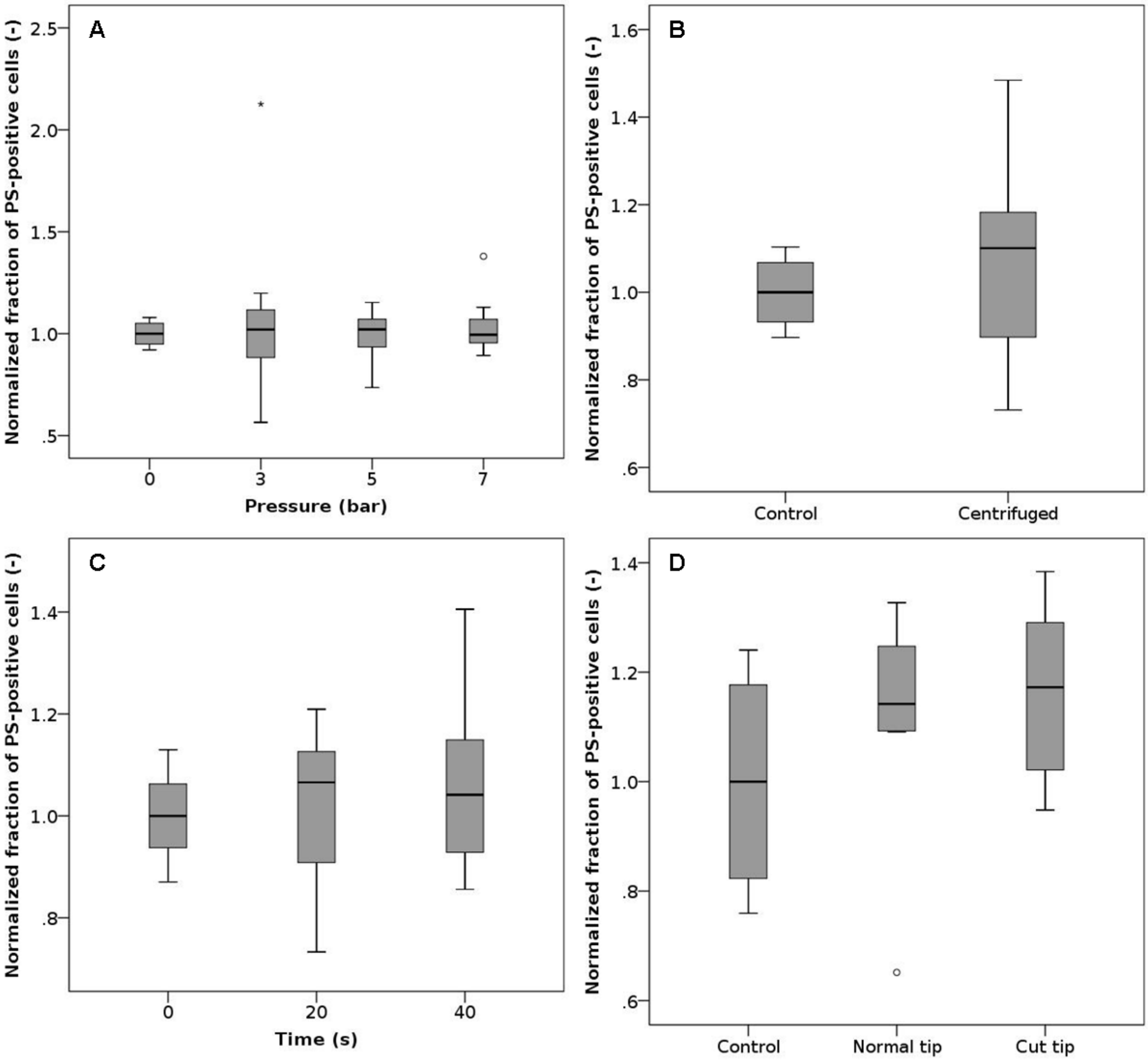

Supplementary Figure 8: Percentage of PS-positive red blood cells measured by flow cytometry. (A): Normalized fraction of Phosphatidylserine-positive red blood cells as a function of the applied pressure level (exposure time 1s, 10 consecutive times with 30s recovery). n per group = 8. (B): Normalized fraction of Phosphatidylserine-positive red blood cells after centrifugation at 900g for 5 minutes. n = 7, 8 for control and centrifuged samples, respectively. (C): Normalized fraction of Phosphatidylserine-positive red blood cells as a function of the vortexing time. n = 7, 8, 8 for vortexing during 0s, 20s and 40s, respectively. (D): Normalized fraction of Phosphatidylserine-positive red blood cells after pipetting with normal vs. cut tips. n per group = 8. Reported values have been normalized by the mean of the corresponding control measurements.

2.7.4 Results of multiple centrifugation and resuspension steps

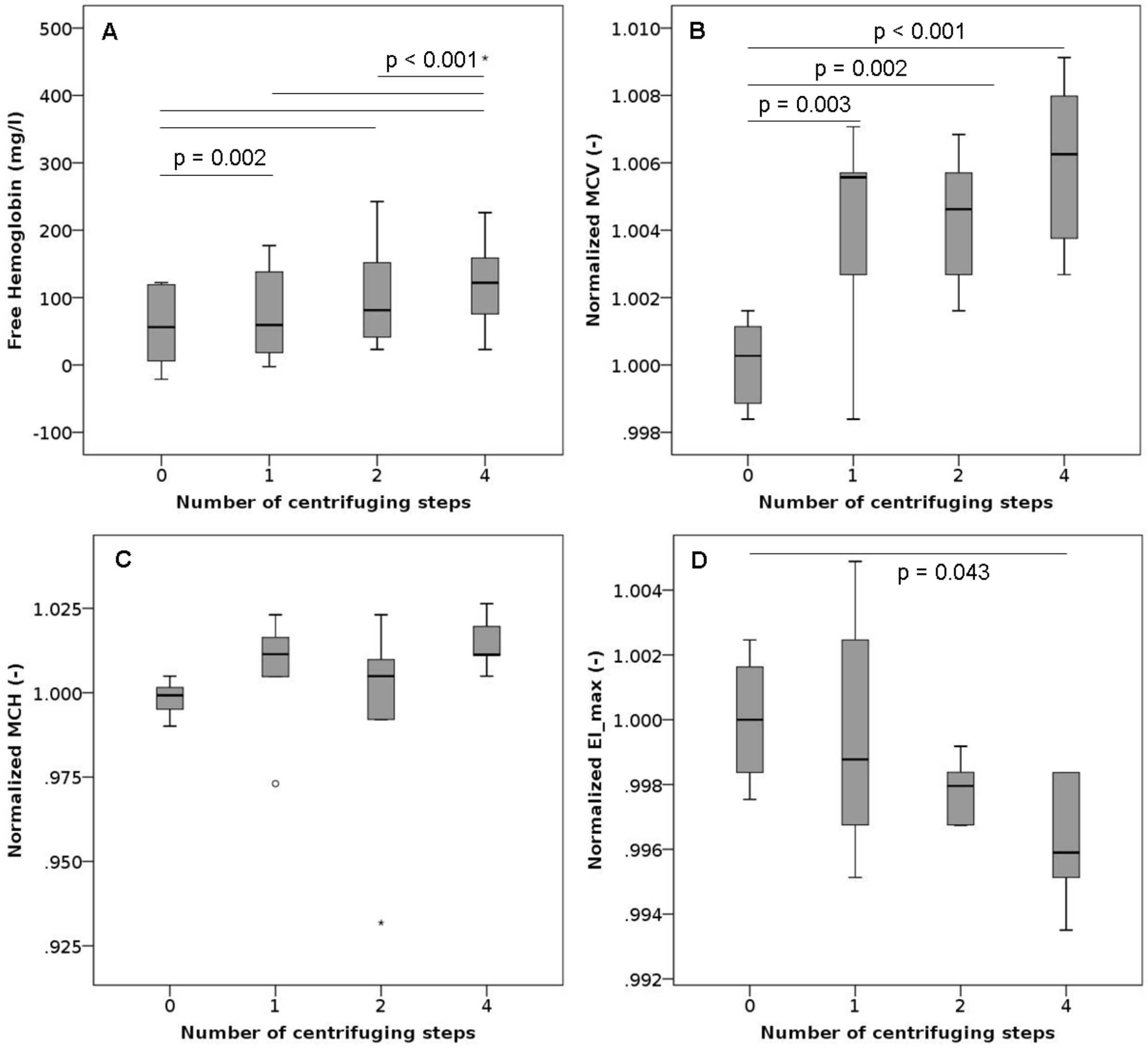

Supplementary Figure 9: Free hemoglobin, MCV, MCH and EImax after repeated centrifugation and resuspension. Samples were centrifuged at 900 g and vortexed for 2s between two consecutive centrifugation steps. (A): Free hemoglobin as a function of the number of centrifugation and resuspension steps. time per step = 5 or 10 min, n per group = 12. (B) Normalized mean cell volume as a function of the number of centrifugation and resuspension steps. Reported values have been normalized by the mean of the corresponding control measurements. time per step = 5 min. n per group = 6. (C) Normalized mean corpuscular hemoglobin as a function of the number of centrifugation and resuspension steps. Reported values have been normalized by the mean of the corresponding control measurements. time per step = 5 min, n per group = 6. (D): Normalized maximal elongation index EImax as a function of the number of centrifuging and resuspension steps. Reported values have been normalized by the mean of the corresponding control measurements. time per step = 5 min, n per group = 6.

3 Blood Pump Design Variations and their Influence on Hydraulic Performance and Indicators of Hemocompatibility

This chapter has been published as:

Wiegmann L, Boës S, de Zélicourt D, Thamsen B, Schmid Daners M, Meboldt M and Kurtcuoglu V, "Blood Pump Design Variations and Their Influence on Hydraulic Performance and Indicators of Hemocompatibility" *Ann. Biomed. Eng.*, vol 46, p. 417, 2018.

3.1 Abstract

Patients with ventricular assist devices still suffer from high rates of adverse events. Since many of these complications are linked to the flow field within the pump, optimization of the device geometry is essential. To investigate design aspects that influence the flow field, we developed a centrifugal blood pump using industrial guidelines. We then systematically varied selected design parameters and investigated their effects on hemodynamics and hydraulic performance using computational fluid dynamics. We analysed the flow fields based on Eulerian and Lagrangian features, shear stress histograms and six indicators of hemocompatibility. Within the investigated range of clearance gaps (50 µm to 500 µm), number of impeller blades (4 to 7), and semi-open versus closed shroud design, we found association of potentially damaging shear stress conditions with larger gap size and more blades. The extent of stagnation and recirculation zones was reduced with lower numbers of blades and a semi-open impeller, but it was increased with smaller clearance. The Lagrangian hemolysis index, a metric commonly applied to estimate blood damage, showed a negative correlation with hydraulic efficiency and no correlation with the Eulerian threshold-based metric.

Key Words: computational fluid dynamics, ventricular assist device, centrifugal blood pump, impeller design, blood damage, thrombosis, hemolysis

3.2 Introduction

Ventricular assist devices (VADs) are the main treatment option for patients with end-stage heart failure if heart transplantation is not possible. Even though VADs are increasingly implanted as destination therapy, patients still suffer from high rates of adverse events [183]. Many of these, such as bleeding, thrombosis and stroke, are thought to be closely related to the flow conditions within the VAD. These flow conditions are determined to a large extent by the pump design, which suggests that its optimization would translate to fewer adverse events and improve patients' quality of life.

Among the existing pump types, turbodynamic pumps are most widely used for VADs. Several experimental and numerical frameworks have been devised for their optimization. Studies such as those by Wu et al. [167], [169] and Arvand et al. [13] shed light on the impact of different impeller designs and clearance gap sizes, while others have focused on developing automated optimization frameworks [165], [166]. Yet, for designers, it is important to gain insight into the impact of single design parameters independently. Building on the vast collective know-how on generic turbodynamic pumps, Mozafari et al. systematically investigated the impact of variations in geometry [16], [17]. The latter study [17] focused on hydrodynamic performance, investigating the influence of geometry on a metric for hemolysis.

Computational VAD design studies reporting on hemocompatibility have typically focused on hemolysis [163], [164], [168], [211] represented by a hemolysis index (HI), which incorporates a weighted integration of shear stresses and exposure times. However, despite being widely used, HI performs poorly in predicting experimentally measured hemolysis values [126]. Its value derives from providing insight into the shear stress history as a general indicator of potential damage to blood cellular components, which may be of use for comparative studies. Thrombus formation as another major aspect of hemocompatibility is driven by multiple factors, including platelet activation and slow blood flow conditions. While an assessment of the latter is indeed feasible, direct computational prediction of platelet activation is currently not possible. Therefore, computationally determinable surrogates have been suggested to serve as alternatives [174], [212]. In general, views on the best surrogate metric of hemocompatibility diverge and validated models for predictions of measured values remain a challenge. This may be one reason why metrics applied for assessing blood damage differ between studies on VAD geometry.

In this study, we provide a comprehensive investigation of selected design parameters in view of their hydrodynamic performance and hemodynamic characteristics. Our geometry is based on an industrial pump design guideline [15], starting from which we investigate the effect of alterations in clearance gap, number of blades, and shroud design. We use computational fluid dynamics simulations that are validated experimentally regarding hydraulic performance to assess the flow fields within the pump, as well as Lagrangian particle tracks to characterize the stress exposure of blood cellular components flowing through the device. These analyses are further supplemented by the classical HI and other metrics proposed to correlate with platelet activation, thrombus formation, or acquired von Willebrand disease. Collectively, these results shed light on the impact of gap size, blade number and shroud design on shear stress exposure and flow stagnation, both of which were shown to have implications in terms of blood damage and thrombosis potential.

3.3 Material and Methods

3.3.1 Baseline Pump Design

The impeller and the housing were designed according to the industrial design guideline for centrifugal pumps by Gülich [15]. Starting with six input parameters that describe the desired operating conditions and impeller topology, the design process is broken down into 21 steps, involving 65 equations and look-up tables, which ultimately result in fully constrained geometries of the impeller and housing. Details on this process are given in Supplementary Material A.

The first three input parameters that describe the desired operating conditions were maintained constant for all designs performed in this study: Operating rotational speed and pressure head were set to 3000 rpm and 100 mmHg, respectively. The design flow rate as an input to the design guideline was iteratively increased until, for our baseline geometry, an effective flow rate of 4 to 5 L/min was achieved in the computational fluid dynamics (CFD) simulation. The chosen speed and pressure head correspond to that of HVAD (Medtronic/Heartware, Minneapolis, MN, USA), a clinically used VAD that produces a flow rate of 5 L/min against a pressure head of 106 mmHg at 3000 rpm[213]. The simulated effective flow rate in the retained baseline geometry was 4.4 L/min.

The remaining three input parameters for the impeller topology, namely clearance gap size (defined as the distance between the tip of the blades and the housing), number of blades and shroud design, were chosen based on the recommendations given in Gülich [15]. They are listed in Table 2 and Table 3 under “Baseline”. Figure 11 shows the CAD drawings of the resulting pump, featuring a priming volume of 11 mL and an impeller with 32 mm diameter. Since the character of this study is conceptual, the design process was free of any constraints imposed by bearing and actuation systems.

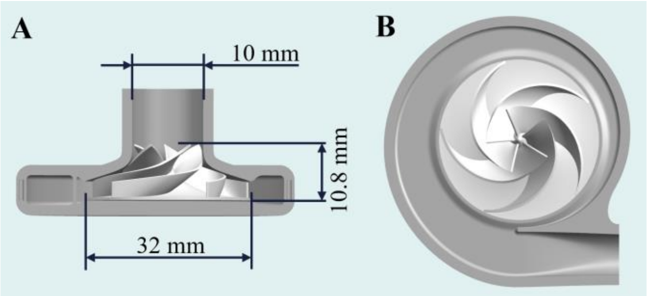

Figure 11: A: Side-view of the CAD model of cut-open housing and impeller design that served as baseline for the CFD simulation, B: Top-view of the CAD model of baseline impeller and cut-open housing.

3.3.2 Design variations

Starting with the baseline design as the initial configuration, clearance gap size, number of blades, and shroud type were varied independently (Table 2). These variations resulted in a total of eight simulated designs, including the baseline design. Table 3 shows the combination of parameters for each variant. Parameter ranges were chosen based on literature and existing technology. For the size of clearance gap, we selected a lower bound of 50 µm and an upper bound of 500 µm based on the dimension of the smallest gaps between impeller and housing of the HVAD [7] and the HM3 (HeartMate 3, Abbott/Thoratec, Abbott Park, IL, USA) [214], respectively. The number of blades was varied from four as seen in a number of clinically used VADs, including the HVAD and HM3, up to seven in order to investigate the suggested range of five to seven blades based on the specific speed of our pump design [15]. In the third variation, the influence of the presence or absence of a top shroud was examined. A semi-open design has a bottom shroud but no top shroud (like the HVAD), whereas a closed design has both bottom and top shrouds (like the HM3). In both designs, we kept the blade height constant. Therefore, the housing of the closed design was slightly larger to maintain the desired clearance gap, resulting in a 1.6% increase of the priming volume.

Parameter	**Value**
Clearance gap size	50, 150, **300**, 500 µm
Number of blades	4, **5**, 6, 7
Shroud design	**Semi-open**, closed

Table 2: Investigated geometry parameter values. The clearance gap size, number of blades and shroud design were investigated independently, varying one parameter at a time while the others were maintained at their baseline value (marked in bold).

Variant	Clearance gap				Number of blades				Shroud design	
	I	II	Baseline	III	IV	Baseline	V	VI	Baseline	VII
Clearance gap size (µm)	50	150	300	500	300	300	300	300	300	300
Number of blades	5	5	5	5	4	5	6	7	5	5
Shroud design	semi-open	semi-open	semi-open	semi-open	semi-open	semi-open	semi-open	semi-open	semi-open	closed

Table 3: Combinations of geometry parameters for each simulated design. Only one parameter was varied at a time for each of the three parameters: clearance gap, number of blades and shroud design. The baseline design is the same for each of the three variations. This resulted in a total of eight individual designs (including the baseline design) that were evaluated in CFD simulations.

3.3.3 Computational fluid dynamics simulations

Computational fluid dynamic simulations were carried out for the eight different designs to evaluate their hydrodynamic performance and associated hemodynamics. The geometries were imported into the commercial CFD package StarCCM+ (Siemens, Munich, Germany). Polyhedral grids were generated using the same settings for all configurations, including a 4-element boundary layer along the walls and a local mesh refinement in the clearance gap, ensuring that it contained a minimum of twelve cell layers. The resultant grid sizes ranged between 4.7 and 7.6 million cells.

The three-dimensional unsteady Reynolds-averaged Navier-Stokes equations were solved using the k-ω-SST turbulence model and implicit second order temporal discretization. Blood was modelled as a Newtonian fluid with a viscosity of 3.5 mPa s and a density of 1060 kg/m^3. This simplification was considered acceptable, as the non-Newtonian properties of blood, such as shear-thinning, become negligible at high shear rates (> 100 s^{-1}) [141] such as those typically found in VADs. The rotation of the impeller was implemented as a rigid body motion with a set speed of 3000 rpm. Pressure boundary conditions were set at the inlet and outlet with a user-defined function such that a constant static pressure head of 100 mmHg was kept between inlet and outlet of the pump.

The simulations were carried out with a convergence criterion of 10^{-4} for the residual errors and a time step of $5 \cdot 10^{-5}$ s, corresponding to less than 1° rotation per time step at 3000 rpm. The simulations were run for five rotations after the flow had stabilized, and only the fifth cycle was used for the analysis. Grid and time step independence were confirmed for pressure, velocity, and shear stresses as reported in Supplementary Material B.

To probe blood cell paths through the pump, we implemented a Lagrangian particle tracking with passive advection. The particles had a diameter of 5 µm and a density of 1125 kg/m^3, which are representative of the dimension and density of red blood cells. A total of 6332 particles were seeded 4 mm downstream of the inlet in a uniform spatial distribution during four consecutive time steps.

3.3.4 Validation

To validate the numerical simulations, the hydraulic performance of the baseline pump design was also assessed experimentally. The baseline design was complemented with features for motor shaft integration resulting in only slight geometric changes to the bottom of the housing below the impeller which was assumed to have no impact on the fluid dynamics. This design was then 3D-printed using photopolymeric resin (FullCure 720, Objet-Stratasys Inc., Eden Prairie, MN, USA) in a polyjet printer (Objet Eden 350 V, Objet-Stratasys Inc) with a layer thickness of 16 µm. We investigated the surfaces roughness of the printed material with a confocal laser microscope (VK-X260K, Keyence International, Mechelen, Belgium) for different inclinations relative to the printing axis, obtaining a mean Ra value of 5 µm. A brushless motor (EC-max 40, 120 W, Maxon Motor AG, Sachseln, Switzerland) was used for actuation. The impeller was mounted directly on the motor shaft through press fit. The 3D-printed pump was connected to the test bench[161] with two pressure-controlled fluid reservoirs, and the resulting flow rate was measured at the pump inlet as illustrated in Figure 2. The pressure head over the pump was measured with two in-line pressure sensors (TruWave, Edwards Lifesciences, Irvine, CA, USA) connected to the inlet and the outlet of the pump.

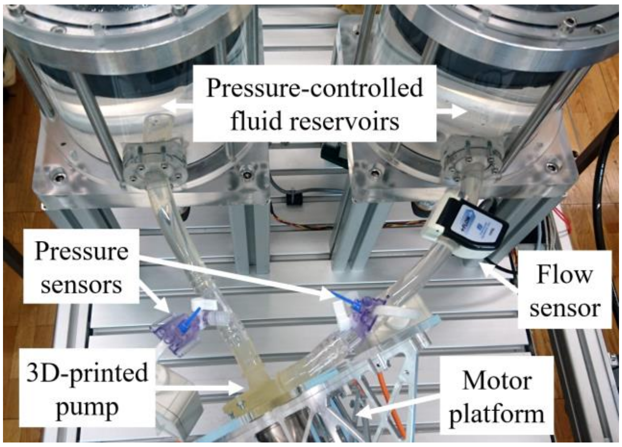

Figure 12: 3D-printed baseline pump design on the motor platform, connected to the test bench [161] for experimental validation

3.3.5 Analyses

Table 4 summarizes the metrics used to compare the various design options in terms of hydrodynamic performance and hemodynamic characteristics.

To gain better understanding of the relation between design features and potential blood damage, we investigated the flow fields qualitatively and quantitatively. To this end, we visualized the regions with low velocities, potentially prone for platelet aggregation and thrombus formation [215], considered disturbances of the flow field and investigated the location of zones with high shear stresses and compared histograms of medium and high shear stresses and exposure times along the Lagrangian particle tracks. We also analysed six metrics proposed in literature to assess blood damage potential that quantify Eulerian and Lagrangian characteristics of the simulated flow fields. Spanwise vorticity and hemolysis index (HI) were integrated over all particle tracks. All other metrics, Eulerian in nature, were computed at each time step and averaged over the last rotation.

Central to most blood damage models are the fluid shear stresses experienced by blood cells and plasma proteins as they flow through the device. The scalar shear stress, τ, was calculated from the viscous shear stress components, σ_{ij}, according to [216]:

$$\tau = \left[\frac{1}{6}\sum\left(\sigma_{ii} - \sigma_{jj}\right)^2 + \sum \sigma_{ij}^2\right]^{1/2} \tag{9}$$

Reynolds stresses were not included in the scalar shear stress since blood damage models available in literature are based on viscous stresses only [126].

HI was calculated as a power law of the scalar shear stresses and exposure time [115] (see corresponding equation in Table 5) using constants by Heuser and Opitz [217] as presented before [126]. Values of HI were integrated along each particle track based on the recorded shear stress histories, and were then averaged to derive the total HI for blood flowing through the VAD. Variation in the number of seeded particles above 6332 (tested range 156 to 9498) did not result in significant changes in the computed HI.

We further determined the overall volumes of fluid in which fluid shear stress is above the threshold suspected for von Willebrand factor (VWF) cleavage (τ>9Pa), platelet activation (τ>50Pa) and hemolysis (τ>150Pa) [174], respectively. Enhanced VWF cleavage and the successive loss of its high molecular weight multimers is believed to be one of the main causes for bleeding complications in VAD patients [60]. Areas of very low wall shear stress (WSS) on the rotor surface (WSS<1Pa) were derived to assess the potential risk of platelet deposition [218]. The Lagrangian spanwise vorticity index (SPWVI) was shown numerically to correlate well with the platelet activation status [212]. This correlation was originally reported for prosthetic heart valves, but since the principles behind shear stress-induced effects on blood components are comparable for blood pumps, an application in this field seems reasonable[99].

To test for association between blood damage indices suggested in literature, we calculated the nonparametric rank correlation coefficients (Spearman’s rho) using the IBM SPSS Statistics 23 software (IBM Corporation, Armonk, USA). P-values below 0.05 were considered indicative of statistical significance. We checked visually for the absence of non-monotonic relations.

Metric	**Implementation**	**Implication**	**Ref.**
Pump flow rate (Q_{pump}) [m^3/s]	$Q_{pump} = \frac{1}{T_{2\pi}} \int_0^{T_{2\pi}} Q(t) dt$	Suitability for full pump support of patient	
Leakage flow rate (Q_{leak}) [m^3/s]	$Q_{leak} = \int \bar{v} \cdot \bar{n} \, dA_{gap}$	Efficiency losses	[167]
Hydraulic efficiency (η) []	$\eta = \frac{P_{hydr}}{P_{mech}} = \frac{Q_{pump} \cdot H}{\Omega \cdot T}$	Hydraulic design	
Relative fluid volume with scalar shear stress above a threshold ($\mathbf{I}_{\tau > Thres}$) []	$\mathrm{I}_{\tau > Thres} = \frac{V_{\tau > Thres}}{V_{total}}$	Hemolysis (Thres = 150 Pa) Platelet activation (Thres = 50 Pa) VWF cleavage (Thres = 9Pa)	[174]
Relative area of low WSS on the impeller surface ($\mathbf{I}_{WSS<1Pa}$) []	$\mathrm{I}_{WSS<1Pa} = \frac{A_{WSS<1Pa}}{A_{total}}$	Thrombus formation	[218]
Spanwise vorticity index (SPWVI) [1/s]	$SPWVI = \frac{1}{N_p} \sum_{k=1}^{N_p} \frac{1}{N_k} \sum_{j=1}^{N_k} \lvert SPWV_{k,j} \rvert$ $SPWV(\bar{s}; t)$ $= \lvert \bar{\omega}(\bar{s}; t) \rvert \sin(\varphi(\bar{s}; t))$	Platelet activation status	[212]
Hemolysis Index (HI) []	$HI = \frac{1}{N_p} \sum_{k=1}^{N_p} C \left(\sum_{j=1}^{N_k} \Delta t_{k,j} \tau_{k,j}^{\beta/\alpha} \right)^{\alpha}$ $\alpha = 0.7650$ $\beta = 1.9919$ $C = 1.8 \cdot 10^{-6}$	Hemolysis	[115], [217]

Table 4: Summary of the analyzed hydrodynamic and hemocompatibility metrics, their implementation, and their suspected implication for blood pumps. Nomenclature: Q(t): volume flow rate [m^3/s], t: time [s], $T_{2\pi}$: time period for one rotation [s], $\bar{\mathbf{v}}$: fluid velocity vector [m/s], $\bar{\mathbf{n}}$: normal of Agap [], A_{gap}: surface of gap between impeller and housing [m^2], P_{mech}: mechanical power [W], Phydr: hydraulic power [W], Ω: angular speed [rad/s], T: torque on rotor [Nm], H: pressure head [Pa], τ: scalar shear stress obtained from Equation 1 [Pa], $V_{\tau>Thresh}$: fluid volume with scalar shear stresses above the prescribed threshold [mL], V_{total}: total volume of fluid in the pump [mL], VWF: von Willebrand factor, WSS: wall shear stress [Pa], A_{total}: total surface area of the impeller surface [m^2], $A_{WSS>1Pa}$: area of the impeller surfaces exposed to WSS above 1Pa [m^2], SPWV: local spanwise vorticity [1/s], $\bar{\boldsymbol{s}}$: position vector [m], $\bar{\boldsymbol{\omega}}(\bar{\mathbf{s}}; \mathbf{t})$: vorticity vector [1/s], $\boldsymbol{\varphi}(\bar{\mathbf{s}}; \mathbf{t})$: angle formed by velocity and vorticity vector [rad], N_k: number of points on the kth particle trajectory [], N_p: number of particle trajectories [], α,β,C: empirical constants [217].

3.4 Results

The influence of design parameter variation on pump flow rate and hydraulic efficiency is shown in Figure 13. The pump flow rate ranged between 3.2 and 5.7 L/min, and the hydraulic efficiency between 38 and 53%. With 4.4 L/min of flow at 100 mmHg, the baseline geometry achieved an efficiency of 47%. The variation of the clearance gap led to the most substantial effects, followed by the change in shroud design.

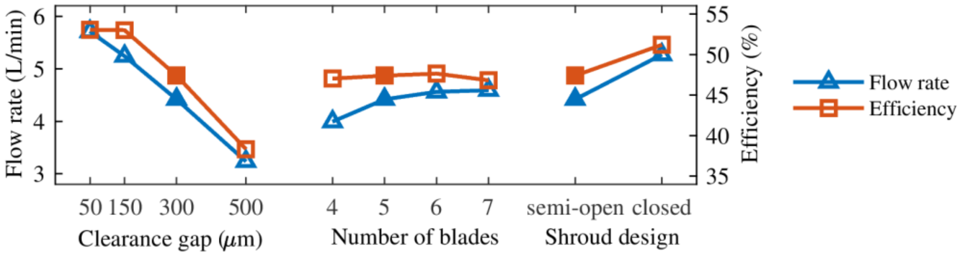

Figure 13: Computed flow rate and hydraulic efficiency plotted for variations of clearance gap size, number of blades and shroud design. The baseline configuration is marked by filled symbols. When one parameter was varied, the remaining two parameters were kept at baseline value. Note that the vertical axes depicting flow rate and efficiency have ranges of 3-6 L/min and 35%-55%, respectively.

Relative changes in hemocompatibility indicators are shown in Figure 14. In this figure, all indices are normalized by their respective value in the baseline geometry to allow for a direct comparison of the relative impact of the various design variations. The numerical data, without normalization to the baseline geometry, is listed in Supplementary Material C. Fractions of fluid volume with shear stress values above a threshold, $I_{\tau>150\mathrm{Pa}}$, $I_{\tau>50\mathrm{Pa}}$ and $I_{\tau>9\mathrm{Pa}}$, were in the range of 0.002% - 0.049%, 1.1% - 2.2%, and 14.4% - 16.9% of the total fluid volume, respectively.

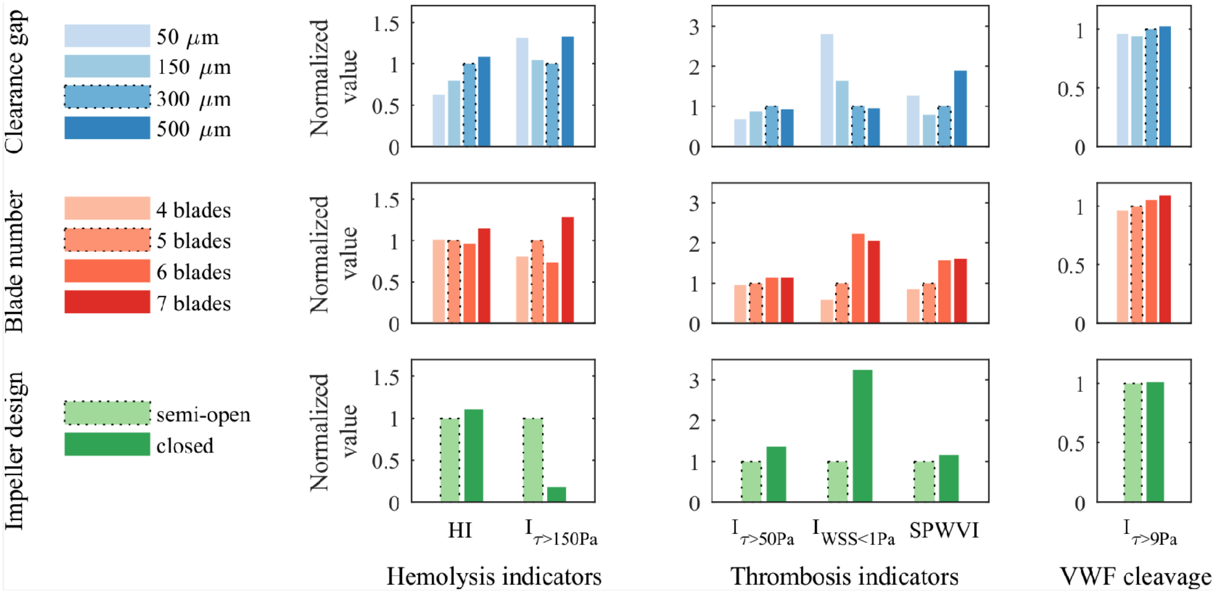

Figure 14: Effect of change in clearance gap size (50 µm to 500 µm), number of blades (4 to 7), and shroud design (semi-open or closed) on hemocompatibility indicators. Hemocompatibility indicators are grouped into three categories according to their suspected implications: (1) Hemolysis indicators are HI and $I_{\tau>150Pa}$. (2) Thrombosis potential is indicated by $I_{\tau>50Pa}$, rotor surface with $I_{WSS<1Pa}$ and SPWVI. (3) Bleeding potential due to VWF cleavage is assessed with $I_{\tau>9Pa}$. All indices are normalized by their respective values in the baseline configuration. Numerical values are listed in Supplementary Material C. Dashed frames indicate baseline configuration.

Table 5 shows Spearman's rank correlation coefficients (r) between all derived metrics of pump performance and hemocompatibility. Strong positive correlations were found between HI and $I_{\tau>50Pa}$ ($r = 0.74$, $p = 0.037$), and between SPWVI and $I_{\tau>9Pa}$ ($r = 0.86$, $p = 0.007$). A strong negative relation was observed between HI and efficiency ($r = -0.71$, $p = 0.047$). None of the other correlations were found to be significant.

		η	**Q_{leak}**	**$I_{\tau>150Pa}$**	**$I_{\tau>50Pa}$**	**$I_{\tau>9Pa}$**	**$I_{WSS<1Pa}$**	**HI**	**SPWVI**
η	r	1							
	p-value	.							
Q_{leak}	r	-.48	1						
	p-value	*.233*	.						
$I_{\tau>150Pa}$	r	-.24	-.36	1					
	p-value	*.570*	*.385*	.					
$I_{\tau>50Pa}$	r	-.31	.50	-.64	1				
	p-value	*.456*	*.207*	*.086*	.				
$I_{\tau>9Pa}$	r	-.52	.26	.02	.64	1			
	p-value	*.183*	*.531*	*.955*	*.086*	.			
$I_{WSS<1Pa}$	r	.69	-.29	-.14	.14	.21	1		
	p-value	*.058*	*.493*	*.736*	*.736*	*.610*	.		
HI	r	**-.71***	.62	-.12	**.74***	.60	-.24	1	
	p-value	*.047*	*.102*	*.779*	*.037*	*.120*	*.570*	.	
SPWVI	r	-.50	.21	.43	.21	**.86****	.19	.41	1
	p-value	*.207*	*.610*	*.289*	*.610*	*.007*	*.651*	*.320*	.

Table 5: Spearman's rank correlation coefficients for the hydrodynamic and hemocompatibility metrics obtained by CFD simulations. Nomenclature: r: rank correlation coefficient, η: hydraulic efficiency, Q_{leak}: leakage flow rate, τ: scalar shear stress, $I_{\tau>150Pa}$, $I_{\tau>50Pa}$ and $I_{\tau>9Pa}$: fraction of fluid volume with scalar shear stresses above 150 Pa, 50 Pa and 9 Pa, respectively, WSS: wall shear stress, $I_{WSS>1Pa}$: relative area of the impeller surface exposed to WSS above 1 Pa, HI: hemolysis index, SPWVI: spanwise vorticity index, *: $p < 0.05$, **: $p < 0.01$. Statistically significant correlations are highlighted with bold case.

3.4.1 Clearance gap size

From the smallest clearance gap of 50 µm to the largest one of 500 µm, the flow rate decreased by 43% and the efficiency decreased by 28% (Figure 13). Although the flow rate steadily declined from 5.7 L/min to 3.2 L/min, the efficiency remained constant at 53% for the two smaller gaps (50 and 150 µm), and only declined for larger ones, reducing to 38% for a gap of 500 µm.

Figure 15 depicts the fluid volume exposed to high shear stresses (SS), which in Figure 4 were shown to be minimal for medium gap sizes (150, 300 µm). Yet, HI steadily increased with increasing gap size. In contrast, smaller gaps led to larger regions of low speeds (< 0.5 m/s, Figure 15). SPWVI was lowest for medium-sized gaps (Figure 14). Larger clearance gaps induced significant flow disturbances on the suction side of the blade as shown by streamlines seeded just above a blade, whereas for the small clearance gap (50 µm) streamlines seeded at the same position were almost undisturbed (Figure 15). The number of particles exposed to medium (>50 Pa) and high (>150 Pa) SS increased substantially for the large gap (Figure 15D). In contrast, large gaps reduced the maximum SS that particles were exposed to (Supplementary Material D).

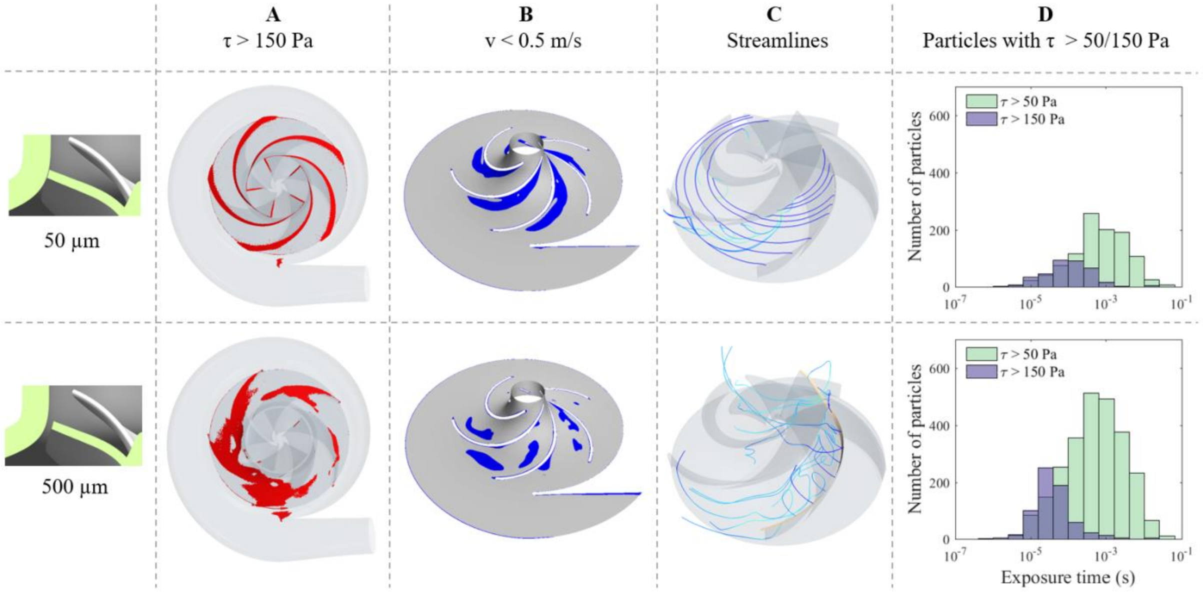

Figure 15: Visualization of the effects of change in clearance gap size from 50 µm to 500 µm. A: Localization and extent of areas of high shear stress (τ>150Pa). B: Regions with low velocities (v<0.5 m/s) along the meridional section of the flow channels inside the pump. The velocity threshold of 0.5 m/s was chosen for best visual representation of possible stagnation zones. C: Flow structures represented by streamlines seeded with a randomized distribution in the clearance gap above one of the blades. D: Histograms of the exposure times to shear stresses above 50 Pa and 150 Pa. With the 50 µm clearance gap, 1049 (16.8%) and 364 (5.8%) of the seeded particles experienced SS above 50 and 150 Pa, respectively, compared to 2560 (40.2%) and 669 (10.5%) with the 500 µm gap.

3.4.2 Number of blades

Increasing the blade number from four to seven increased the pump flow rate from 4.0 to 4.6 L/min (+15%), but did not affect efficiency (variation within ±1%, Figure 13). The values of

$I_{\tau>50Pa}$ and $I_{\tau>9Pa}$ increased marginally with an increasing number of blades (Figure 14). In contrast to $I_{\tau>50Pa}$, the thrombosis indicators $I_{WSS<1Pa}$ and SPWVI increased to 3.5-fold and 1.9-fold when the blade count was increased from 4 to 7. Stagnation zones with low velocity (Figure 16) increased with the number of blades and aggregated for higher blade numbers at the suction side of the blades. Exposure times to medium and high SS were almost unaffected, with a slight shift towards longer exposure to medium stresses for seven blades (Figure 16C).

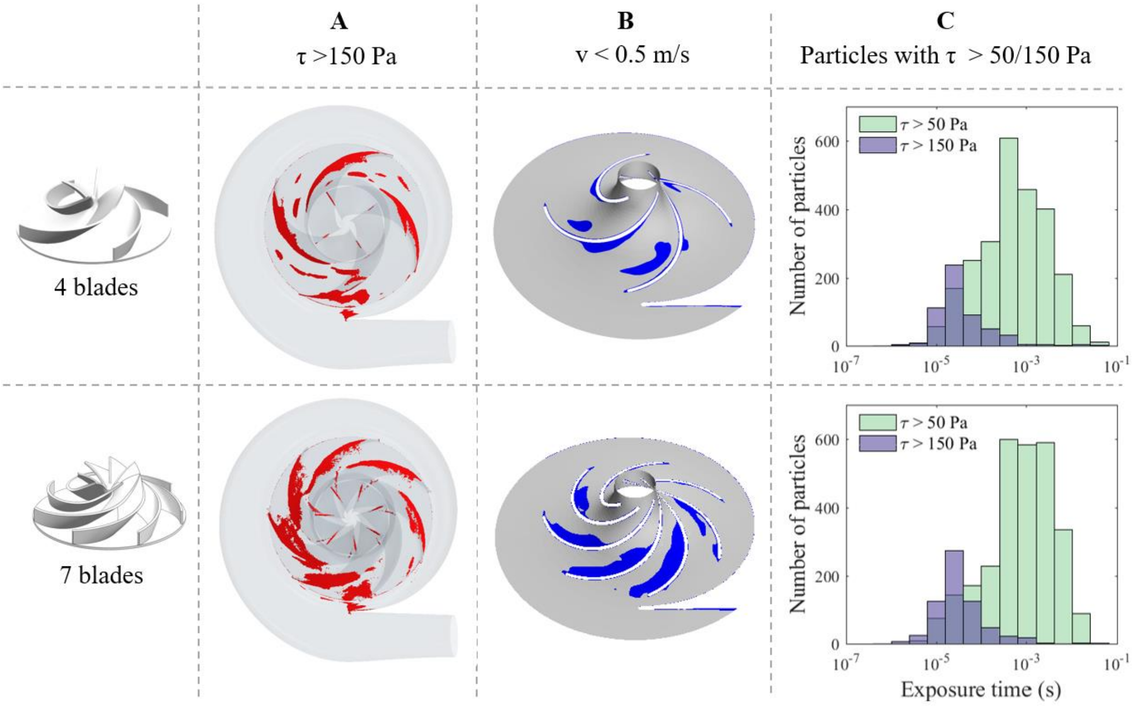

Figure 16: Visualization of the effects of change in the number of blades from 4 to 7. A: Areas of high shear stress (τ>150Pa). B: Regions with low velocities (<0.5 m/s) along the meridional section of the flow channels inside the pump. The velocity threshold of 0.5 m/s was chosen for best visual representation of possible stagnation zones. C: Histograms of the exposure times to shear stresses above 50 Pa and 150 Pa. With 4 blades, 2552 (40.3%) and 557 (8.8%) of the seeded particles experienced SS above 50 and 150 Pa, respectively, compared to 2835 (44.8%) and 651 (10.3%) with 7 blades.

3.4.3 Shroud design

Compared to the semi-open impeller, the closed impeller yielded higher hydraulic efficiency and flow rate (Figure 13). In the semi-open design, high SS occurred in the clearance gap, a behavior that was effectively suppressed by the closed design (Figure 17A). The closed design also reduced the size of the low-velocity zones near the blades (Figure 17B), but gave rise to stagnation zones at the corner edges where blades and shroud meet. The closed impeller radically reduced the amount of fluid exposed to SS above 150 Pa, but moderately increased the amount of fluid exposed to mid-range SS above 50 Pa, and more than tripled the value of low WSS $I_{WSS<1}$ (Figure 14). Similarly, substantially fewer particles were exposed to high SS for the closed design, while simultaneously, exposure time to medium SS increased (Figure 17C).

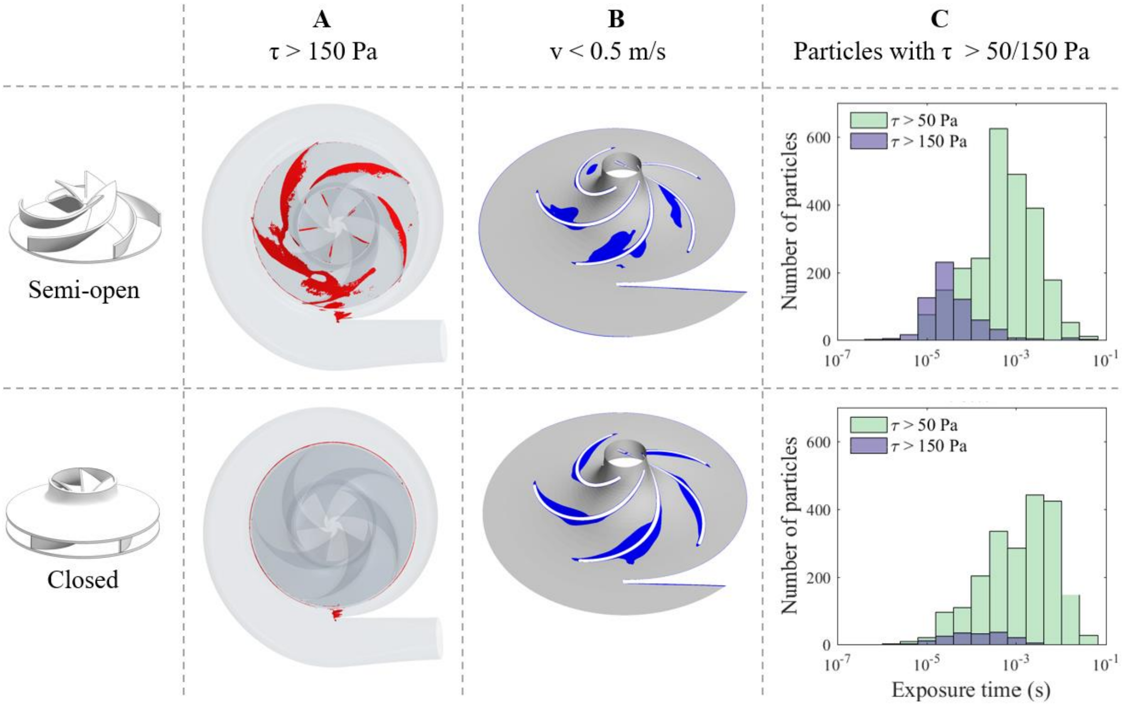

Figure 17: Visualization of the differences in shear stress and flow speed in a semi-open and a closed shroud design. A: Areas of high shear stress (τ>150 Pa). B: Regions with low velocities (v<0.5 m/s) along the meridional section of the flow channels inside the pump. The speed threshold of 0.5 m/s was chosen for best visual representation of possible stagnation zones. C: Histograms of the exposure times to shear stresses above 50 Pa and 150 Pa. With the semi-open design, 2435 (38.5%) and 611 (9.7%) of the seeded particles experienced SS above 50 and 150 Pa, respectively, compared to 2111 (33.0%) and 171 (2.7%) with the closed design.

3.4.4 Validation

We compared simulated and measured pump performance with the baseline geometry, finding good agreement between the two modalities. For a speed of 3000 rpm and a pressure head of 100 mmHg, the simulated flow rate was 4.4 L/min versus 4.9L/min in the experiments, which corresponds to a difference of 10.3%. Figure 18 shows the experimental measurements of the relation between pressure head and flow rate at a rotational speed of 3000 rpm. A curve shape that is typical for radial pumps can be observed, flatter at low and steeper at high flow rates. The difference between experimentally measured and simulated flow rates is high in the low flow region (< 5 L/min) with 19.7% root mean square error compared to only 2.4% in the high flow region (> 5 L/min).

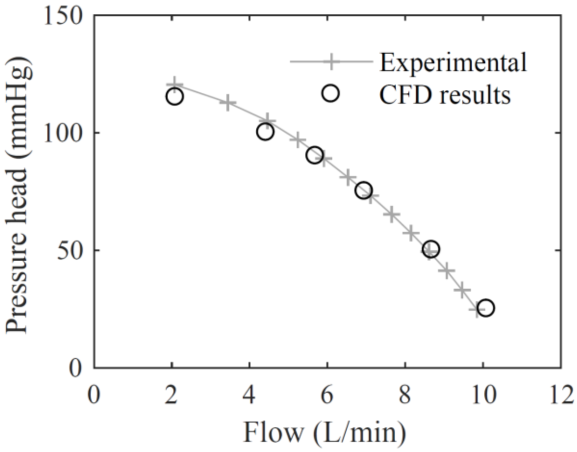

Figure 18: Experimental measurements and simulation results of the hydraulic performance of the baseline design at a rotational speed of 3000 rpm

3.5 Discussion

In this study, we performed systematic variations of design parameters in a centrifugal blood pump. Using CFD, we analysed their effects on the flow field and multiple metrics of hydraulic performance. Exposure to elevated shear stress and exposure duration have been shown to damage and/ or activate the cellular components of blood including erythrocytes, thrombocytes [174] and leukocytes [219]. According to Virchow's triad of thrombus formation, zones of low flow require attention. Despite the evidence for flow induced blood damage, validated models for predictions of measured values of damage remain a challenge. While indices such as the numerically derived hemolysis index often provide an integrated view on specific flow features, they should not be interpreted as predictors of measured blood damage. We, therefore, use them here in combination with detailed analysis of the flow fields and particle tracks to shed light on the influence of each independent design variation on the extent of cell exposure to potentially damaging or activating hemodynamic environments.

In the choice of clearance gap size, designers face conflicting requirements: Aiming for high hydraulic efficiency calls for small gaps, whereas minimization of maximum SS and suspected washout performance would suggest larger gaps. In our geometries, smaller gap sizes indeed increased the maximum SS (Supplementary material D). However, firstly, the total fluid volumes exposed to high SS ($I_{\tau>150Pa}$) were comparable for 50 and 500 µm gaps (Figure 14) and, secondly, smaller gaps induced cell screening, an effect also observed experimentally by Antaki et al. [220], such that only half as many particles effectively experienced these high SS in the 50 µm gap compared to the 500 µm gap (5.8% vs. 10.5% of the tracks, Figure 15D). Larger gaps on the other hand gave rise to substantial flow disturbances in the fluid path (Figure 15C), increasing SS and vorticity. As a result, volumes exposed to medium SS ($I_{\tau>50Pa}$) generally increased with gap size. These medium SS volumes, with sizes two to three orders of magnitude larger than those with SS above 150Pa, affected about 40% of the particles in the 500 µm gap setup vs. only 17% in the 50 µm gap configuration (Figure 15D). Increased vorticity content in the main particle paths is reflected by the increase in SPWVI with the largest gap size. Combined, the noted changes in SS histories led to lower HI in smaller gaps, which is consistent with previous results [163]. In contrast, Wu et al. [168] reported minimal HI at 100 µm compared to clearance gaps of 50 µm and 200 µm. Different to our study, they studied the effect of gap size prescribing a constant flow rate. While a well validated metric of hemolysis remains to be established, all qualitative and quantitative indicators investigated here suggest that by minimizing the number of cells exposed to high and medium stresses, smaller gaps may be expected to yield lower hemolysis than larger ones. This is also consistent with experimental observations [211]. SS>50 Pa and higher SPWVI have been proposed as indicators of platelet activation. However, whether the noted reduction in $I_{\tau>50Pa}$ and SPWVI (Figure 14) in the 50 µm gap compared to the 500 µm gap geometry do translate into reduced activation remains to be demonstrated. One major drawback of the smaller gaps is certainly the close to three-fold increase in regions of low WSS and flow separation with low velocities on the pressure side of the blades. Strategies to avoid stagnation regions should thus be devised in accordance to the retained gap size. The gap size also affected the location of potential flow stagnation regions, shifting from the pressure side in the 50 µm to centrally in the vanes in the 500 µm gap (Figure 15B).

Compared to gap size variations, varying the number of blades had more blunted effects. While there was a clear increase in volumes exposed to high SS with 7 blades compared to 4, SS histograms were almost unaffected, showing for 7 blades only a slight shift towards longer exposure times to medium stresses (Figure 16C). Consistent with these marginal changes in SS exposures, HI was also marginally affected. The SPWVI increased with the number of blades, as did the regions of potential flow stagnations ($I_{WSS<1Pa}$, Figure 14) due to flow separation at each blade (Figure 16B). Collectively, the decreased SS, vorticity indices and extent of potential stagnation zones point to fewer blades as being advantageous in terms of potential hemocompatibility. However, it should be noted that for fewer than 5 blades this comes at the cost of a decrease in pump flow rate.

In contrast to the above, shroud design variations yielded conflicting observations. Compared to the semi-open design, a closed shroud drastically reduced exposure to high SS but increased exposure time to medium SS (Figure 17C). The number of particles affected by medium SS was one order of magnitude larger than to the peak SS. HI was slightly lower for the semi-open configuration reflecting the opposite evolution of exposures to high and medium SS. However, without further data, no conclusion can be drawn on the integrated effect of these two changes on net hemolysis. Both platelet activation indicators suggested slightly preferable behaviour for the semi-open shroud. The semi-open compared to the closed design resulted in a smaller overall area of low WSS.

Overall, statistical analysis revealed that high efficiency correlates with low HI ($r = -0.71$, $p = 0.047$). Indeed, more efficient pumps have fewer recirculation zones, flow disturbances and lower leakage flow, all of which contribute to higher shear stresses or longer exposure times and thereby higher HI. This finding is consistent with the experimental data of Mozafari et al. [17]. Lack of correlation between HI and $I_{\tau>150Pa}$ ($r = -0.12$, $p = 0.78$) highlights that in the considered geometries, peak SS only reflects a small part of particles' SS histories, which are dominated by medium stresses as indicated by the correlation of HI and $I_{\tau>50Pa}$ ($r = 0.74$, $p = 0.037$) and the areas under the histograms in Figure 15D. The two metrics that have been suggested to indicate platelet activation, $I_{\tau>50Pa}$ and SPWVI, did not correlate ($r = 0.21$, $p = 0.61$) in our study.

The computational approach employed in this study has limitations. First and foremost, all design variations were tested against a constant pressure head. The consideration of pulsatile conditions would be an important next step, acknowledging not only the physiological pulsations in the cardiovascular system, but also VAD-inherent features such as washout algorithms as in the HM3 [221]. Secondly, while the blood damage indicators used in this study are widely employed in cardiovascular modelling, they remain explorative. They substantially simplify complex biological mechanisms [126], [130] and often perform poorly when evaluated against experimental data [126]. We, therefore, used them here to probe integrated flow characteristics rather then as predictors of measured blood damage. Quantification of true hemolysis or platelet activation potentials requires further investigation. Further effects, such as the interaction between blood and the pump material are also critical for thrombogenesis [96] and hemocompatibility. Biological advances in its understanding and modelling could significantly enhance the predictive power of CFD models. Finally, we investigated an approach presented recently, which links SPWVI to platelet activation [212]. We applied this metric to Lagrangian tracks of particles with properties similar to erythrocytes (diameter 5 µm, density 1125 kg/m^3) rather than platelets (1 µm, simulated as massless) as used in the original work. Even though this might slightly alter the flow paths, the major characteristics of the tracks are expected to remain unaffected. However, the SPWVI lacks a thorough experimental validation. Thus, the prediction of platelet activation remains challenging and requires further investigation.

3.6 Supplementary Material

3.6.1 Resulting geometric design parameters

Industrial pumps differ from blood pumps in terms of size, flow rate, pressure head, efficiency, and Reynolds number [16] to where the application of industrial pump guidelines to VADs constitutes an extension of their intended use. In our study, these differences caused discrepancies between the set design criteria and the actual operating points obtained in the computational fluid dynamic simulations (CFD): To achieve the desired pump flow rate of 4 to 5L/min in CFD, we increased the targeted flow given as a design input up to 10 L/min. Similarly, the targeted hydraulic efficiency was set to 80%, which is close to the maximum for centrifugal pumps, but the values achieved only ranged between 38% and 53%, depending on the clearance gap and shroud design chosen.

Possible reasons for the discrepancies observed between design criteria and observed operating points are:

- **Clearance gap to impeller diameter ratio**
  The ratio of the clearance gap to the diameter of the impeller is substantially larger for a blood pump than for an industrial pump. Therefore, any losses due to the clearance gap are more relevant, which may be underestimated in guidelines derived based on larger pumps.
- **Sub-optimal constraints**
  If there is no danger of clogging the pump and if the fluid medium allows it, a closed shroud design is preferable over a semi-open design for efficiency reasons. In our study, we simulated a closed design with the relatively high clearance gap of 300 µm. In combination with smaller clearance gaps, a higher efficiency is expected to be achieved.
- **Discarded leakage flow**
  The expected leakage flow rate as an input in the design process was set to zero. In an iterative design process, first CFD results of an actual leakage flow rate would be fed back into the calculation and would iteratively lead to more accurate results.
- **Absent downstream optimization**
  Designs based on the guideline are further optimized iteratively using CFD [15] and might achieve targeted efficiency values only after the optimization process.

Nonetheless, the resulting design in this study is comparable to clinical blood pumps with regard to impeller dimension, housing size, and hydraulic performance. The geometric output parameters based on the guideline are illustrated in Supplementary Figure 10, and the calculated values for the baseline design are listed in Supplementary Table 1.

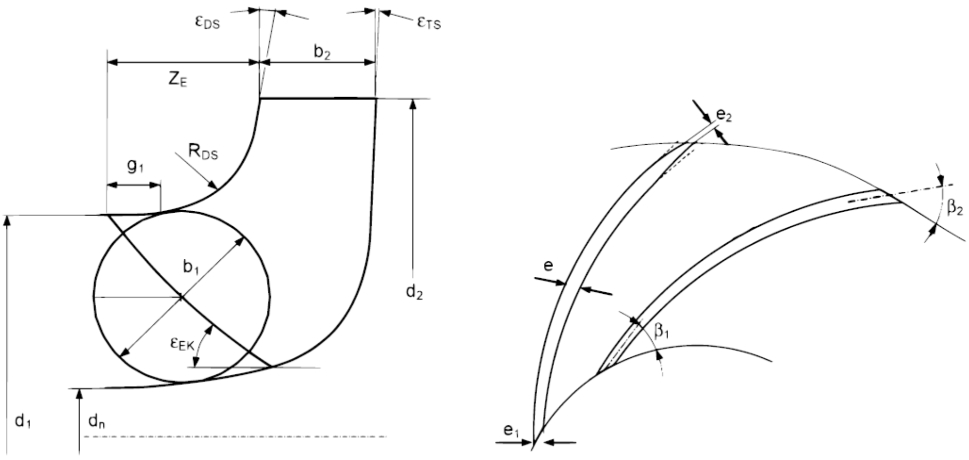

Meridional section of impeller

Plan view of two adjacent blades

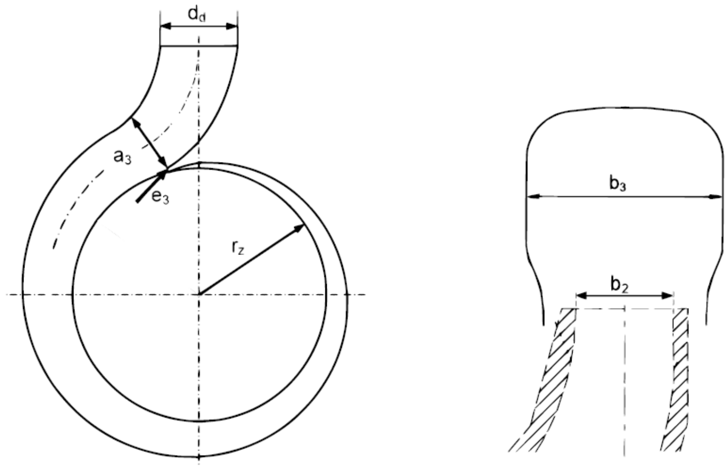

Plan view of volute casing

Meridional section of volute

Supplementary Figure 10: Design parameters for the meridional section and plan view of both impeller and volute casing according to the design guideline. Sketches adapted from Gülich[15], used with permission of Springer Nature.

	Symbol	Parameter	Value	Unit
Impeller	d_1	Diameter of impeller inlet	13.21	mm
	d_2	Outer diameter of impeller	32.08	mm
	d_n	Hub diameter	0.80	mm
	b_1	Width of the impeller inlet	6.21	mm
	b_2	Width of the impeller outlet	2.90	mm
	z_{La}	Number of impeller blades	5	[-]
	R_{Ds}	Radius of curvature	4.34	mm
	z_E	Axial extension	7.38	mm
	g_1	Short section to achieve flat pressure distribution	1.55	mm
	ε_{Ds}	Angle of the free blade at the trailing edge	18.00	°
	ε_{Ts}	Angle of the bottom shroud at the trailing edge	0.00	°
	ε_{EK}	Angle of the leading edge	35.00	°
	β_1	Inlet angle of impeller blade	84.44	°
	β_2	Outlet angle of impeller blade	19.21	°
	e, e_1, e_2	Blade thickness ($e = e_1 = e_2$)	0.51	mm
	ε_{sch}	Wrap angle	160.00	°
Volute casing	a_3	Width of the throat area	9.15	mm
	d_d	Inner diameter of the discharge nozzle	8.17	mm
	r_z	Cutwater radius	17.76	mm
	b_3	Height of the casing at the impeller outlet	5.79	mm
	e_3	Diameter of the cutwater tip	0.64	mm

Supplementary Table 1: Geometric parameters of the baseline design as obtained from the guidelines for dimensioning the impeller and the volute casing

3.6.2 Grid and time step independence studies

We conducted grid and time step independence studies on three line-probes located in crucial parts of our geometry: the first one spanned across the part of the pump directed towards the outlet, the second one followed a representative streamline within the vanes and the third one ran across the bottom gap between impeller and housing. The three locations are illustrated in Supplementary Figure 11. We investigated velocity (Supplementary Figure 12 and Supplementary Figure 13), pressure (Supplementary Figure 14 and Supplementary Figure 15) and shear stress (Supplementary Figure 16 and Supplementary Figure 17) depending on different mesh sizes and time steps. For the grid independence study, a time step of $\Delta t = 5 \cdot 10^{-5}$ s was used. For the time step independence study, a mesh with 6.3 million cells was used. All simulations were performed on our baseline geometry with 4 blades, a semi-open impeller and 300 µm clearance gap. All other settings of the CFD simulation are described in the Methods section of the main manuscript.

Since the evaluation of shear stress along the streamline line-probe revealed some differences depending on the grid size, we additionally checked for independence of the resulting hemolysis index HI. HI was $5.00 \cdot 10^{-5}$ for a mesh with 11.1 million cells compared to $5.07 \cdot 10^{-5}$ for a mesh with 6.3 million cells.

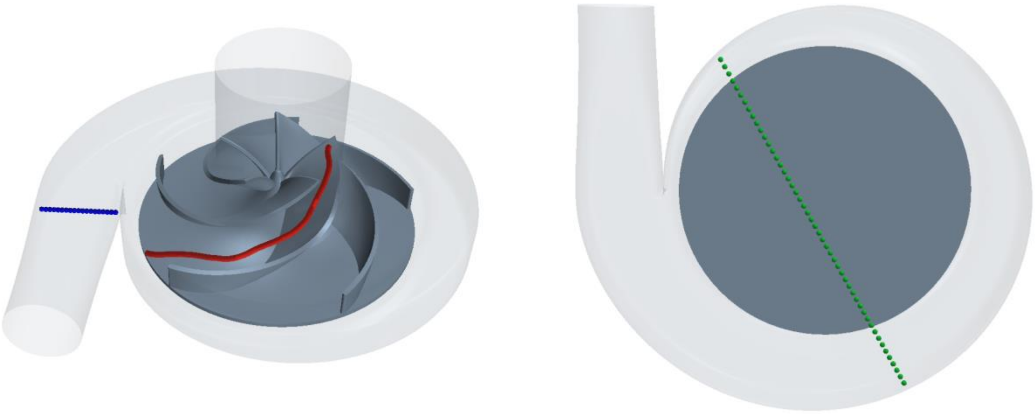

Supplementary Figure 11: Location of the three line-probes used for testing grid and time step independence: “Cross Outlet” (blue) runs across the part of the pump directed towards its outlet at half height of the channel. “Streamline” (red) runs along a streamline through the vane. “Bottom Gap” (green) runs across the gap below the impeller at half height of the total gap.

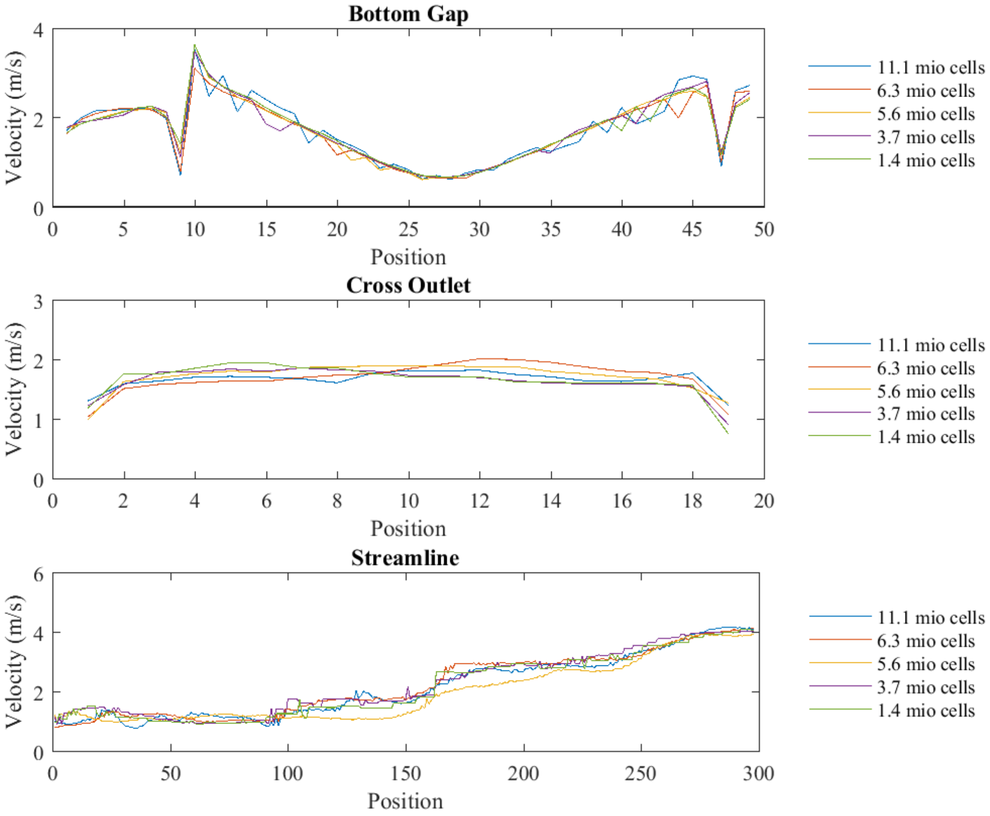

Supplementary Figure 12: Results of the grid independence study with respect to velocity. The three graphs represent the three geometric locations tested. The time step in these simulations was $\Delta t = 5 \cdot 10^{-5}$ s. The mesh with 6.3 million cells was chosen for the study. Position refers to the geometrical position on the line probe.

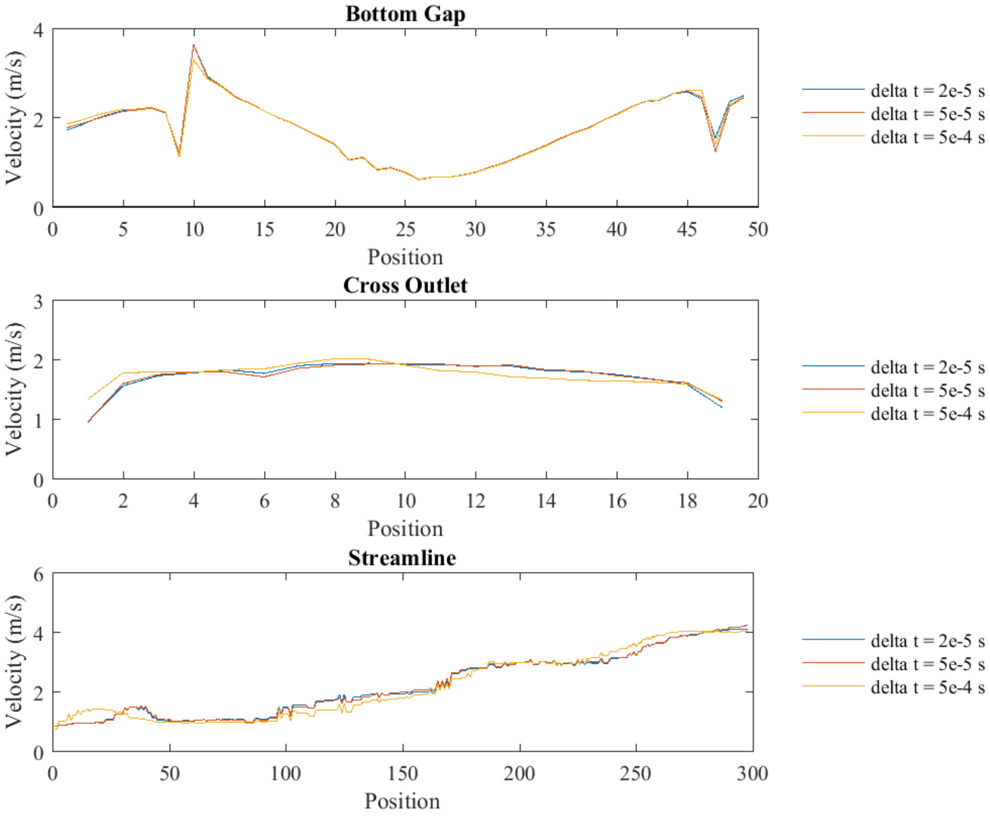

Supplementary Figure 13: Results of the time step independence study with respect to velocity. The three graphs represent the three geometric locations tested. The grid size in these simulations was 6.3 million cells. $\Delta t = 5\cdot10^{-5}$s was chosen for the study. Position refers to the geometrical position on the line probe.

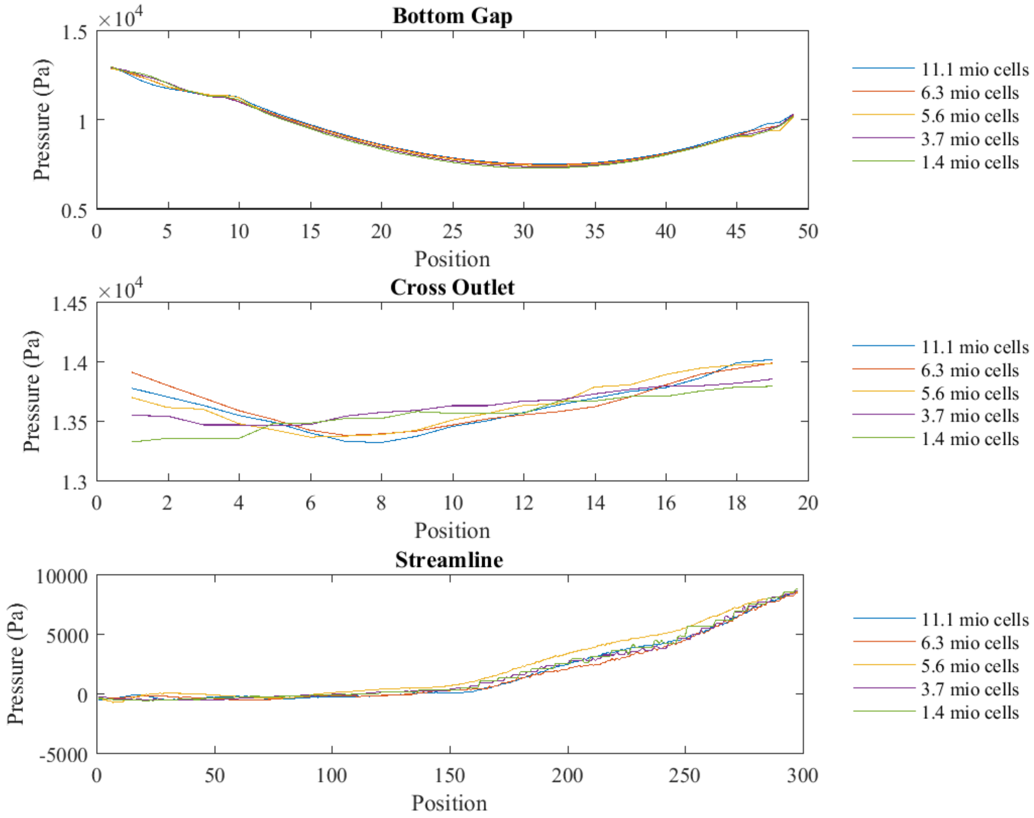

Supplementary Figure 14: Results of the grid independence study with respect to pressure. The three graphs represent the three geometric locations tested. The time step in these simulations was Δt = $5 \cdot 10^{-5}$ s. The mesh with 6.3 million cells was chosen for the study. Position refers to the geometrical position on the line probe.

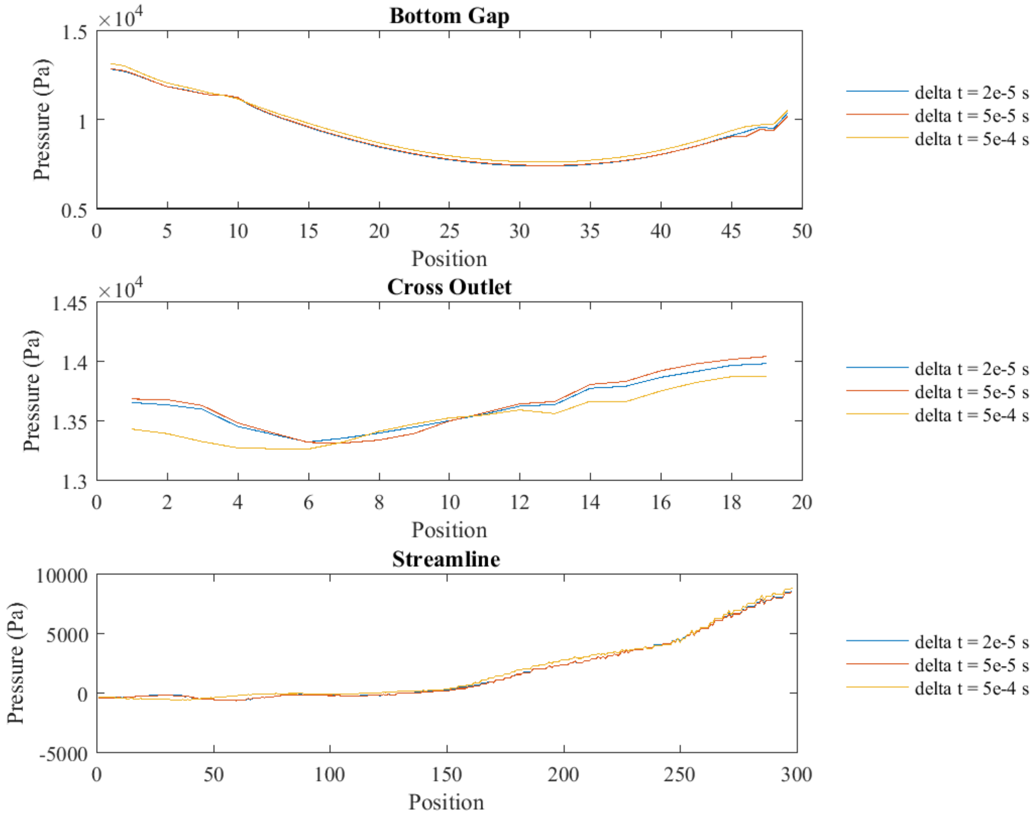

Supplementary Figure 15: Results of the time step independence study with respect to pressure. The three graphs represent the three geometric locations tested. The grid size in these simulations was 6.3 million cells. $\Delta t = 5 \cdot 10^{-5}$s was chosen for the study. Position refers to the geometrical position on the line probe.

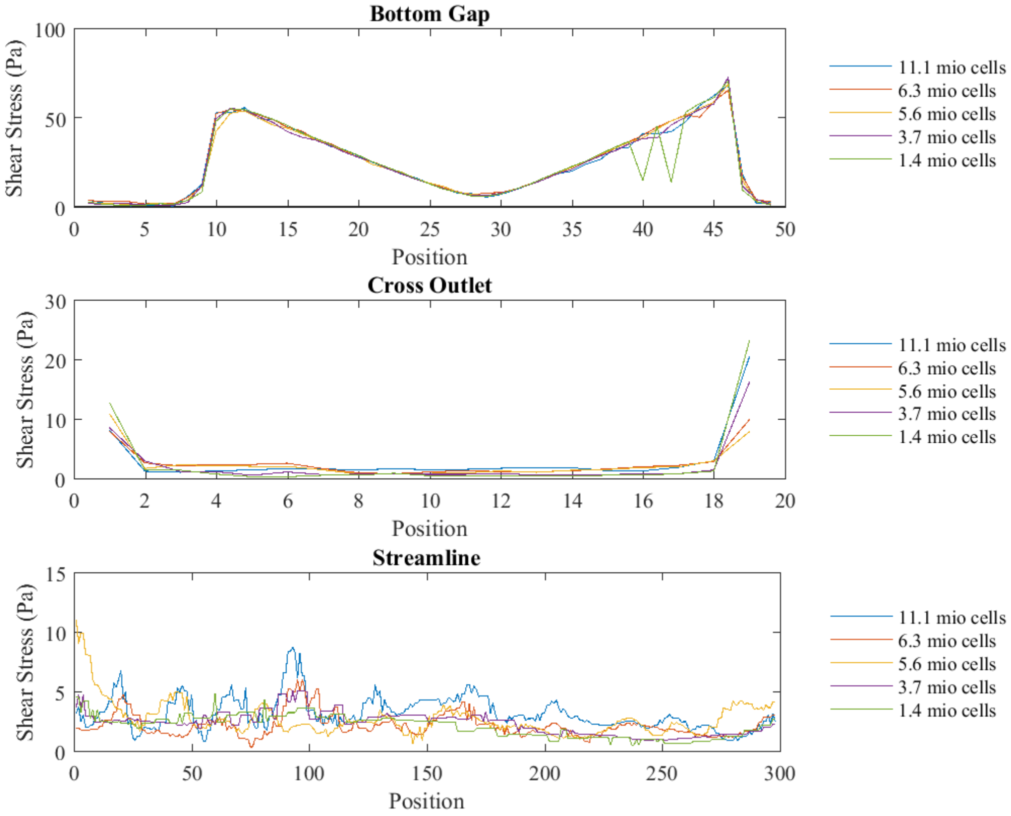

Supplementary Figure 16: Results of the grid independence study with respect to shear stress. The three graphs represent the three geometric locations tested. The time step in these simulations was $\Delta t = 5 \cdot 10^{-5}$ s. The mesh with 6.3 million cells was chosen for the study. Position refers to the geometrical position on the line probe.

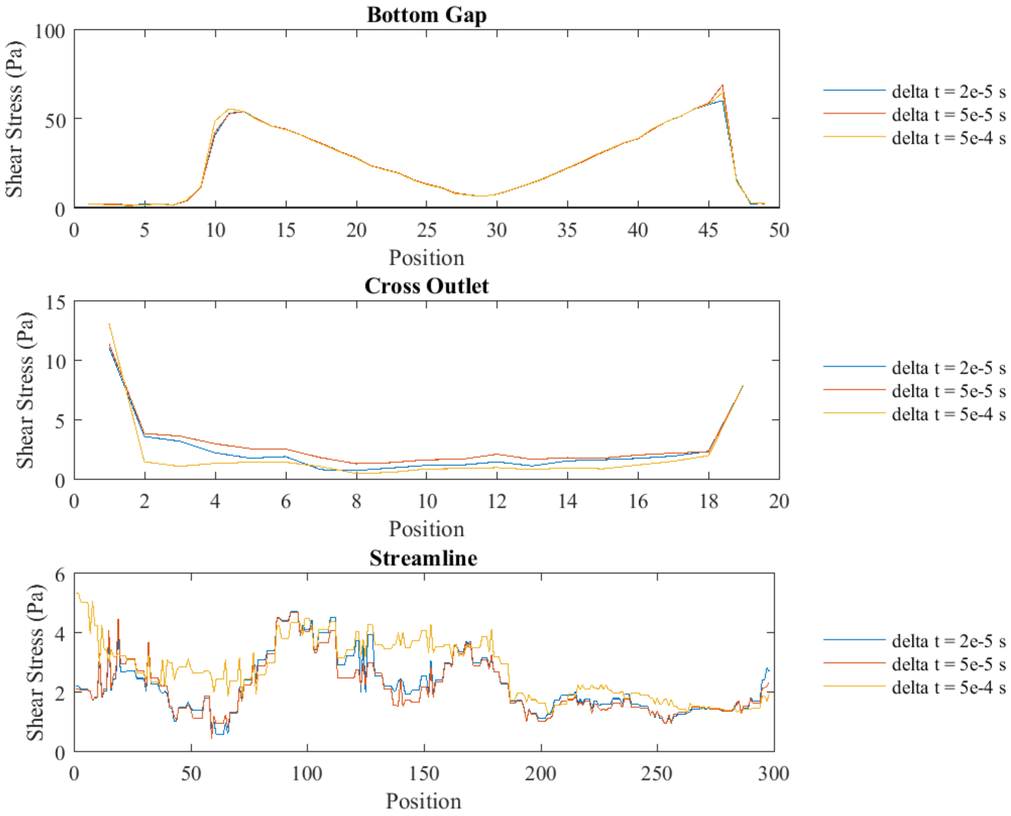

Supplementary Figure 17: Results of the time step independence study with respect to shear stress. The three graphs represent the three geometric locations tested. The grid size in these simulations was 6.3 million cells. Δt = $5 \cdot 10^{-5}$s was chosen for the study. Position refers to the geometrical position on the line probe.

3.6.3 Raw data hemocompatibility indicators

Geometries			**Hemolysis indicators**		**Thrombosis indicators**			**VWF cleavage**
Variation	Label acc. to Table 3	Geometry feature	HI	$I_{\tau>150Pa}$	$I_{\tau>50Pa}$	$I_{WSS<1Pa}$	SPWVI	$I_{\tau>9Pa}$
Clearance gap size	I	50 µm	3.20E-05	4.80E-04	1.11E-02	7.32E-03	361	1.46E-01
	II	150 µm	4.05E-05	3.82E-04	1.44E-02	3.76E-03	227	1.44E-01
	Baseline	300 µm	5.07E-05	3.64E-04	1.65E-02	2.81E-03	286	1.52E-01
	III	500 µm	5.51E-05	4.85E-04	1.52E-02	2.07E-03	542	1.57E-01
Number of blades	IV	4 blades	5.14E-05	2.94E-04	1.57E-02	1.72E-03	242	1.46E-01
	Baseline	5 blades	5.07E-05	3.64E-04	1.65E-02	2.81E-03	286	1.52E-01
	V	6 blades	4.87E-05	2.66E-04	1.87E-02	5.58E-03	449	1.60E-01
	VI	7 blades	5.84E-05	4.69E-04	1.87E-02	4.74E-03	459	1.66E-01
Shroud design	Baseline	Semi-open	5.07E-05	3.64E-04	1.65E-02	2.81E-03	286	1.52E-01
	VII	closed	5.59E-05	6.41E-05	2.25E-02	6.33E-03	329	1.54E-01

Supplementary Table 2: Effects of a change in clearance gap size (50 µm to 500 µm), number of blades (4 to 7), or shroud design (semi-open or closed) on hemocompatibility indicators – raw data. These data are also displayed, normalized by their respective values in the baseline configuration, in Figure 14: Effect of change in clearance gap size (50 µm to 500 µm), number of blades (4 to 7), and shroud design (semi-open or closed) on hemocompatibility indicators. Hemocompatibility indicators are grouped into three categories according to their suspected implications: (1) Hemolysis indicators are HI and $I_{\tau>150Pa}$. (2) Thrombosis potential is indicated by $I_{\tau>50Pa}$, rotor surface with $I_{WSS<1Pa}$ and SPWVI. (3) Bleeding potential due to VWF cleavage is assessed with $I_{\tau>9Pa}$. All indices are normalized by their respective values in the baseline configuration. Numerical values are listed in Supplementary Material C. Dashed frames indicate baseline configuration.of the manuscript. Footnote: HI: hemolysis index, $I_{\tau>150Pa}$: fluid volume with τ>150Pa/total fluid volume in the pump, $I_{\tau>50Pa}$: fluid volume with τ>50Pa/total fluid volume in the pump, $I_{WSS<1Pa}$: area on the rotor with WSS<1Pa/total surface area of the rotor, SPWVI: spanwise vorticity index, $I_{\tau>9Pa}$: fluid volume with τ>9Pa/total fluid volume in the pump.

3.6.4 Maximum shear stress histograms

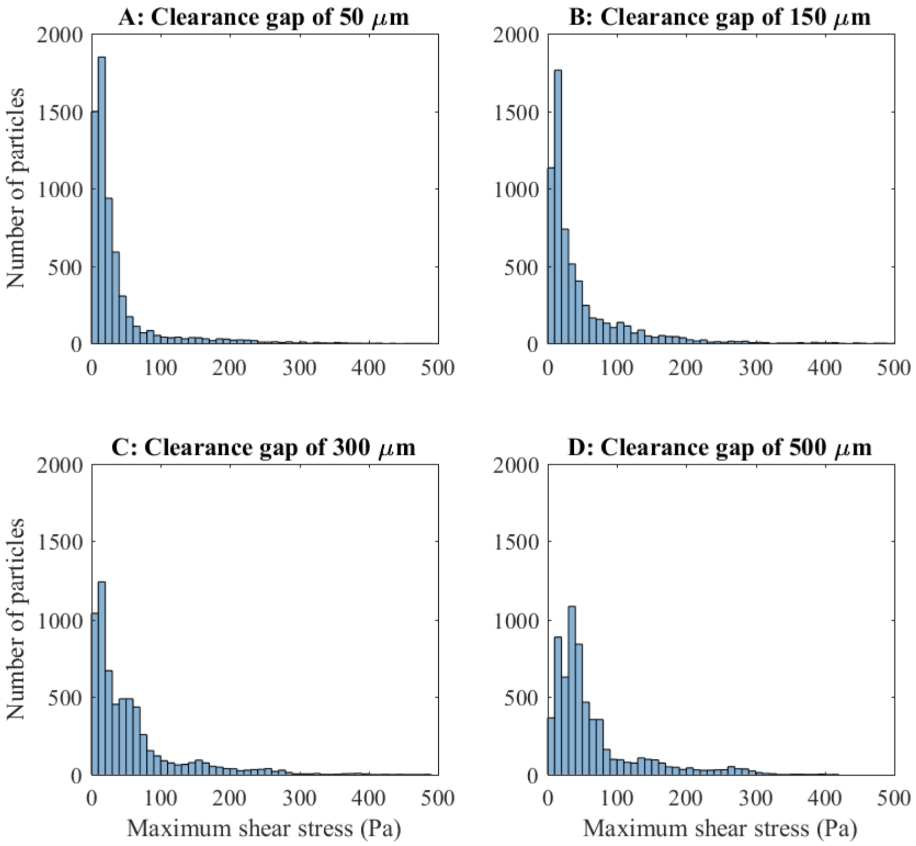

Supplementary Figure 18: Histograms of the maximal scalar shear stress experienced by each Lagrangian particle track depending on the clearance gap size. A: Clearance gap = 50 µm (geometry I). B: Clearance gap = 150 µm (geometry II), C: Clearance gap = 300 µm (geometry baseline), D: Clearance gap = 500 µm (geometry III). For optimal display, the x-axis shows maximum shear stresses between 0 and 500 Pa for all geometry variations. The maximum experienced shear stress was 694, 662, 486 and 418 Pa with the 50, 150, 300 and 500 µm gap sizes, respectively.

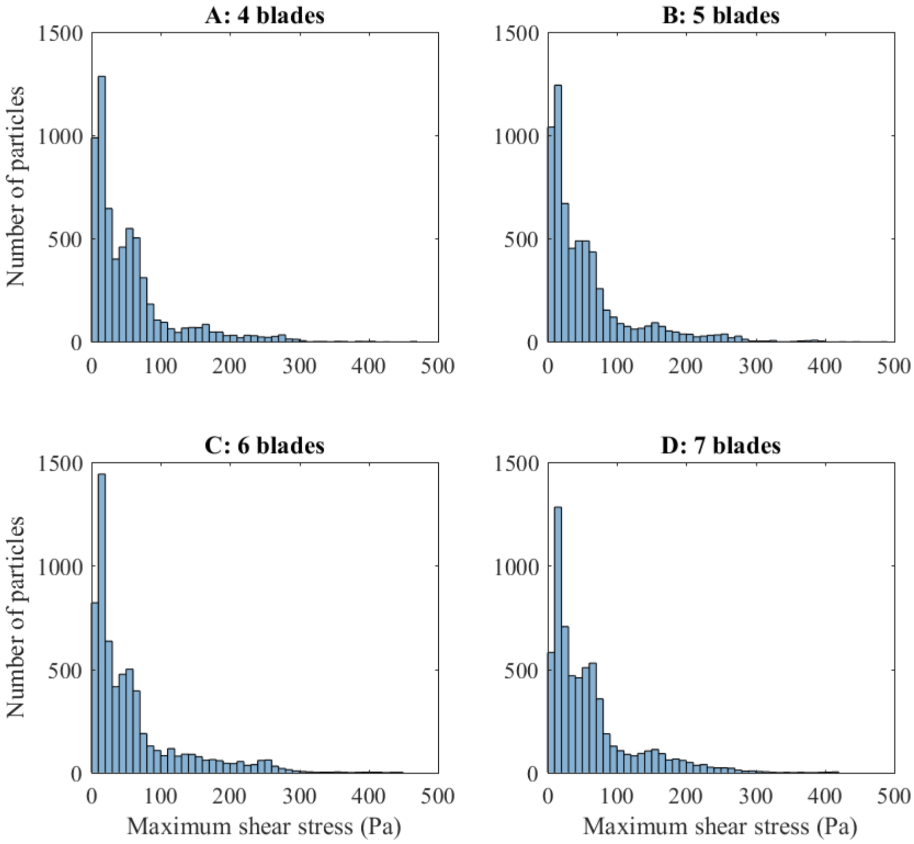

Supplementary Figure 19: Histograms of the maximal scalar shear stress experienced by each Lagrangian particle track depending on the number of blades. A: 4 blades (geometry IV), B: 5 blades (geometry baseline), C: 6 blades (geometry V), D: 7 blades (geometry VI). For optimal display, the x-axis shows maximum shear stresses between 0 and 500 Pa for all geometry variations. The maximum experienced shear stress was 468, 486, 440 and 414 Pa with 4, 5, 6 and 7 blades, respectively.

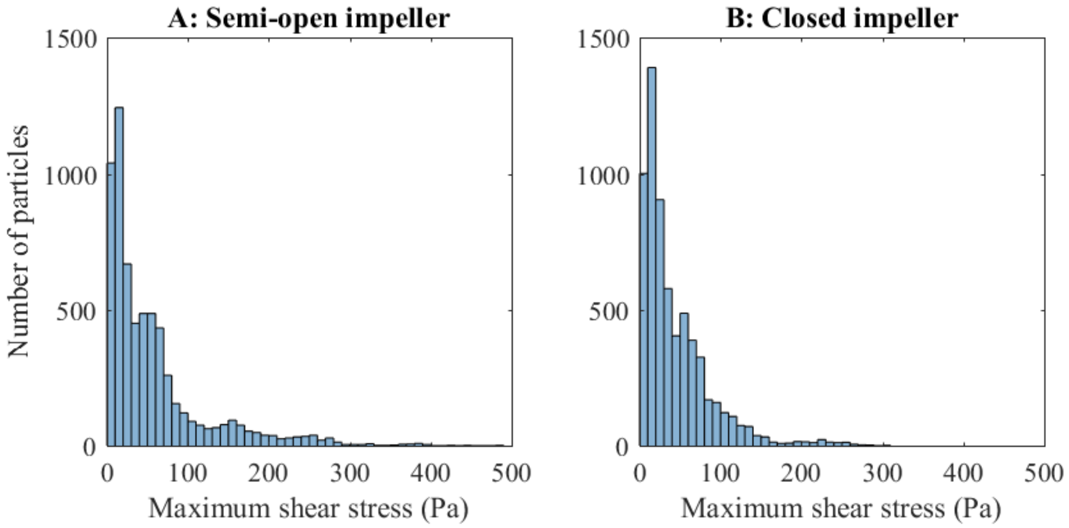

Supplementary Figure 20: Histograms of the maximal shear stress experienced by each Lagrangian particle track depending on the shroud design. A: semi-open impeller (geometry baseline), B: closed impeller (geometry VII). For optimal display, the x-axis shows maximum shear stresses between 0 and 500 Pa for all geometry variations. The maximum experienced shear stress was 486 and 303 for the semi-open and closed shroud design, respectively.

4 Fluid dynamics in the HeartMate 3: Influence of the artificial pulse feature and residual cardiac pulsation

This chapter has been submitted for publication to *Artificial Organs.*

4.1 Abstract

Ventricular assist devices (VADs), among which the HeartMate 3 (HM3) is the latest clinically approved representative, are often the therapy of choice for patients with end-stage heart failure. Despite advances in the prevention of pump thrombi, rates of stroke and bleeding remain high. These complications are attributed to the flow field within the VAD, among other factors. One of the HM3's characteristic features is an artificial pulse that changes the rotor speed periodically by 4000 rpm, which is meant to reduce zones of recirculation and stasis. In this study, we investigated the effect of this speed modulation on the flow fields and stresses using high-resolution computational fluid dynamics. To this end, we compared Eulerian and Lagrangian features of the flow fields during constant pump operation, during operation with artificial pulse feature and with the effect of the residual native cardiac cycle. We observed good washout in all investigated situations, which may explain the low incidence rates of pump thrombosis. The artificial pulse had no additional benefit on scalar washout performance, but it induced rapid variations in the flow velocity and its gradients. This may be relevant for the removal of deposits in the pump. Overall, we found that viscous stresses in the HM3 were lower than in other current VADs. However, the artificial pulse substantially increased turbulence, and thereby also total stresses, which may contribute to clinically observed issues related to hemocompatibility.

Keywords: ventricular assist devices, HeartMate 3, computational fluid dynamics, artificial pulse, cardiac cycle, hemocompatibility

4.2 Introduction

The HeartMate 3 (HM3, Abbott, St. Paul, MN, USA) is the latest clinical ventricular assist device (VAD) designed for long-term support of patients with advanced heart failure. It is characterized by a magnetic levitation system, textured blood-contacting surfaces, wide flow gaps and an artificial pulse [4]. Together, these features shall enhance the hemocompatibility of the pump and reduce thrombotic and hemorrhagic adverse events. Clinical results so far suggest that the HM3 decreases incidence rates of pump thrombosis and stroke compared to the HeartMate 2 (Abbott), while the rates of disabling stroke are similar [45]. Bleeding rates are comparable to other VADs [45], [222], even though the HM3 appears to preserve high molecular weight von Willebrand factor (VWF) multimers better than other clinically used VADs [223].

Hemocompatibility is linked to the blood flow within the VAD. This includes regions of stagnation and recirculation that may promote thrombus formation [218], as well as high shear areas that may activate platelets [96] and reduce VWF functionality [108]. It has been hypothesized that the HM3's artificial pulse improves pump washout [4] and thereby inhibits pump thrombus formation. However, this hypothesis has not been tested so far. Further, while rotary blood pumps typically operate at a constant speed, maintaining some pulsatility has been hypothesized to have positive effects on the vasculature [69]. Evidence on the beneficial effect of periodic speed changes has been provided by comparative studies in patients with an HVAD (Medtronic, Minneapolis, MN, USA), which features an optional periodic speed modulation. Patients with the modulation enabled had significantly fewer rates of stroke, sepsis and right heart failure than those without, while overall survival and gastrointestinal bleeding rates were not affected [35].

The HM3's artificial pulse comprises a decrease of the pump speed by 2000 rpm, followed by an increase by 4000 rpm, before operation at nominal speed is resumed. This pulse lasts 350 ms and is repeated every 2 seconds. While the flow inside the HM3 has been investigated under steady conditions [4], the effects of the rapid change in rotor speed on the flow and corresponding stress fields have not. Given the severity of the modulation of pump operation, we view it as imperative to understand its influence on blood flow and to consider effects on blood components along with potential downstream consequences.

To contribute to this understanding, we utilized computational fluid dynamics (CFD) and investigated the haemodynamic characteristics of the artificial pulse in absence of any remaining cardiac function, and of cardiac pulsatility without artificial pulse, comparing both to a baseline with neither native nor artificial pulsatility. Our CFD framework includes high-resolution dynamic flow simulations in the VAD and a lumped parameter representation of the cardiovascular system including the pump. We have analyzed the computed data with respect to Eulerian and Lagrangian characteristics linked to blood damage and thrombosis potential, and juxtaposed the results to clinical findings.

4.3 Methods

We simulated three different scenarios: The first one considers a remaining cardiac function and a HM3 operating without the artificial pulse feature with constant speed for a full cardiac cycle (hereinafter referred to as “cardiac cycle”). The second one considers no native heart function, but includes the HM3 artificial pulse (“artificial pulse”). The final one represents the baseline case with constant HM3 speed and no native heart function (“baseline”). We set pump speeds to maintain a mean cardiac output of 5 L/min [224] in all three scenarios. Boundary conditions (BCs) for the flow computations in the VAD were obtained from a lumped parameter representation of the entire cardiovascular system, including the pump.

4.3.1 Geometry

An explanted HM3 pump was scanned using an X-ray micro computed tomography system (MicroDETECT, Empa, Zurich, Switzerland) as in [12]. The resulting pixel size was 30 µm. The obtained images were segmented using Mimics (Materialise, Leuven, Belgium) and reconstructed in Solidworks (Dassault Systèmes, Waltham MA, USA). The identified top and bottom gaps between rotor and housing are 1 mm and 1.75 mm, respectively.

4.3.2 Computational fluid dynamics simulations

CFD simulations were carried out using StarCCM+ (Siemens, Munich, Germany). Polyhedral grids were generated for all parts of the domain except inlet and outlet cannulas, including an eight-element boundary layer along the walls in the rotating part and a ten-element boundary layer in the volute. Local mesh refinement was performed where needed. In the inlet cannula and outlet graft, a structured mesh was generated. The final grid contained 9.95 million cells.

The three-dimensional unsteady Reynolds-averaged Navier-Stokes equations were solved using implicit second order temporal and spatial discretization, a segregated flow approach and k-ω-SST turbulence modeling. Inlet turbulent boundary conditions were prescribed based on relationships for fully developed turbulent pipe flow, namely turbulent intensity = $0.16 \cdot Re^{1/8} = 0.06$ and turbulent length scale = $0.07 \cdot D = 1.33$ mm, with D being the diameter of the inlet cannula. Blood was modelled as a Newtonian fluid with a viscosity of 3.5 mPa·s and a density of 1050 kg/m^3. This simplification was considered acceptable, as the non-Newtonian properties of blood, such as shear-thinning, become negligible at high shear rates (> 100 s^{-1}) [141] such as those typically found in VADs. The rotation of the impeller was implemented as a rigid body motion. Pressure boundary conditions were prescribed at the inlet and outlet. For the cardiac cycle and artificial pulse simulations, the time-dependent pressure BCs were obtained from the corresponding lumped-parameter simulations.

All simulations were carried out with a convergence criterion of 10^{-5} for the residual errors and a time step corresponding to 2° of rotation. For the artificial pulse, the time step was kept constant at the smaller value during the ramping time, corresponding to 2° at the higher speed. Grid and time step independence were confirmed for pressure, velocity, and shear stresses as reported in the supplementary material.

4.3.3 Lumped parameter model

Pressure BCs were obtained from a lumped parameter model of the entire circulation, including a mathematical representation of the dynamic response of the HM3. A numerical model similar to previously reported ones [225]–[228] was employed to simulate the cardiovascular system. The heart was modeled as having a time-varying elastance with nonlinear end-diastolic/end-systolic pressure-volume relationships and unidirectional valves as suggested in Colacino et al. [225]. Arterial and venous vasculatures were modeled as 3- and 2-element Windkessel models [229], respectively. Cardiovascular parameters were adapted to mimic the ones of an average LVAD patient [224]. The mathematical representation of the HM3 was derived from in vitro experiments similar to [230], [231]. The in vitro experiments were conducted on the mock loop setup described in [161]. A 15 cm long outlet graft, which is within the range of graft lengths found in patients [232], was included as hydraulic resistance and inertance between the pump outlet and aorta. That graft was subdivided into two compartments, respectively accounting for the first 7 cm and subsequent 8 cm of the graft, allowing for the extraction of the pressure boundary conditions 7 cm away from the pump for the CFD simulations.

4.3.4 Simulation "baseline"

In the baseline case, we investigated the flow in the HM3 at a constant speed and no influence of the native circulation. The pump was operated at 5650 rpm and 80 mmHg. For assessment of the washout performance, CFD calculations were carried out for 40 full rotations.

4.3.5 Simulation "cardiac cycle"

In the cardiac cycle simulation, the HM3 was run at a constant speed of 5250 rpm and the effect of physiologic pressure pulsations induced by native heart function on the flow field within the VAD were investigated. Appropriate dynamic behavior was ensured by initialization over two full cardiac cycles, run with a time step of 4° to reduce computational effort. After initialization, one full cardiac cycle (0.658 s at 91.2 bpm [224] , corresponding to approximately 58 full rotations) was calculated with a time step size corresponding to 2°.

4.3.6 Simulation "artificial pulse"

In the artificial pulse simulation, the effect of the HM3 speed modulation on the flow field within the VAD was investigated. The system was initialized at 5650 rpm and a flow of 5 L/min, before the speed and pressure BCs including the speed change were prescribed for a total duration of 670 ms, corresponding to approximately 59 full rotations.

4.3.7 Analyses

We analyzed various Eulerian and Lagrangian features of the flow field both qualitatively and quantitatively. We calculated the scalar viscous shear stress, τ_{visc}, from the viscous shear stress components, σ_{ij}, according to [216], [233]:

$$\tau_{visc} = \left[\frac{1}{12}\sum\left(\sigma_{ii} - \sigma_{jj}\right)^2 + \frac{1}{2}\sum \sigma_{ij}^2\right]^{1/2} \tag{10}$$

Similarly, we calculated a scalar total shear stress, τ_{tot}, including turbulent stresses as

$$\tau_{tot} = \left[\frac{1}{12}\Sigma\left((\sigma_{ii} + s_{ii}) - (\sigma_{jj} + s_{jj})\right)^2 + \frac{1}{2}\Sigma\left(\sigma_{ij} + s_{ij}\right)^2\right]^{1/2}, \tag{11}$$

with the components of the Reynolds stress tensor s_{ij} given by

$$s_{ij} = -\rho \cdot \overline{u_i' u_j'} = -\frac{2}{3}\rho k \delta_{ij} + \mu_t\left(\frac{\partial u_i}{\partial x_j} + \frac{\partial u_j}{\partial x_i}\right), \tag{12}$$

where ρ is density, $u'$is the fluctuating component of the mean fluid velocity, k is turbulent kinetic energy, δ_{ij} is the Kronecker delta, μ_t is turbulent viscosity and u is mean fluid velocity.

To probe blood cell paths through the pump, we implemented Lagrangian particle tracking with passive advection. The tracked particles had a diameter of 5 µm and a density of 1125 kg/m^3, which are representative of, respectively, the dimension and density of red blood cells. At least 798 particles were seeded 44 mm downstream of the inlet with uniform spatial distribution at multiple instances in time. We confirmed that the derived metric (exposure time to stress above a specific threshold) did not depend on the number of tracked particles (supplementary material).

To investigate washout, we quantified advection of a passive scalar Φ:

$$\begin{gathered}\rho\frac{\partial \phi}{\partial t} + \rho\nabla \cdot (u\phi) = S_\phi(t) \\ S_\phi(t) = \begin{cases} 100\,, t = t_0 \\ 0, t \neq t_0 \end{cases}\end{gathered} \tag{13}$$

where t is time, S_Φ is a source term and t_0 is the scalar initialization time.

4.4 Results

4.4.1 Hydraulic data

To confirm that the imposed BCs result in the desired fluid dynamic behavior, we compared the flow curves obtained with CFD to corresponding data obtained using the lumped parameter model (Figure 19). Overall, the CFD and LP model data agree well (root mean square error of 6% and 10% for the cardiac cycle and artificial pulse, respectively). The arterial pulse pressures in the cardiac cycle and artificial pulse simulations are 5 mmHg and 11 mmHg, respectively.

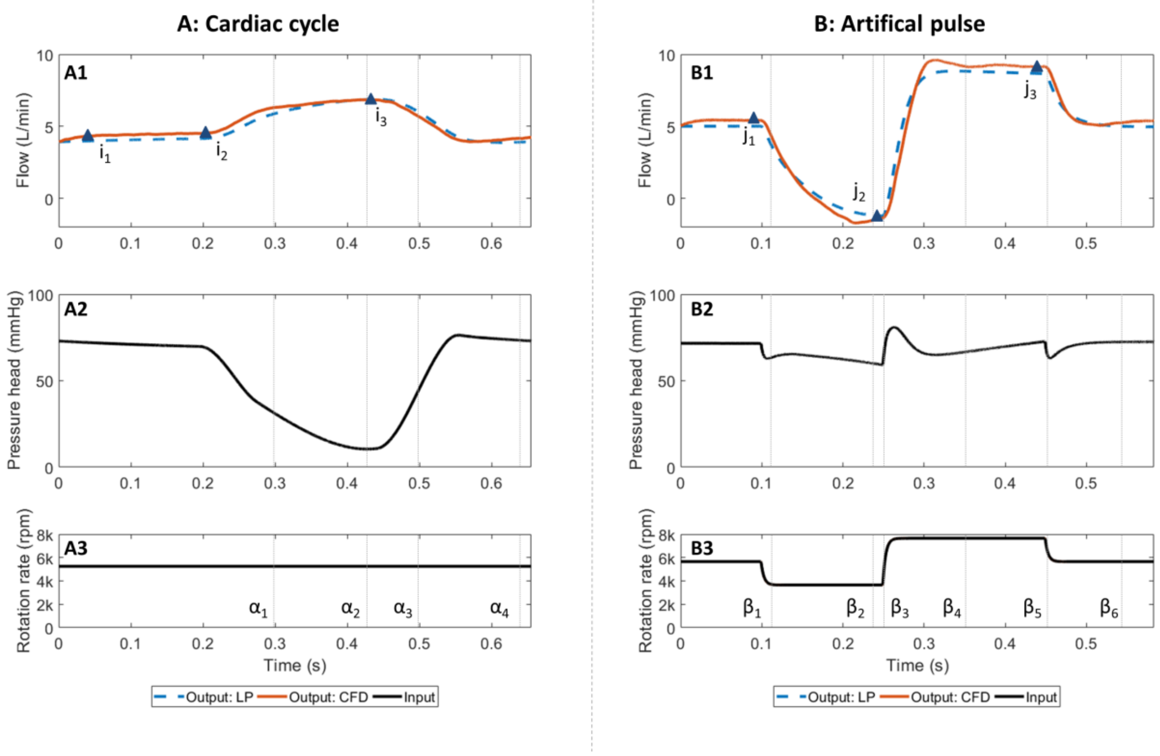

Figure 19: Calculated flow rates and corresponding model input in the ‘cardiac cycle’ (Panels A) and ‘artificial pulse’ scenarios (Panels B). Flow rates calculated using the lumped parameter (LP) and CFD models are shown in Panels 1 (dashed and solid lines, respectively). Pressure head and rotation rate were prescribed as model input (Panels 2 and 3). α_1- α_4 and β_1- β_6 indicate time points selected to visualize the flow structures in subsequent figures. i_1-i_3 and j_1-j_3 indicate injection time points for Lagrangian particles highlighted in Figure 23.

4.4.2 Flow field (velocity & vorticity)

To understand flow features inside the pump, we started by investigating the ‘baseline’ scenario (constant speed and constant BCs). Here, areas of flow detachment are observed at the pressure side and the trailing edges of the blades (Figure 20B, markers I & II). An area of stagnation forms centrally under the rotor (III). Vorticity is increased in regions of recirculation or flow detachment at the pressure side and trailing edges of the blade, in the gaps (IV), as well as at the tongue (V), depending on blade position (Figure 20D). In addition, we observe flow features similar to a wavy vortex flow in the side gap between rotor and housing (Figure 20C). The regions of flow detachment and wavy vortex pattern remain present during the entire rotation and occur at all tested quasi-steady flow situations (incl. the high flow/high speed plateau in the ‘artificial pulse’ scenario).

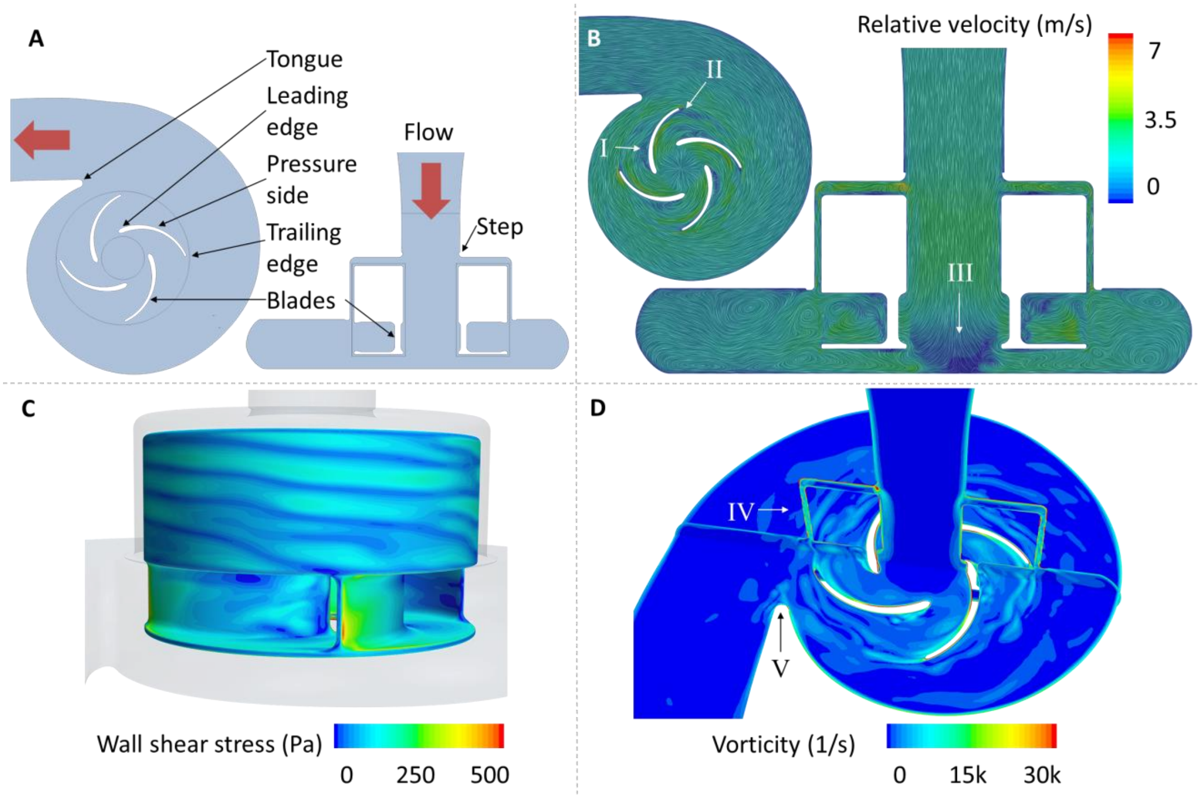

Figure 20: General characteristics of the HM3 hemodynamics in the ‘baseline’ scenario. A: Geometry features. B: Relative velocity. Areas of flow detachment are observed at the pressure sides (I) and the trailing edges (II) of the blades. An area of stagnation forms centrally under the rotor (III). C. Wall shear stress (WSS) on the rotor surface. Highest WSS occurs at the trailing edges. In the gap, a WSS pattern caused by wavy vortex-like flow is observed. D. Vorticity is increased in regions of recirculation or flow detachment at the pressure side and trailing edges of the blade, in the gap (IV), as well as at the tongue (V), depending on blade position.

Next, we explored the influence of unsteady pump operation. In the ‘cardiac cycle’ scenario, some destabilization occurs during systole (Figure 21A). The area of low flow under the rotor shifts towards the outlet during high flow.

The speed decrease of the artificial pulse severely destabilizes the flow, leading to multiple vortices (Figure 21B). Vortices form in the blade channels and centrally between their leading edges. Vortical structures are particularly present close to the rotating body and travel towards the inlet cannula during backflow. The subsequent speed increase leads to an overall stabilization of the flow. The final speed change from top speed back to nominal leads to the anticipated overall reduction of velocities, but not to the formation of major vortices.

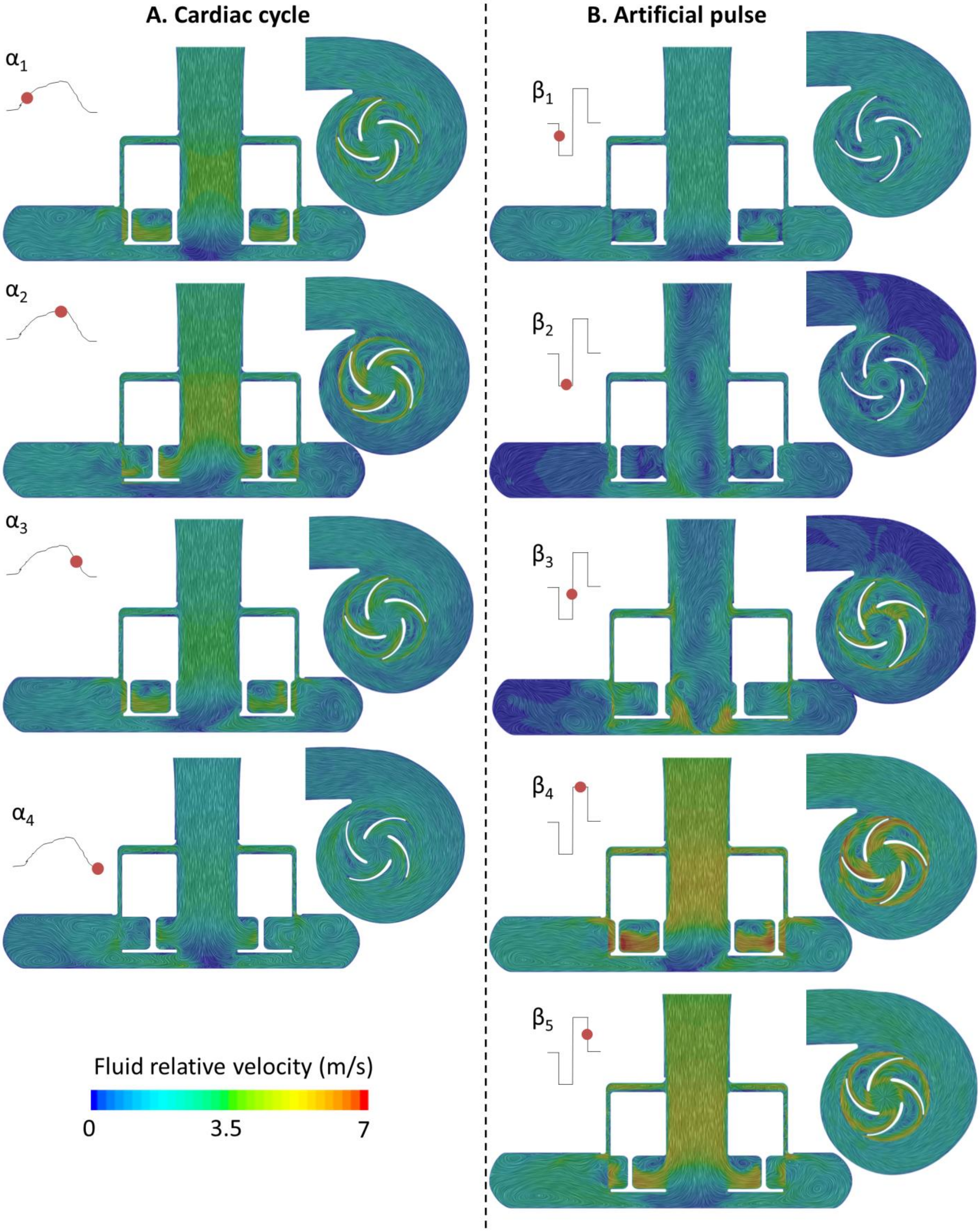

Figure 21: Relative velocities at selected time points α_1-α_4 (Panel A, 'cardiac cycle' scenario) and β_1-β_5 (Panel B, 'artificial pulse' scenario) as defined in Figure 19. Relative velocities are visualized in supplementary videos 1 to 6 for all scenarios.

4.4.3 Turbulence and vortical structures

Turbulence is suspected to influence blood damage [234]. Turbulence content is substantially higher in the ‘artificial pulse’ compared to the other two scenarios, as highlighted by the substantially increased total stresses (Figure 22). Vortices build especially during deceleration of the rotor and low flow or backflow conditions.

4.4.4 Stresses

Since damage to blood components is caused, among other factors, by a combination of high stresses and exposure times [174], we assessed both Eulerian stress levels and computed heat maps visualizing time-dependent aspects.

In the ‘baseline’ scenario, highest viscous stresses are observed at the trailing edges, in the side gaps and at the transition from top gap to the main flow path (Figure 22A). Total stresses are highest in the blade channels and the narrowest part of the volute, while they are slightly elevated in the volute towards the outlet. In the ‘cardiac cycle’ scenario, overall viscous and total stress levels within the rotor increase. Peak total stresses are observed at the pressure side of the blades, the top part of the blade trailing edges and the tongue (Figure 22B). In the ‘artificial pulse’ scenario, viscous stress levels in the rotor decrease during the period of low flow and increase during high rotational speed (Figure 22C). Total stresses in the rotor and volute rise considerably during the period of low flow, and zones of elevated stresses are also located towards the inlet. At the time of the increase in rotor speed, large parts of the rotor experience total stresses > 100 Pa. Overall levels of total stress decrease only as the system returns to nominal conditions. The difference in total stress levels between the three investigated scenarios is also visualized in Figure 22D, which displays the fluid volume exposed to total stresses > 150 Pa.

A Lagrangian perspective allows the assessment of exposure times in addition to stress magnitudes, which is highlighted in Figure 23. Table 6 summarizes the fraction of particles exposed to stresses above thresholds of 9, 50 and 150 Pa, which have been suggested to be indicative of different types of blood damage [174] and are useful as comparative metrics between different operating conditions or pump designs [181].

	Viscous stresses			Total stresses		
	Baseline (%)	Cardiac cycle (%)	Artificial pulse (%)	Baseline (%)	Cardiac cycle (%)	Artificial pulse (%)
$\boldsymbol{\tau_{thres} = 9\ Pa}$	83	81	88	99	99	100
$\boldsymbol{\tau_{thres} = 50\ Pa}$	34	30	40	36	37	90
$\boldsymbol{\tau_{thres} = 150\ Pa}$	5	5	10	5	5	39

Table 6: Fraction of particles (%) exposed to $\boldsymbol{\tau > \tau_{thres}}$ in the 'baseline', 'cardiac cycle' and 'artificial pulse' scenarios. For the 'cardiac cycle' and the 'artificial pulse' scenario, the numbers represent the arithmetic mean of the fraction of exposed particles across all sets of tracks. "Exposed particles" refers to particles that were exposed to stresses above the threshold at least once. Each set of particle tracks corresponds to one injection time (as highlighted in Figure 19) and the individual values per injection time are reported in the supplementary material.

In the 'cardiac cycle' scenario, the fraction of particles exposed to viscous and total stresses above 50 and 150 Pa (Table 6) as well as the corresponding exposure times (Figure 23, B2 and B3) are similar, highlighting the small contribution of Reynold stresses. For the artificial pulse case, total stresses are considerably higher than viscous ones, resulting in a shift to higher total stress values and longer exposure times (Figure 23, C3). This is also reflected in the increased number of particles exposed to total stresses above the selected threshold as compared to viscous stresses (Table 6).

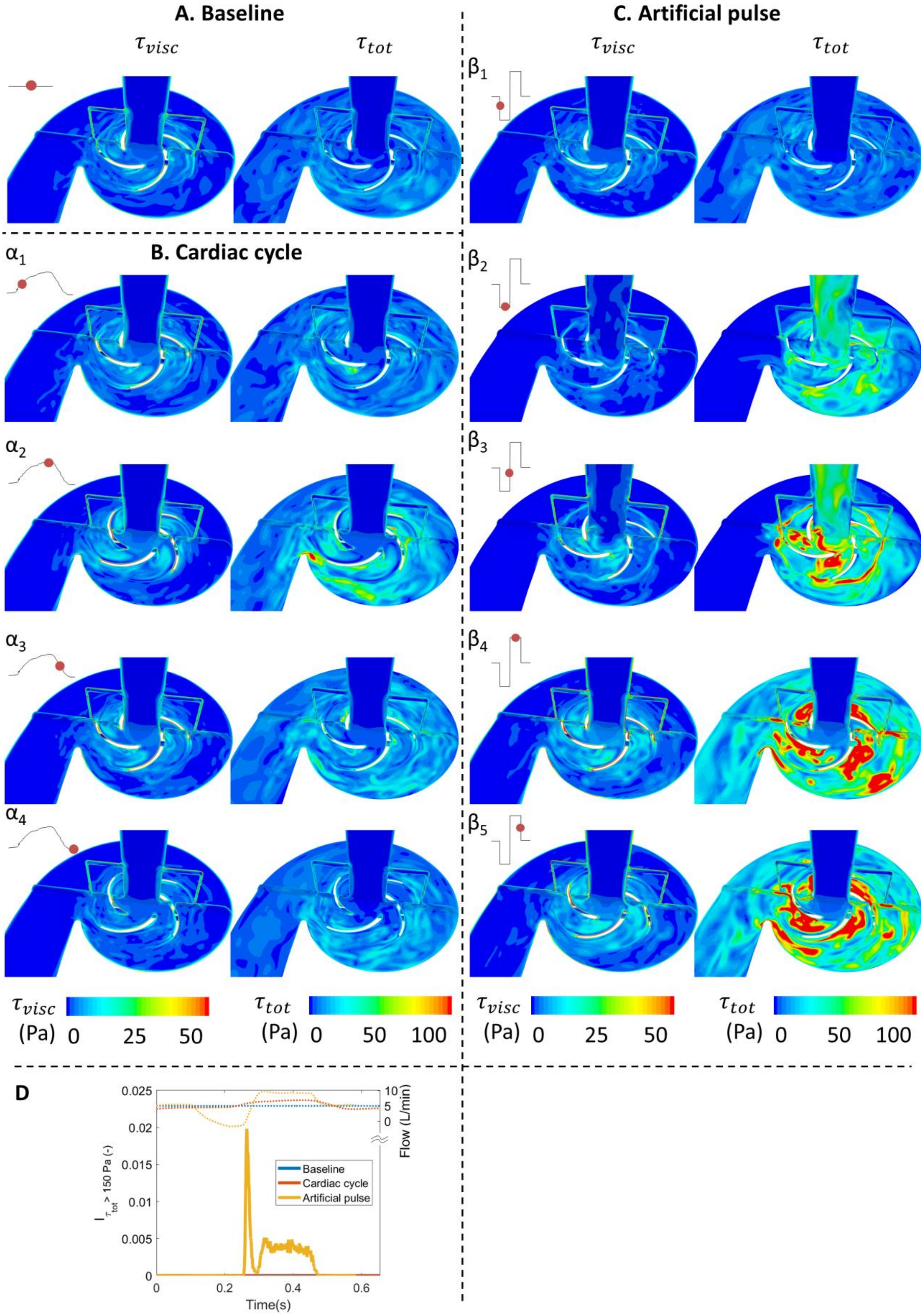

Figure 22: Viscous and total stresses in the ‘baseline’ (Panel A), ‘cardiac cycle’ (Panel B) and ‘artificial pulse’ scenarios (Panel C) at selected time points as defined in Figure 19. Note the different scales for viscous and total stresses. D: Fraction of fluid volume with τ_{tot} > 150 Pa. Values for the ‘baseline’ and ‘cardiac cycle’ scenarios are $1.9\cdot10^{-5}$ and $1.6\cdot10^{-5}$, respectively, thus too small to be visible here. The pump flow rate (values on right vertical axis) is plotted with dotted lines to aid interpretation.

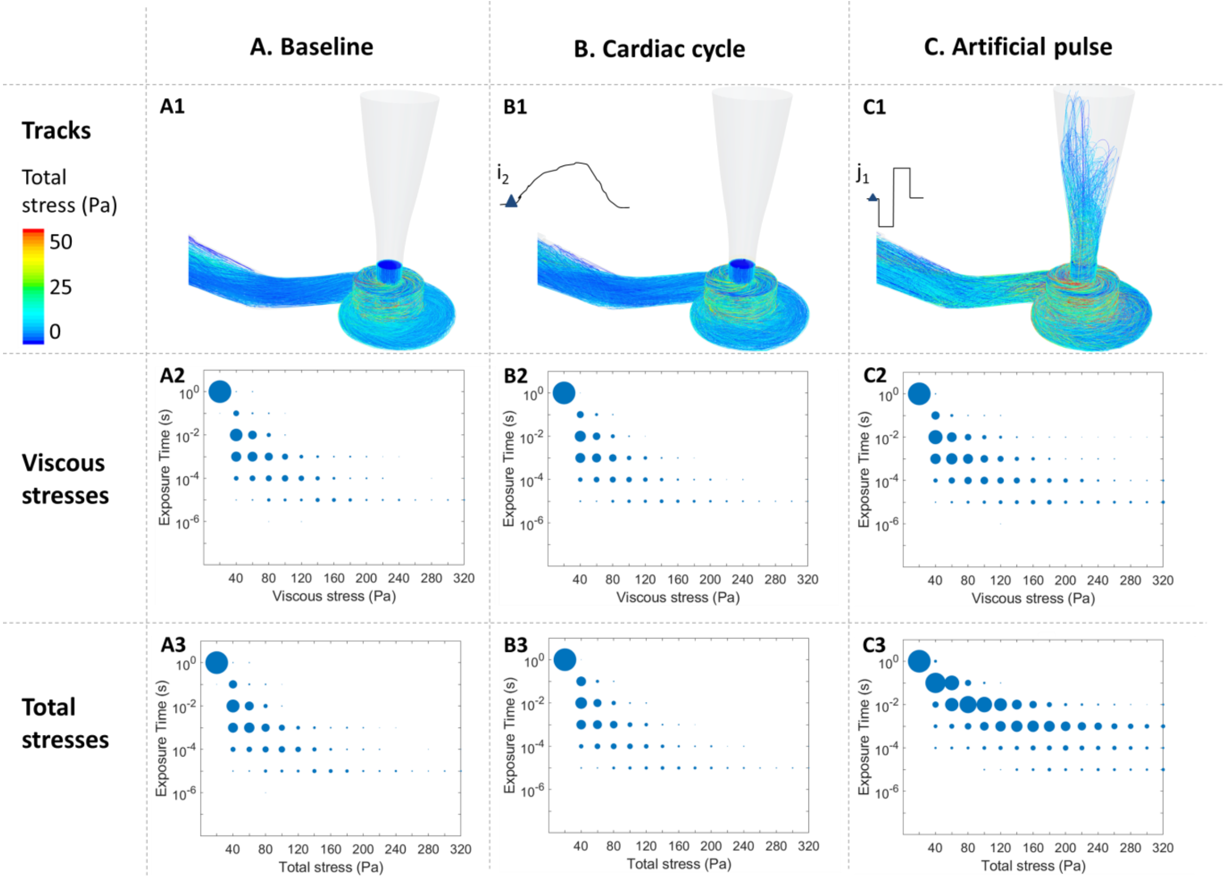

Figure 23: Lagrangian track data in the 'baseline' (Panels A), 'cardiac cycle' (Panels B) and 'artificial pulse' scenarios (Panels C). Panels 1: Particle tracks are colored according to the experienced total stress. In all cases, particles are injected on the same plane. I_2 and j_1 indicate the corresponding injection point for the Lagrangian particles. For the artificial pulse case, the effect of backflow is evident as the particles are advected back towards the inlet. Panels 2: Heat maps of exposure times and viscous stresses. The stresses are binned in intervals of 20 Pa (e.g. $100 \text{ Pa} < \tau < 120 \text{ Pa}$), and the exposure time of each track to levels of stress in each bin is calculated. The exposures times are then binned in a logarithmic manner (e.g. $10^{-3} < t < 10^{-2}$). The sizes of the circles represent the number of entries per time and stress bin. Panels 3: Heat maps of exposure times and total stresses. In this figure, only the results of one set of tracks are displayed per simulation. The respective injection times are indicated in B1 and C1. Results for the other sets of tracks look qualitatively similar and are available in supplementary figures 9 and 10.

4.4.5 Washout

To test washout behavior, which is presumably relevant for thrombus formation, we analyzed the relative content of a passive scalar. We found that scalar washout of the HM3 is generally good (95% washout after 26 rotations in the cardiac cycle case, Figure 24A), including also the stagnation area below the rotor observed during constant pump operation (Figure 20A). However, there remains a detachment area with poor washout downstream of the kink in the outlet graft (Figure 24B). In the 'artificial pulse' scenario, backflow leads to particle movement in reverse direction towards the inlet, and increases the time until the passive scalar has left the domain. Washout is visualized in supplementary videos 7 to 9.

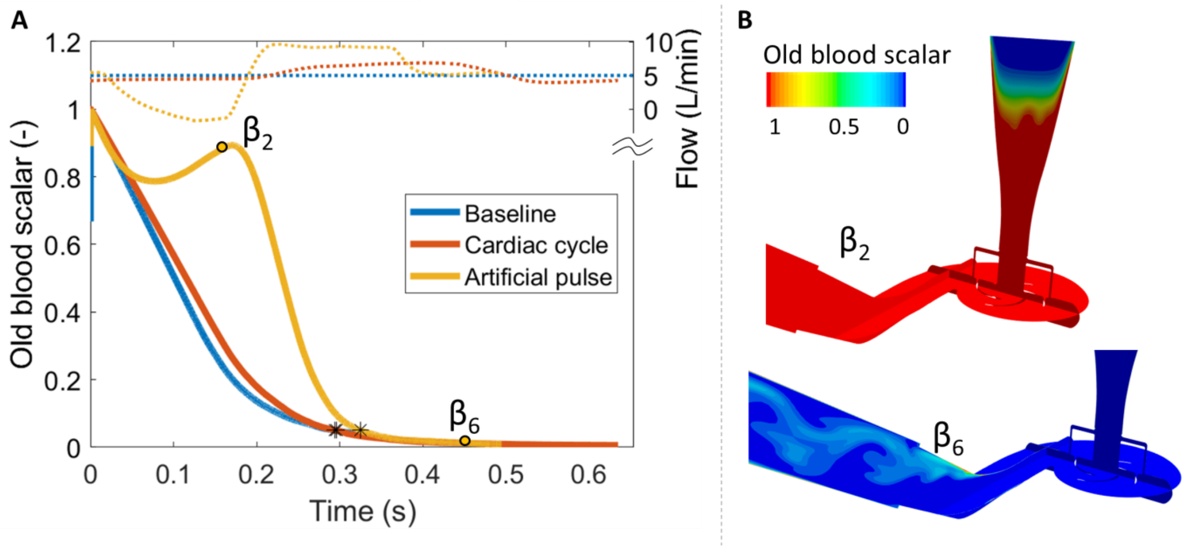

Figure 24: Passive scalar washout. A. Relative content of the passive scalar (labeled 'Old blood scalar') in the domain. The asterisks indicate the time point of 95% washout. The time scale is relative to the time point of initialization of the passive scalar. The pump flow rate is plotted with dotted lines to aid interpretation (values on right vertical axis). B. Visualizations of old blood scalar content at two selected time points (β_2, β_6) as defined in Figure 19.

4.4.6 Stagnation and recirculation

Since zones of stagnation and recirculation negatively affect hemocompatibility, we qualitatively and quantitatively assessed their extent. In the 'baseline' scenario, areas of stagnation are observed at the small step (labelled as "Step" in Figure 20A) at the transition site from inlet cannula to volute (Figure 25A, I), at the end of the secondary flow path (II), centrally under the rotor (III), at the bottom of the rotor close to the inner edge (IV) and at the volute wall (V). In the 'cardiac cycle' scenario, the extent of low velocity zones ($v < 0.2$ m/s) remains relatively constant (Figure 25B-C), whereas in the 'artificial pulse' scenario, the volumes of low velocity peak to 12 times the 'baseline' scenario value during backflow conditions and almost vanish at high rotor speed (Figure 25C-E).

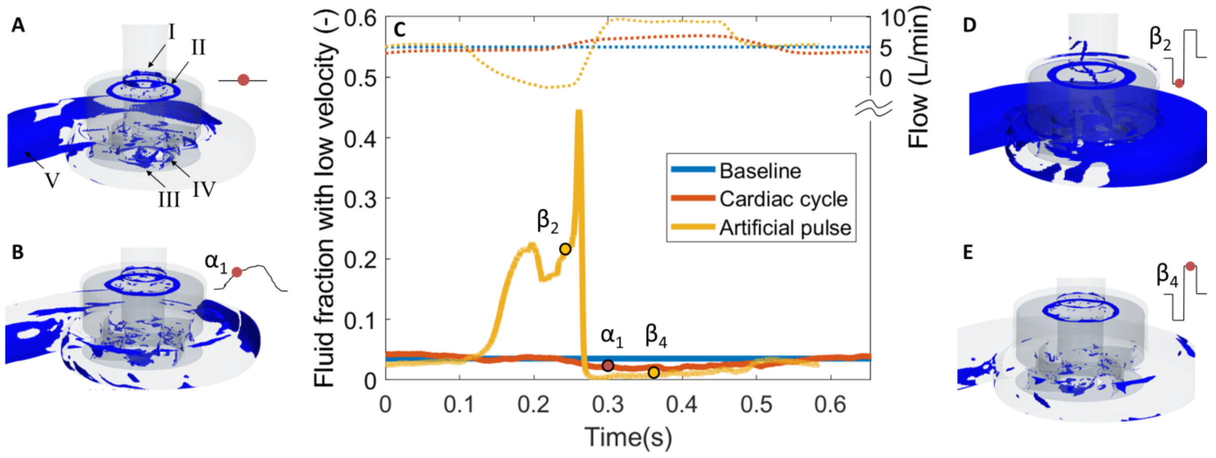

Figure 25: Regions of low velocity: volume with $v_{rel} < 0.2$ m/s and distance from walls > 40 µm. A. 'Baseline' scenario. Blue areas indicate volumes of low velocity. The black arrows indicate areas of stagnation: at the small geometry step at the transition from inlet cannula to volute (I), at the end of the secondary flow path (II), centrally under the rotor (III), at the bottom of the rotor close to the inner edge (IV) and at the volute wall (V). B. Situation during systole in the 'cardiac cycle' scenario. C. Fluid fraction with low velocity plotted over time for the three investigated scenarios. The pump flow rate is plotted with dotted lines to aid interpretation (values on right vertical axis). D. Situation during low speed in the 'artificial pulse' scenario. E. Situation during high speed in the 'artificial pulse' scenario. The selected time points (α_1, β_2 and β_4) refer to those defined in Figure 19. Videos of the regions of low velocity are available as supplementary videos 10 to 12.

4.4.7 Validation

To validate the CFD simulations, we compared the simulated hydraulic performance of the pump to values obtained from in vitro measurements. We assessed the modelled pressure head for a specified flow for 7 operating conditions at 3 different speeds. Simulated pressures were in good agreement with experimental measurements with relative errors ranging between 0.7% and 13.6% (Figure 26).

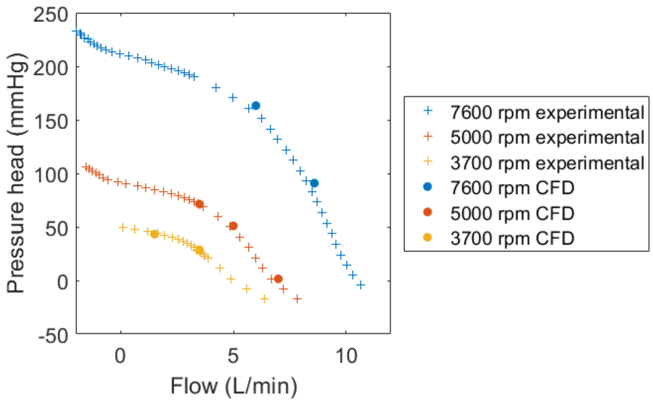

Figure 26: HQ plot displaying measured data and CFD simulation results. H: pressure head (mmHg), Q: flow rate (L/min)

4.5 Discussion

We carried out a high-resolution analysis of the flow inside the HM3 under dynamic conditions, and explored the fluid dynamic effects of its artificial pulse feature, a periodic modulation of the pump rotational speed intended to enhance pump washout as well as to partially restore arterial pulsatility [4]. We compared the effect of the HM3 artificial pulse on the flow field to that induced by remaining cardiac function. Our high-resolution CFD simulations with dynamic boundary conditions allow for unprecedented insight into this VAD's transient flow structures, such as temporal evolution of low velocity and high shear regions. This is of relevance for assessing washout and thrombus formation potential, and determining effective stress and exposure time profiles during physiological off-design point operation. In contrast to the current calculations, previous numerical investigations of axial or centrifugal VADs have employed moving reference frame approaches or large time-steps [175], [235], precluding the continuous analysis of flow structures, or have relied on small time steps but used static boundary conditions [176], [177].

Clinical experience to date suggests that while the HM3 significantly outperforms previous devices in terms of the occurrence of pump thrombosis, patients still suffer from similar rates of gastrointestinal bleeding and detrimental stroke [45]. From a fluid dynamic perspective, this shifts two phenomena into the spotlight: supra-physiological stresses for their potential to damage blood cellular and non-cellular components, as well as stagnation and recirculation regions for their role in thrombus formation and growth.

Elevated stresses affect erythrocytes, platelets, leucocytes and blood proteins, thereby causing hemolysis, platelet activation and impairment of VWF function, respectively. Experimentally determined stress thresholds for hemolysis depend on exposure time, but are generally above 150 Pa [88]. However, recent evidence suggests that even subclinical hemolysis, which may occur below the above mentioned thresholds, might contribute to thrombotic adverse events [61]. Since viscous stresses in the HM3 are generally lower than 150 Pa throughout the investigated conditions, we expect negligible hemolysis, which fits clinical experience [45] and in-vitro experiments [4]. What could occur is subclinical hemolysis, possibly causing a procoagulant state. Shear-mediated platelet activation has been studied experimentally [97], [98], [100]. Applying the power-law model postulated in [97], our calculations indicate a platelet activation state below 1% in the HM3 for the observed viscous stresses and exposure times. However, platelet activation is also sensitive to stress gradients, and high-frequency components (here: 82-94 Hz) have been shown to be major triggers for activation [100]. Analysis of our particle tracks revealed that they often contain frequencies in or above the high-frequency range investigated in [100], suggesting that we may expect higher damage than predicted by the simple power-law model. Shear-mediated damage has further been shown to be a main driver of acquired von Willebrand syndrome, which is associated with the bleeding problems in VAD patients [60]. The exact relationship between shear exposure and bleeding has not yet been found, but experimental studies suggest that stress of the levels seen in the HM3 would, indeed, damage the VWF [108], [236]. Aspects not included in experimental studies so far are damage accumulation and relaxation: Since blood components pass through the high shear environment inside the implanted device thousands of times, damage accumulation and relaxation between exposures could take place. It is known that the stress history should be taken into account to accurately predict potential damage [237]. Consequently, experimental results obtained for long, but single exposures (minutes in [100], hours in [108], [236]) might still be translatable to the clinical setting, but it is not clear how such translation should be done.

There is evidence that turbulent flow situations lead to higher blood trauma than laminar flows with comparable levels of viscous stresses [234]. We accommodated that fact by considering both viscous and total stress levels. Overall, viscous stresses in the HM3 are lower than in the HM2 and the HVAD [7]. Viscous stress levels are also generally lower in the investigated 'cardiac cycle' scenario than in the 'artificial pulse' one. For example, approximately 30% of all particles are exposed to viscous stresses > 50 Pa in the former scenario, and approximately 40% in the latter. Due to the transient flow reversal, exposure times to given viscous shear stress levels are also slightly longer in the 'artificial pulse' scenario (Figure 23, B2 and C2). Yet, the most notable differences are observed in the total stress levels. Total stresses within the cardiac cycle remain similar to viscous stresses, highlighting limited turbulence levels and a small contribution of Reynold stresses. In contrast, in the 'artificial pulse' scenario, total stress levels and the respective exposure times are substantially higher than the viscous ones (Figure 23, C2 and C3). Approximately 37% of the seeded particles are exposed to total stresses > 50 Pa in the 'cardiac cycle' scenario, while in the 'artificial pulse' one 90% of the particles seeded during or shortly before the pulse are affected. Since the artificial pulse covers only 17.5% of the HM3's runtime [4], this translates to approximately 44% of the particles being exposed to total stresses > 50 Pa assuming baseline conditions outside the pulse sequence. The biological effect of Reynold stresses on cells is still a matter of debate. While initially it was believed that Reynold stresses damage blood directly [147], [148], it was later argued that Reynold stresses are inappropriate for direct assessment of mechanical load on cells and that, instead, the resulting viscous stresses should be estimated [88], [149]. In conclusion, the strong increase in total stresses during the artificial pulse should certainly be kept in mind, but further research is needed to understand its potential implications for hemocompatibility.

Independent of the possible consequences, the artificial pulse significantly increased the modelled turbulence in the system. Flow reversal, which may not happen in all patients, reinforces the destabilization observed after initial deceleration. However, the strongest turbulent onset is clearly associated with the rapid speed increase by 4000 rpm following the period of very low flow. This is highlighted by the rise in total stress levels (Figure 22), and might be important to consider during the design of artificial pulse features in general.

Beyond stresses, detrimental flow features include zones of flow detachment, which were observed at the pressure sides and trailing edges of the blades independent of blade position during all (quasi-) static situations assessed in this study. In addition, a four-arm like stagnation zone formed centrally under the rotor. In the 'cardiac cycle' scenario, the detached zones close to the blades remained stable, while the zone under the rotor shifted and resolved during peak flow (supplementary videos 3, 4 and 11). The extent of these changes will depend on individual remaining cardiac function. In the 'artificial pulse' scenario, the low speed caused overall low velocities, but resolved the stagnation and recirculation zones at the blades and below the rotor. These zones of stagnation and recirculation are prone for thrombus growth and generally decrease the hydraulic efficiency of the pump, thus a design minimizing their extent is favorable.

Good passive scalar washout performance was observed for all investigated scenarios. It therefore appears that washout is governed largely by the device geometry and pump flow rate. The time required for 95% washout was comparable to that found in the HVAD, which features a secondary flow path similar to the HM3 [8]. Notably, the implemented scalar only characterizes washout of a fully soluble quantity, neglecting effects like mechanical interaction with the wall or biological interaction between blood components. It is thus conceivable that although the artificial pulse does not increase scalar washout, it may, in reality, help remove blood components from pump surfaces by inducing the observed drastic changes in the flow field and WSS. When interpreted in this way, our results align well with clinical observations of very small numbers of pump thrombi in the HM3 [45].

An important aspect in VADs is pulsation or the lack thereof in rotary blood pumps [26]. Speed modulations as in the HM3 or in the HVAD [35] are a way to induce pulsatility. The speed modulation studied herein resulted in a larger pressure pulse than the corresponding contribution of the residual cardiac function (11 vs 5 mmHg). However, it has to be kept in mind that the artificial pulse is not synchronized with the patient's cardiac cycle. While we have shown here clearly that the artificial pulse has a substantial effect on the flow field, its biological and clinical implications remain to be resolved.

The computational approach employed in this study comes with limitations. Since the geometry is reverse-engineered, small differences to the actual geometry cannot be excluded. Specifically, even small differences in the gap between rotor and housing can influence the obtained stress fields [181]. Here, the rotor position is assumed to be fixed at all operating points. Due to the passive magnetic bearing in the axial direction, the gap might change with changing operating conditions. Furthermore, we assumed rotor actuation to be perfect, implying that the rotor speed always equals its set speed. In our simulations, walls were assumed to be smooth in contrast to the partly sintered actual device. Sintered surfaces may lead to higher stresses than predicted here and could slightly reduce efficiency. Also, even though the turbulence modelling employed in this study follows best practices, it still remains an approximation. Detailed measurements of the turbulent structures in VADs have not been obtained to date. Since the artificial pulse feature is not synchronized with the heartbeat, the flow and pressure dynamics vary considerably depending on the relative temporal position of native and artificial pulse (periodicity > 66s for 91.2 bpm), which makes CFD simulations of scenarios including both the native heart function and the artificial pulse feature too costly. It must also be noted that the flow fields formed during the artificial pulse feature, and especially possible flow reversals, depend on pump speed, pressure head and likely on individual patient physiology.

4.6 Conclusion

Our analysis of the fluid dynamics in the HM3 under dynamic physiologic conditions indicates good washout, which is in line with the clinical observation of very low pump thrombus occurrence rates. Viscous stress levels are slightly higher during the device's artificial pulse, but overall lower than in other clinically used VADs. However, these stress levels are still above what is currently considered benign, which may be reflected in the clinically observed rates of stroke and bleeding, presumably caused, among other factors, by damage to platelets. In our simulations, the artificial pulse did not substantially affect washout, but sudden changes in WSS may aid removal of potential deposits in the pump. At the same time, the artificial pulse increased turbulence substantially. While the biologic effects of turbulence are not known in detail, the resulting elevated total stresses might contribute to hemocompatibility-related problems observed in the clinics.

4.7 Supplementary Material

4.7.1 Grid and time step independence

We conducted grid and time step independence studies and assessed the variation of fields relevant for our study. We investigated the behavior of the fields on a radial cross-sectional plane and three line-probes located in crucial parts of the geometry. The plane and the three locations are illustrated in Supplementary Figure 21. The studies were performed at 5500 rpm and 5 L/min flow. For the grid independence study, a time step of $\Delta t = 6.061 \cdot 10^{-5}$ s (corresponding to 2° of rotation) was used. For the time step independence study, a mesh with 9.9 million cells was used. All other settings of the CFD simulation are described in the Methods section of the main manuscript.

As an additional bulk metric providing an integrative measure of shear stresses, we compared the damage index D as described by Garon and Farinas [115]:

$$D = (\overline{D_I})^{0.785} \tag{14}$$

$$\overline{D_I} = \frac{1}{Q}\int_V \sigma dV \tag{15}$$

$$\sigma = (3.62 \cdot 10^{-7})^{1/0.785} \tau^{2.416/0.785} \tag{16}$$

where Q is the flow rate (L/min) and τ is the shear stress (Pa).

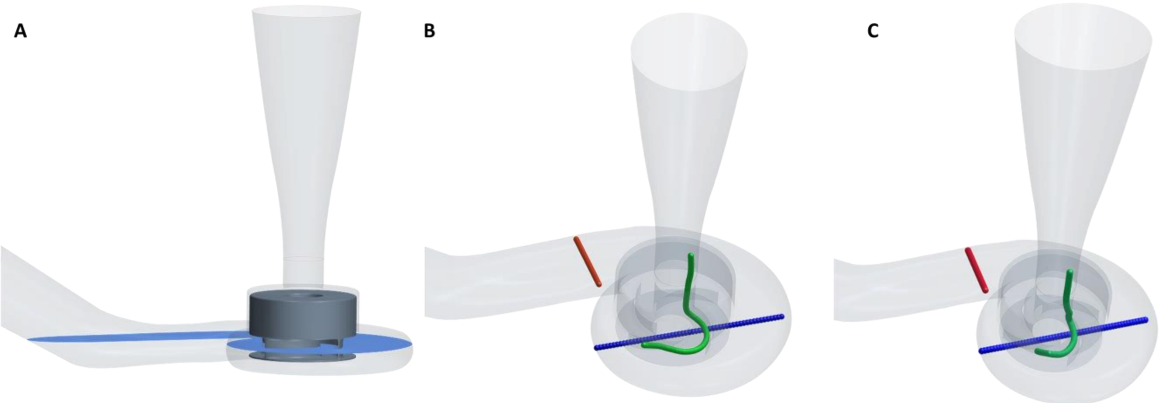

Supplementary Figure 21: A Location of the plane displayed in Supplementary Figure 22 and 3. B: Location of the three line-probes used for testing grid independence: “Cross Outlet” (red) runs across the across the outlet of the volute at half height of the channel. “Streamline” (green) runs along a streamline through the vane. “Bottom Gap” (blue) runs across the gap below the impeller at half height of the total gap. C: Location of the three line-probes used for testing time step independence: “Cross Outlet” (red),. “Streamline” (green) and “Bottom Gap” (blue). The rotor position for the time step independence study is different compared to the grid independence, so a different “Streamline” probe was defined. The “Cross Outlet” and “Bottom Gap” probes are identical.

Supplementary Figure 22 and Supplementary Figure 23 display the distribution of pressure, velocity and vorticity on the plane indicated in Supplementary Figure 21A for the different grid sizes and time steps. The two coarsest grids (6.7 and 7.3 million cells) and coarsest time step ($\Delta t = 3.03 \cdot 10^{-5}$ s, corresponding to 4° of rotation) lead to an undesired smoothing of the vorticity fields.

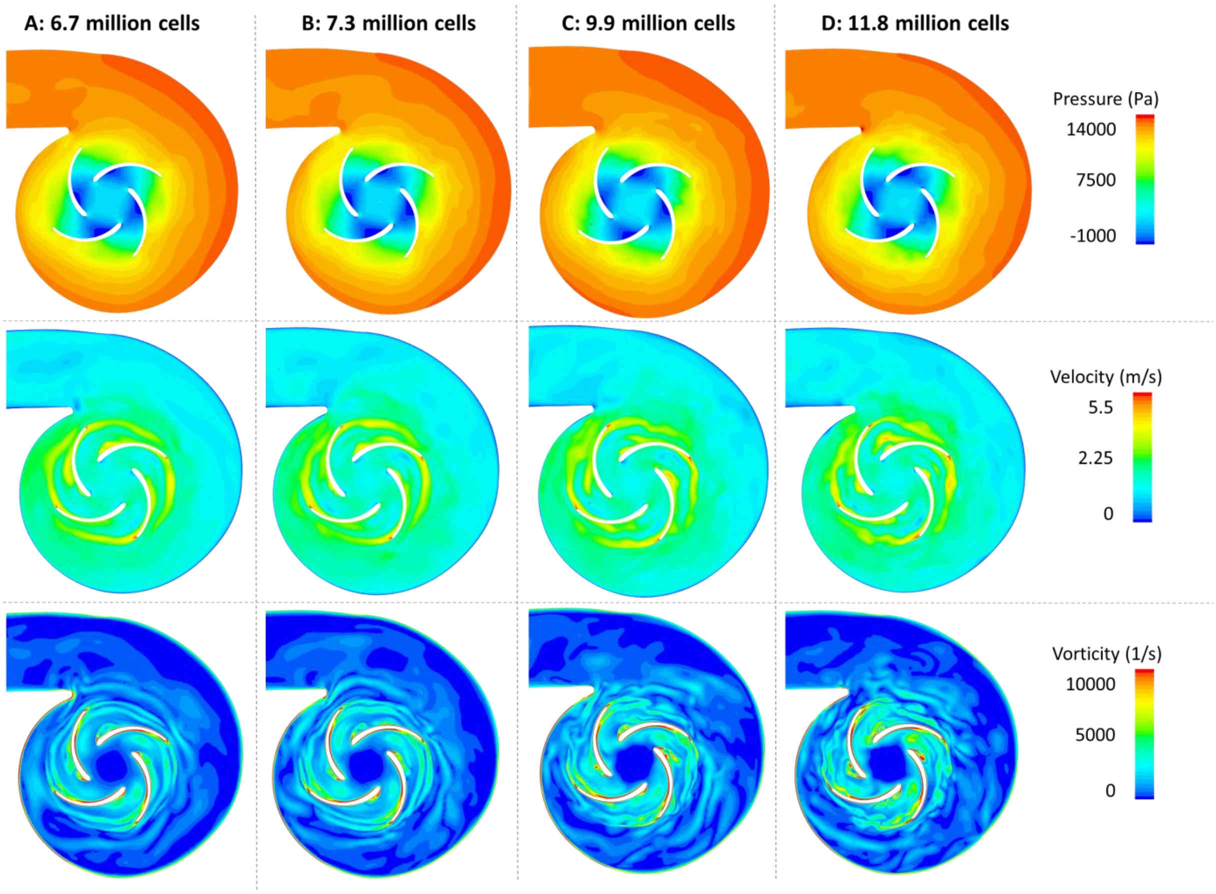

Supplementary Figure 22: A: Pressure (row 1), velocity (row 2) and vorticity (row 3) for the grid containing 6.7 million cells. B: Pressure (row 1), velocity (row 2) and vorticity (row 3) for the grid containing 7.3 million cells. D: Pressure (row 1), velocity (row 2) and vorticity (row 3) for the grid containing 9.9 million cells. D: Pressure (row 1), velocity (row 2) and vorticity (row 3) for the grid containing 11.8 million cells.

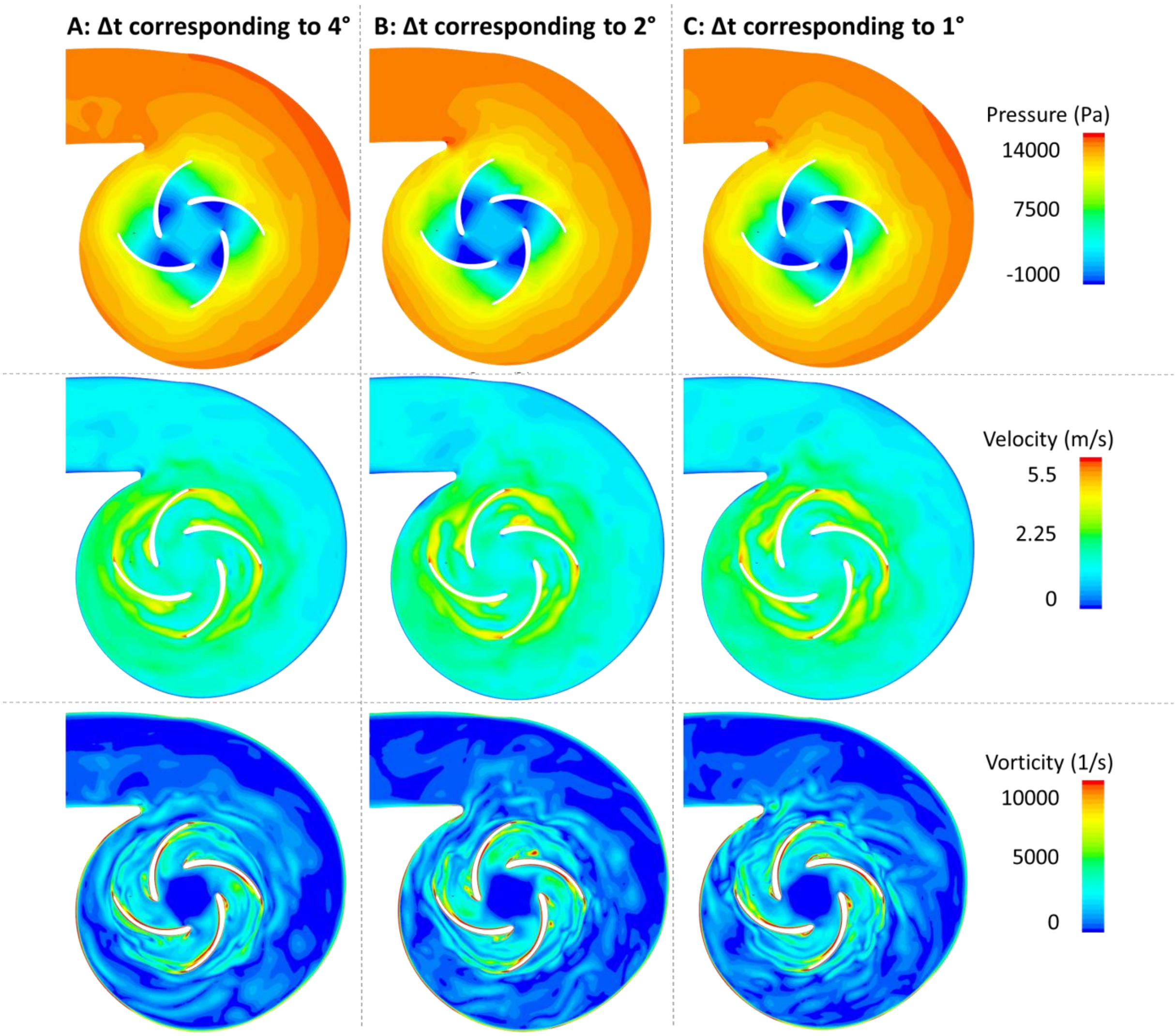

Supplementary Figure 23: A: Pressure (row 1), velocity (row 2) and vorticity (row 3) for the time step corresponding to 4° of rotation. B: Pressure (row 1), velocity (row 2) and vorticity (row 3) for the time step corresponding to 2° of rotation. C: Pressure (row 1), velocity (row 2) and vorticity (row 3) for the time step corresponding to 1° of rotation.

We further investigated the dependence of velocity (Supplementary Figure 24 and Supplementary Figure 25), pressure (Supplementary Figure 26 and Supplementary Figure 27) and shear stress (Supplementary Figure 28 and Supplementary Figure 29) on grid and time step size along our selected line-probes. Additionally, we confirmed the independence of bulk measures relevant for the analyses conducted in the main study on grid and time step size in Supplementary Figure 30 and Supplementary Figure 31.

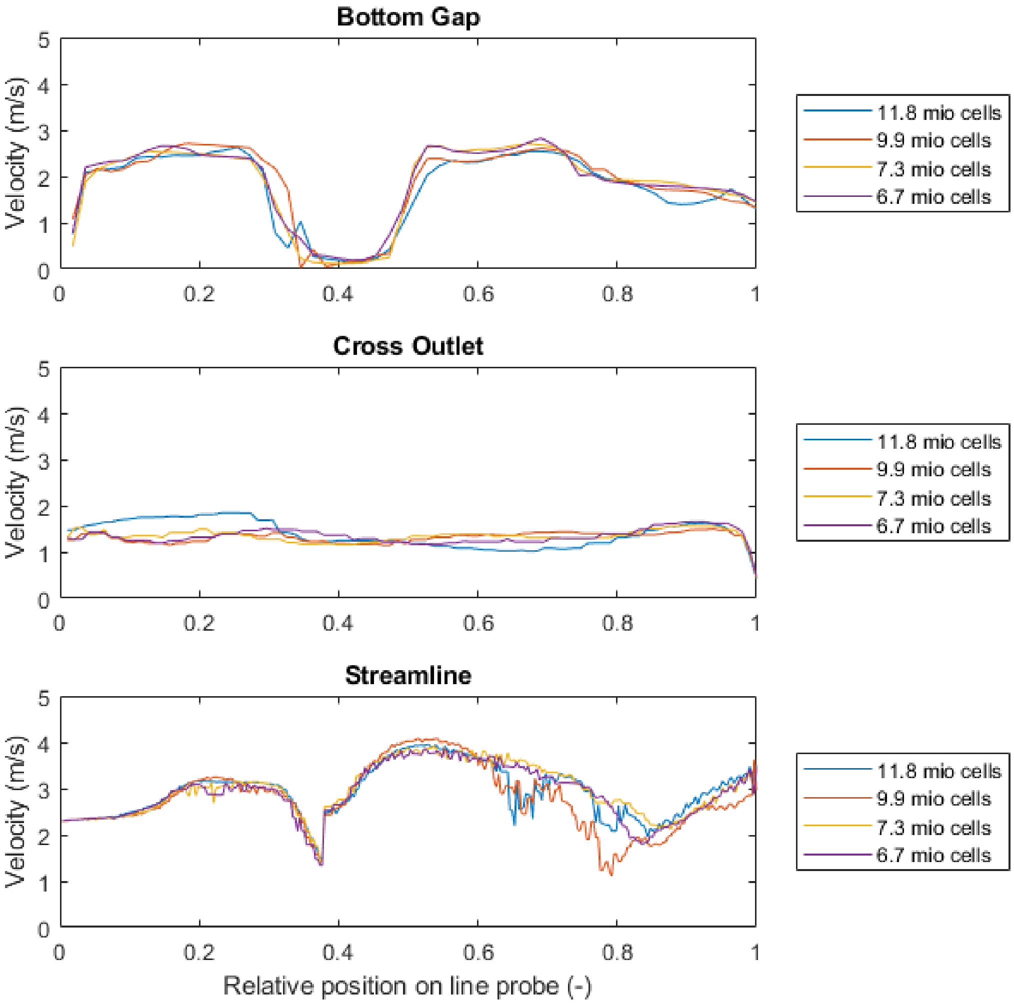

Supplementary Figure 24: Results of the grid independence study with respect to velocity. The three graphs represent the three geometric locations tested. The time step in these simulations was $\Delta t = 6.061 \cdot 10^{-5}$ s . The mesh with 9.9 million cells was chosen for the study.

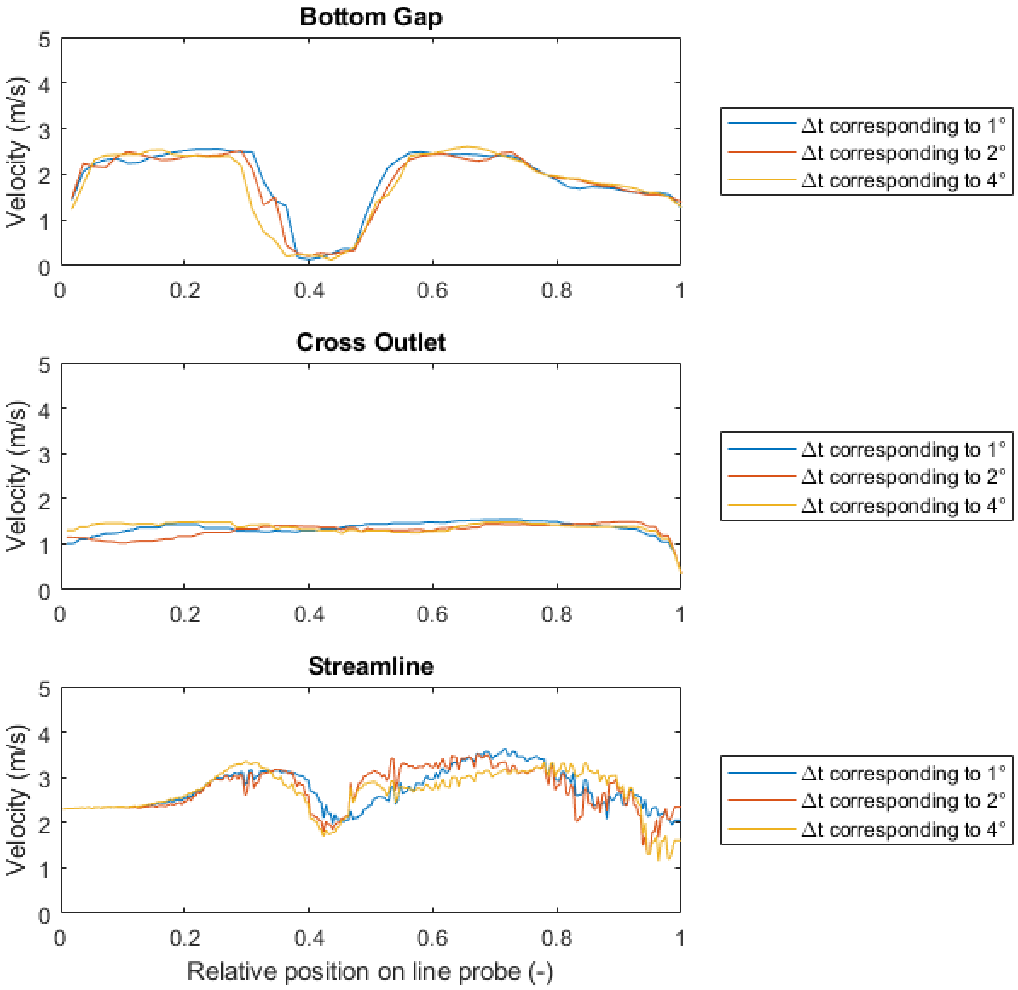

Supplementary Figure 25: Results of the time step independence study with respect to velocity. The three graphs represent the three geometric locations tested. The grid size in these simulations was 9.9 million cells. $\Delta t = 6.061 \cdot 10^{-5}$ s (corresponding to 2° at 5500 rpm) was chosen for the study.

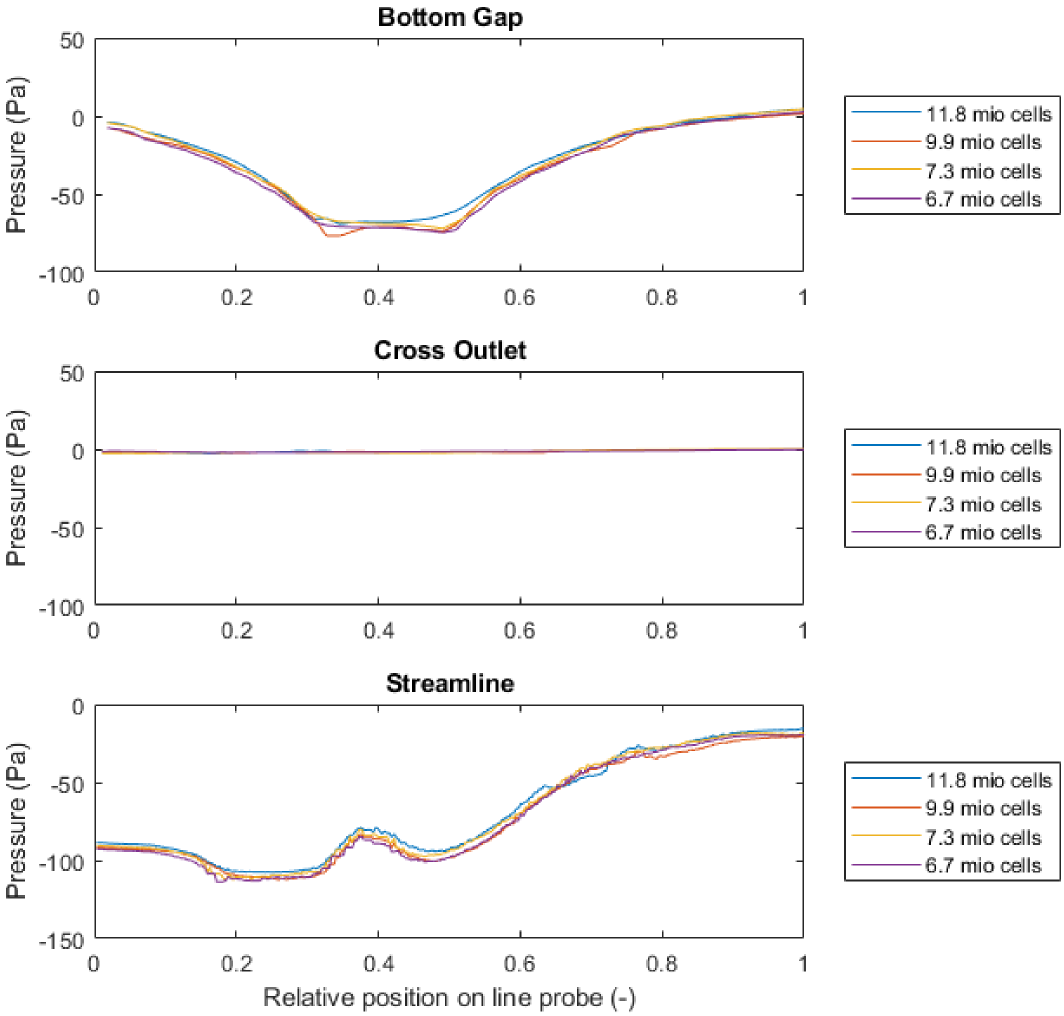

Supplementary Figure 26: Results of the grid independence study with respect to pressure. The three graphs represent the three geometric locations tested. The time step in these simulations was $6.061 \cdot 10^{-5}$ s. The mesh with 9.9 million cells was chosen for the study.

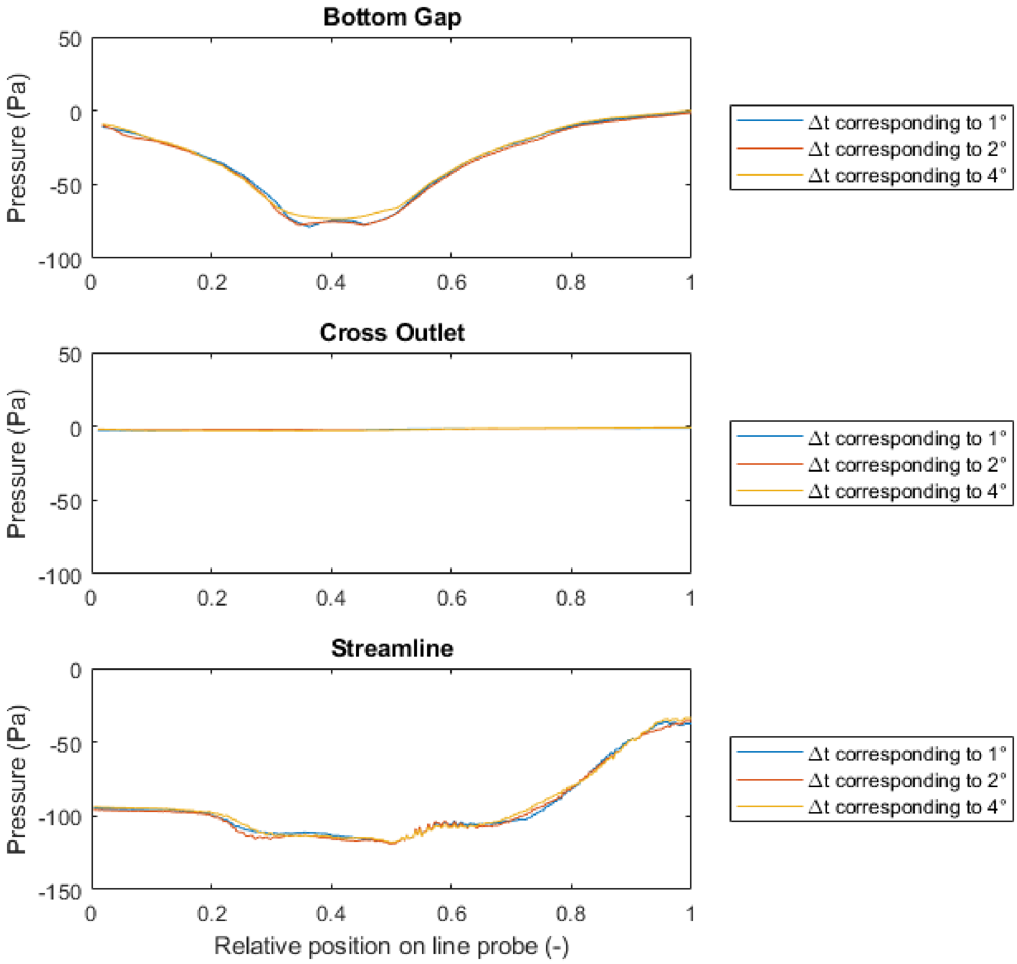

Supplementary Figure 27: Results of the time step independence study with respect to pressure. The three graphs represent the three geometric locations tested. The grid size in these simulations was 9.9 million cells. Δt = $6.061 \cdot 10^{-5}$ s (corresponding to 2° at 5500 rpm) was chosen for the study.

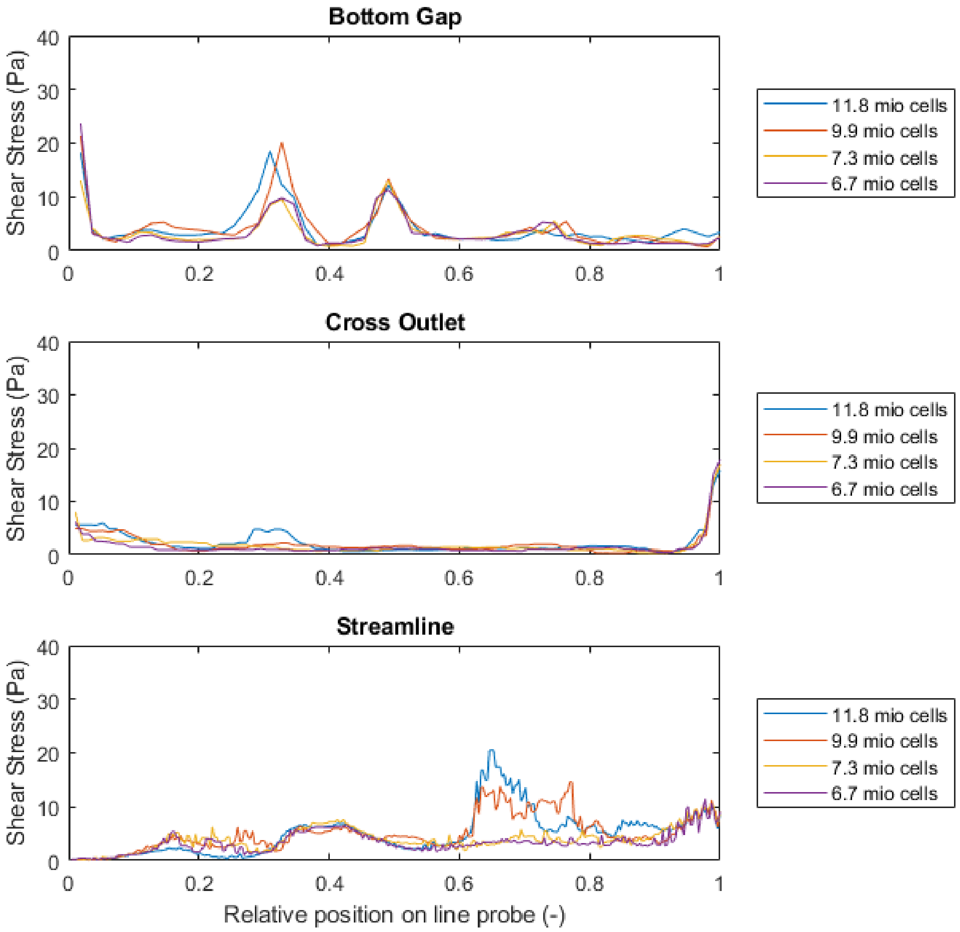

Supplementary Figure 28: Results of the grid independence study with respect to shear stress. The three graphs represent the three geometric locations tested. The time step in these simulations was 6.061 10^{-5} s. The mesh with 9.9 million cells was chosen for the study.

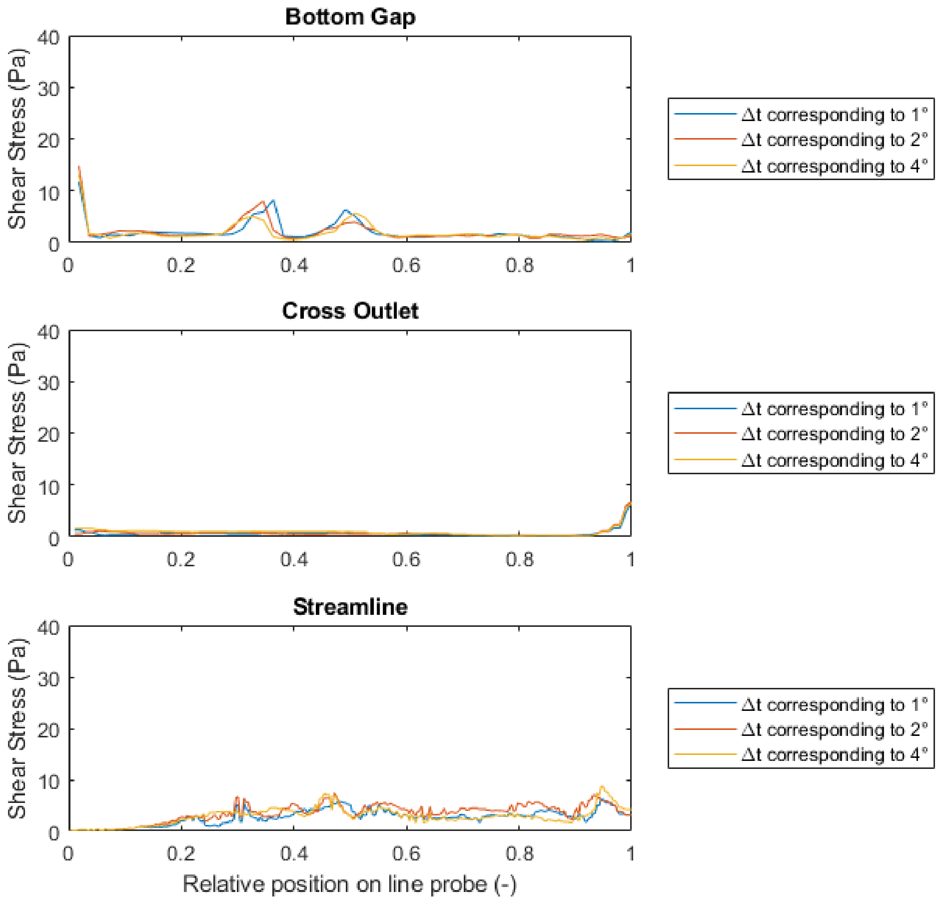

Supplementary Figure 29 Results of the time step independence study with respect to shear stress. The three graphs represent the three geometric locations tested. The grid size in these simulations was 9.9 million cells. Δt = $6.061 \cdot 10^{-5}$ s (corresponding to 2° at 5500 rpm) was chosen for the study.

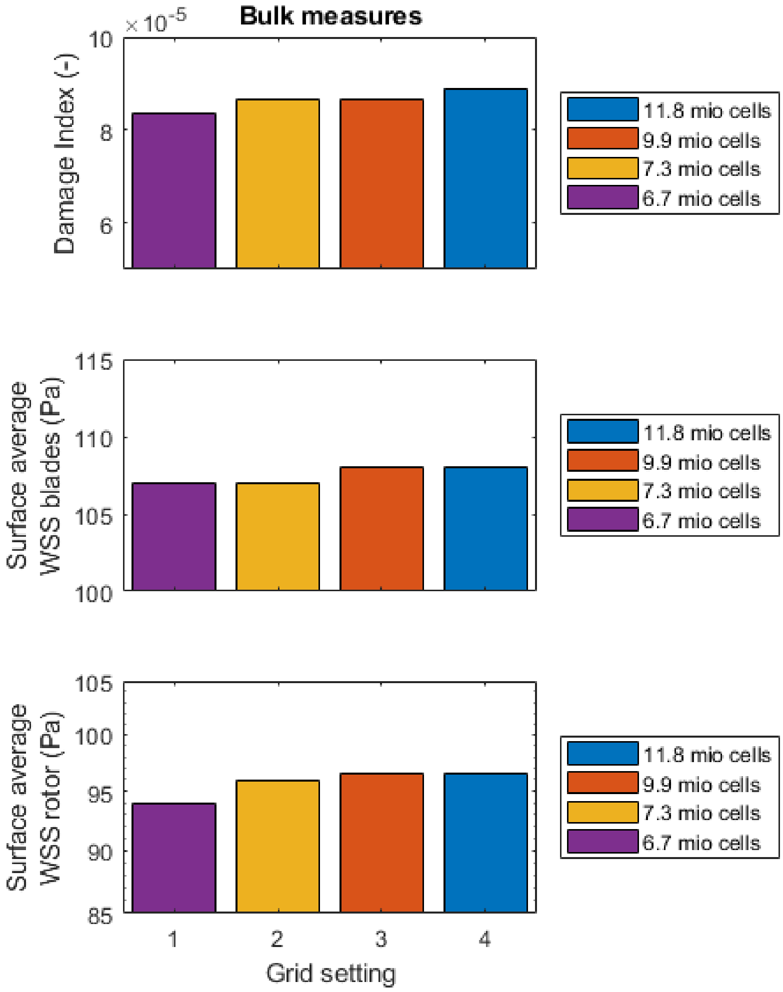

Supplementary Figure 30: Dependence of bulk measures relevant for analyses in the main manuscript on grid size: Damage index, surface average of the wall shear stress (WSS) on the blades and surface average of the WSS on the rotor excluding the blade.

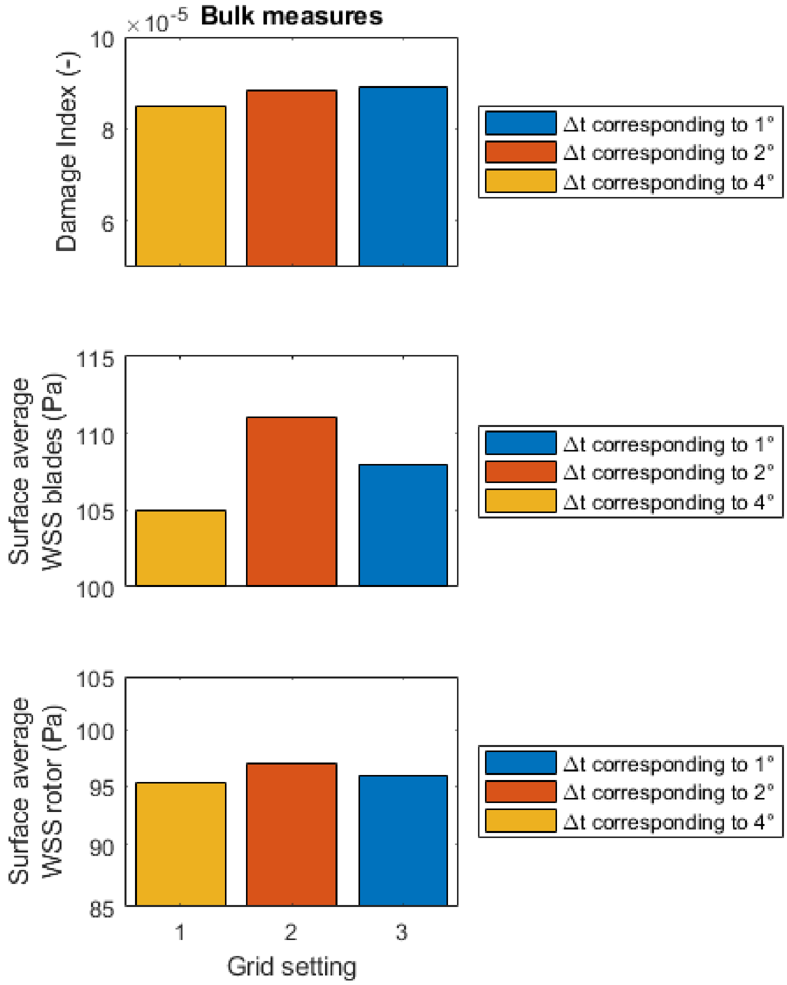

Supplementary Figure 31: Dependence of bulk measures relevant for analyses in the main manuscript on the time step: Damage index, surface average of the wall shear stress (WSS) on the blades and surface average of the WSS on the rotor excluding the blades.

4.7.2 Lagrangian tracks independence study

To test the independence of the exposure time to shear stress above a threshold to the number of tracks, we conducted a track independence study. We injected 371, 780, 1560 and 2340 particles 44 mm downstream of the inlet with a uniform spatial distribution, and compared the resulting exposure times to viscous stresses above 9 Pa and 50 Pa. We repeated this for rotational speeds of 3500, 5500 and 7500 rpm. The time step size was chosen to correspond to 2° steps of rotation, and the mesh contained 9.9 million cells. All other settings were as described in the Method section of the main manuscript. Ultimately, 780 particle tracks were chosen for the study.

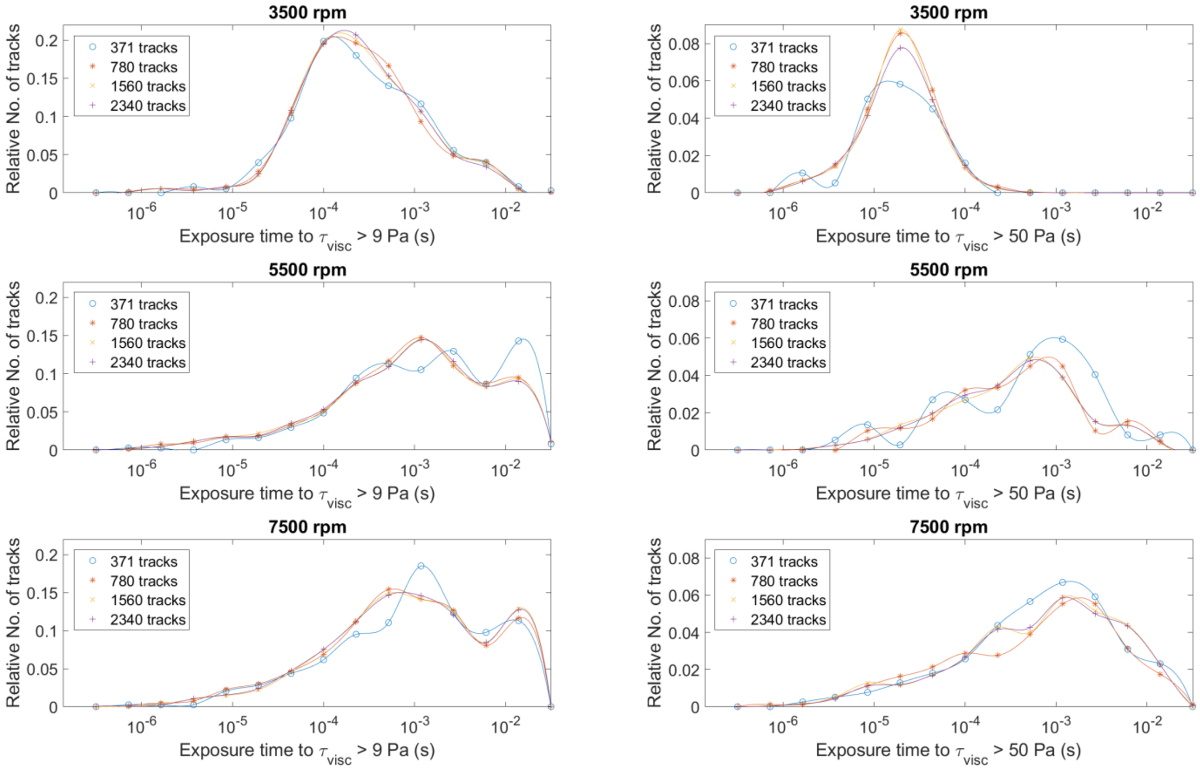

Supplementary Figure 32: Results of the Lagrangian tracks independence study. The histogram are displayed as dots for improved readability. Exposure times to τ_{visc} > 9 Pa and 50 Pa were compared. ‘Relative number of tracks’ refers to the fraction of particle tracks that were exposed to viscous stress above the specified threshold for the indicated time. 780 particle tracks were chosen for the main study.

4.7.3 Exposure time heat maps

In the ‘cardiac cycle’ and ‘artificial pulse’ scenarios, 780 particles each were injected at three time points (as indicated in Figure 19 in the main manuscript). Supplementary Figure 33 and Supplementary Figure 34 display the resulting heat maps for all sets of tracks.

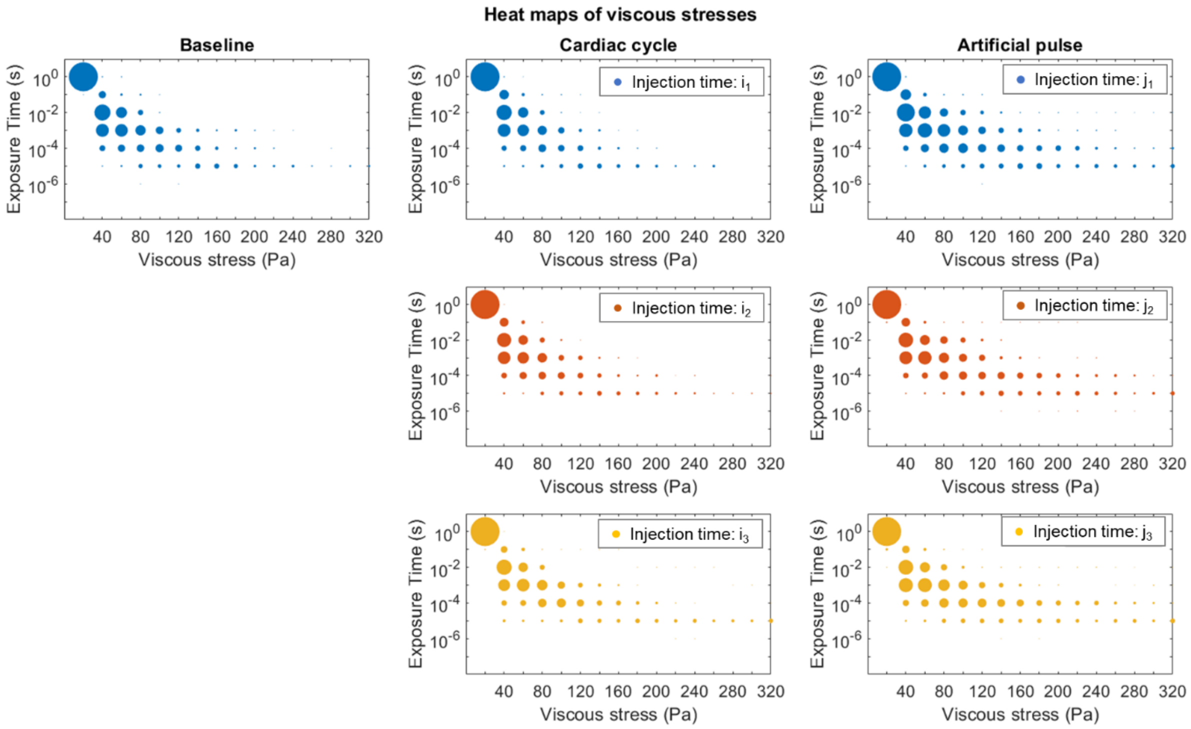

Supplementary Figure 33: Heat maps of exposure times and viscous stresses for ‘baseline’, ‘cardiac cycle’ and ‘artificial pulse’ scenarios for different injection time points. The stresses are binned in steps of 20 Pa (e.g. 100 Pa < τ < 120 Pa), and the exposure time of each particle track to the levels of stress in each stress bin is calculated. The exposure times are then binned in a logarithmic manner (e.g. $10^{-3} < t < 10^{-2}$). The size of the circles represents the number of entries per time and stress bin. For each simulation, all sets of particle tracks are displayed. For the ‘cardiac cycle’ and ‘artificial pulse’ scenario, the injection times i_1,i_2,i_3 and j_1,j_2,j_3, correspond to the time points illustrated in Figure 1 of the main manuscript.

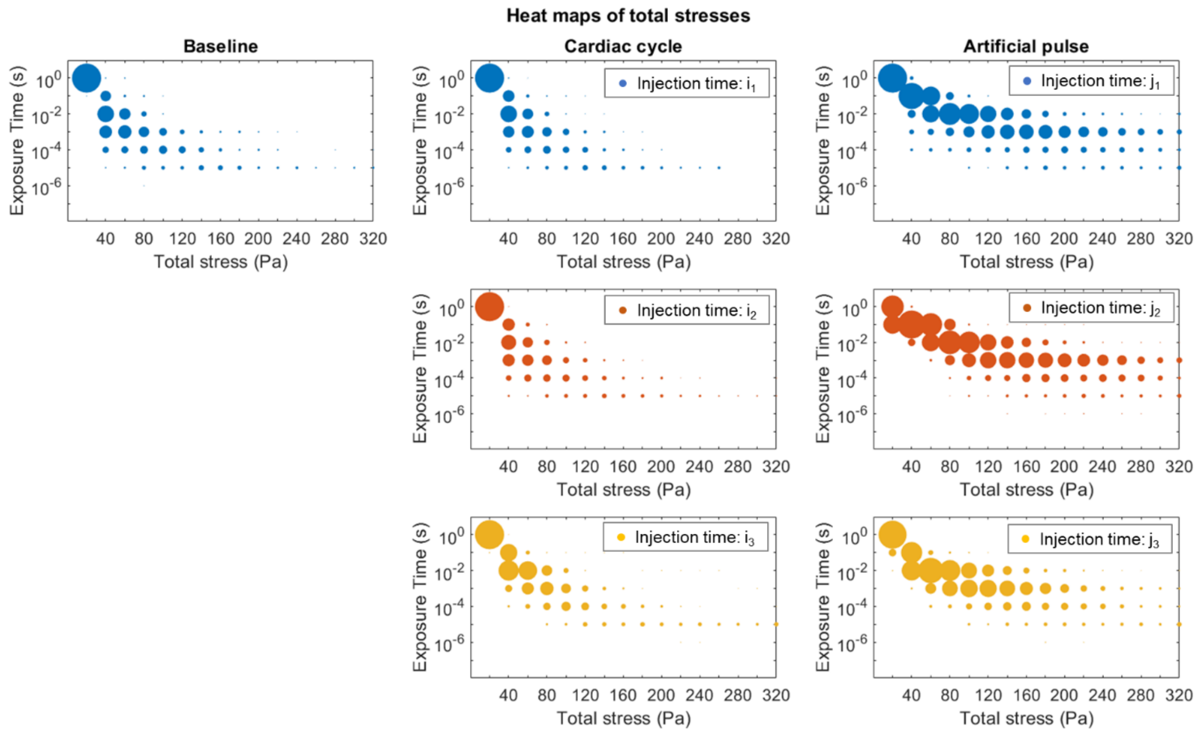

Supplementary Figure 34: Heat maps of exposure times and total stresses for ‘baseline’, ‘cardiac cycle’ and ‘artificial pulse’ scenarios for different injection points. The stresses are binned in steps of 20 Pa (e.g. 100 Pa < τ < 120 Pa), and the exposure time of each particle tracks to the levels of stress in each stress bin is calculated. The exposure times are then binned in a logarithmic manner (e.g. $10^{-3} < t < 10^{-2}$). The size of the circles represents the number of entries per time and stress bin. For each simulation, all sets of particle tracks are displayed. For the ‘cardiac cycle’ and ‘artificial pulse’ scenario, the injection times i_1,i_2,i_3 and j_1,j_2,j_3, correspond to the time points illustrated in Figure 1 of the main manuscript.

4.7.4 Lagrangian track data

Supplementary Table 3 summarizes the fraction of particles exposed to stresses above thresholds of 9, 50 and 150 Pa.

	Viscous stresses			**Total stresses**		
	Baseline (%)	Cardiac cycle (%)	Artificial pulse (%)	Baseline (%)	Cardiac cycle (%)	Artificial pulse (%)
$\boldsymbol{\tau_{thres} = 9\ Pa}$	83	84, 82, 77	93,85,86	99	98, 98, 99	99,100, 100
$\boldsymbol{\tau_{thres} = 50\ Pa}$	34	29, 29, 31	46, 35, 39	36	30, 30, 51	80, 99, 90
$\boldsymbol{\tau_{thres} = 150\ Pa}$	5	4, 4,6	12, 9, 10	5	4, 4, 6	40, 46, 32

Supplementary Table 3: Fraction of particles (%) exposed to $\boldsymbol{\tau > \tau_{thres}}$. The three numbers per cell indicate the set of particles injected at time points i_1, i_2,i_3 and j_1,j_2, j_3, as defined in Figure 1 in the main manuscript, for the ‘cardiac cycle’ and ‘artificial pulse’ scenarios, respectively.

5 Discussion

Ventricular assist devices improve quality of life and survival of end-stage heart failure patients, but rates of adverse events are still high [6], [31]. Many of the clinical complications are linked to the hemocompatibility of the device, such as bleeding, strokes, pump thromboses and hemolysis. Understanding their relation to the flow conditions in the device and optimizing the geometry for minimal expected damage are crucial for the development of the next generation VADs and were the topic of this PhD thesis.

Experimental studies are necessary to shed light on the consequences of elevated shear stresses, as they occur in VADs, on biological cells. In particular, characterization of the dynamic stress patterns and load histories experienced by blood cells or proteins flowing through the VAD is required for an accurate characterization of blood damage [128]. Only if such knowledge exists, can an efficient and successful device design optimization process be established. While many experimental studies have focused on bulk measures of damage [97], [112], [217], the experimental setups used therein (typically Couette viscometers) are limited in their capability to reproduce the high-frequency dynamics observed in cardiovascular implants. A viable alternative are micro-channels made of polydimethysiloxane (PDMS) as this material is biocompatible and manufacturing processes allow for small channels with high geometric freedom [238], [239]. Such micro-channels can be designed in a way that they reproduce shear loading patterns observed in VADs [80], [240], which only then makes it feasible to accurately characterize the effect of VAD hemodynamics on blood cells. However, irrespective of the detailed design of the channels, such experiments include handling steps for the preparation of cells, their placement in the device and subsequent analytical steps, all of which may induce spurious stresses on the cells and introduce confounding effects in the experimental endpoints. Secondary effects, such as high pressures required to drive flow through the micro-channels, may similarly influence the measured results. Exact understanding of the influence of possible confounding factors on the experimental endpoints is crucial for a correct interpretation of the results, which equally applies for interfering factors in analyses conducted in clinical laboratories [187]. Researchers have investigated the effect of transport [195], RBC processing in the transfusion setting [194] and common methodological mistakes in RBC handling [241], but, to date, little literature is available addressing the specific impact of laboratory handling steps on RBCs. We aimed to fill this knowledge gap with our study on the influence of standard laboratory procedures on RBC damage [180], which comprises chapter 2 of this thesis. Here, we showed that centrifuging, vortexing, pipetting and high pressures lead to increased levels of free hemoglobin and that this effect depends significantly on the level of stress. We also found evidence for changes in RBC population and membrane properties after exposure to elevated pressures and centrifuging. These results highlight the importance of a careful quantification of the effects of sample handling and other secondary effects induced by the experimental setup on the measurements of interest. It is advised to include such a priori quantification into the experimental protocols to remove potential confounders.

Our study forms the basis for further research on the cell damage due to highly dynamic shear stress patterns. In particular, we intended to pave the way for studies utilizing geometries small enough to conduct single-cell experiments. We believe that this is a necessary next step to understand the effects of shear stress patterns similar to those occurring in cardiovascular implants, since only such experiments would allow for a true assessment of the forces acting on the cell surface. In micro-channels in the 50 to 100 µm range as in [80], [240], multiple cells fit the channel's cross-section (RBCs are around 5-8 µm in diameter, platelets around 2 µm [242]). Since in such channels the velocity gradients are not constant over the entire cross-section, fluid stresses differ accordingly. Consequently, depending on the exact path of a cell in the channel, its mechanical loading considerably varies. Thus, the exact trace of each cell would need to be known to derive the shear stresses acting on its membrane and to be linked to potential alterations in membrane properties or damage. Instead of tracking each cell's position, designing the channel in a way that the cell's stress history is known a priori seems a promising option. The latter could be achieved by utilizing a channel small enough to only fit one cell per cross-section. A major challenge arising from micro-channels with such small cross-sections is the large pressure gradient that is required to drive the flow, which by itself could unduly influence the cells. Hence, we believe that specifically our quantification of the damage induced by static pressure will facilitate the development of such experimental setups. Our results indicated that temporal pressure gradients, more than the absolute pressure values, could be the predominant factor for RBC lysis, which should be considered during the experimental design.

Our study was limited by the sole use of hematologically healthy blood. From a clinical perspective, the assessment of hereditary or acquired disorders of RBC membrane alterations, such as spherocytosis or sickle cell disease, would elucidate the relevance of our results in the setting of a clinical hematology laboratory. Also in the setting of heart failure patients, shape, distribution or oxidative state of blood cells can deviate from healthy individuals [243]–[245], which might alter their response to mechanical stresses.

The biophysical interaction between cardiovascular implants and blood is critically influenced by fluid dynamics. Here, we established a computational framework to simulate the flow fields and related stresses inside VADs under physiological operating conditions. We explored our framework in two main directions: Firstly, we took advantage of its versatility during the design phase and assessed the influence of systematic variations of given geometrical parameters, and secondly we investigated the flow structures inside a commercial VAD in light of experiences gained in clinical practice.

During the development of a VAD, numerous decisions on the fluid dynamic design need to be taken. Some are governed by technical constraints originating e.g. from the actuation or levitation requirements, but many aspects in the impeller or volute geometry can potentially be optimized towards highest hydraulic efficiency and maximal hemocompatibility. Naturally, however, these two aspects can be contradictory in their preferred design choices. With our study published in *Annals of Biomedical Engineering* [181] and presented in chapter 3 of this thesis, we aimed at providing a systematic investigation of the influence of selected design aspects on hydraulic performance and indicators of hemocompatibility to facilitate these decisions. We specifically assessed the influence of the number of blades, clearance gap sizes and shroud design and found an association of reduced zones of flow stasis with lower numbers of blades, a semi-open impeller and larger clearance gaps. Potentially damaging shear stress conditions were reduced for smaller gaps and fewer blades. Overall, this study facilitated an insight into the systematic effect of selected design features on the flow field. Additionally, we assessed the statistical correlation between various metrics that have been proposed in literature to assess hemocompatibility and hydraulic performance. Here, we found that the Lagrangian hemolysis index, which is commonly applied to estimate blood damage, had a negative correlation with the hydraulic efficiency. It however was not correlated to an Eulerian threshold-based metric suggested to predict hemolysis as well. Similarly, two metrics previously suggested to estimate platelet activation were not correlated in our data. These findings highlight the need for improved models to predict blood damage based on computational models.

The main limitation of this study was the evaluation of a single operating point. We tested all design variations against a constant pressure head at the same constant rotational speed, which resulted in different flow rates for the different designs. In the clinical application, the pump speed would be adjusted to achieve the same hydraulic output. While VADs effectively operate at a constant pump speed, this selected speed also varies from patient to patient, while we restricted our analyses to one specific rotation rate. Furthermore, in a clinical setting, the blood pump faces varying pressures and flows at the interface to the cardiovascular system. We addressed this limitation in our second CFD-based study. Also, even though the metrics for blood damage employed in our study are widely used in cardiovascular modelling, they considerably simplify the underlying biological mechanisms and remain explorative.

While the aforementioned study was conducted on a conceptual blood pump design derived from industrial guidelines [15], we applied our computational framework to a current clinical VAD, the HeartMate 3, in the study presented in chapter 4 of this thesis. Here, our intention was to link the clinical experience available for the HM3 [45], [221] with its internal flow structures. One of the HM3's key features is the so called 'artificial pulse', which has been hypothesized to improve pump washout [4] and thereby inhibit pump thrombus formation. However, this hypothesis had not been tested so far. The dynamic flow fields in the HM3 were unknown, as was the isolated impact of the artificial pulse. We filled this knowledge gap with our study investigating three operational scenarios: a 'baseline' scenario with constant boundary conditions and constant pump speed, a 'cardiac cycle' scenario mimicking the remaining cardiac function interacting with a HM3 operating at constant speed with the artificial pulse virtually switched off, and an 'artificial pulse' scenario considering no native cardiac function, but the speed modulation.

We found good scalar washout performance for all investigated scenarios, suggesting that this behavior is largely governed by the geometry and the flow rate. The observed washout times were similar to those measured for the HVAD, but longer than those measured for the HMII [8]. This is not surprising, since the HMII is an axial pump in contrast to the HVAD and the HM3, that both are centrifugal pumps. Centrifugal pumps by design feature a designated secondary flow path, which increases the time required to completely washout the pump, whereas axial pumps do not have such a secondary flow path. However, it has to be kept in mind that scalar washout alone is not sufficient to predict potential thrombus formation in a VAD. It only characterizes washout of a fully soluble quantity, neglecting effects like interference with the wall, mass, or possible interaction between biological cells. In fact, despite the favorable washout performance [8], the HeartMate II is known to be specifically prone to pump thrombus formation. This has been observed clinically [43], [45] and studied in computational models [246], but remains to be fully understood [44]. In contrast, the HeartMate 3 so far seems to perform relatively well in that respect, reducing significantly the occurrence of pump thromboses [45]. In our study, we found that its artificial pulse lead to drastic changes in the flow field, thereby causing variations in WSS. These can be hypothesized to foster removal of potential deposits in the pump, before larger thrombi can grow. Interpreted that way, our insights gained on the flow fields fit well with the clinical observations.

Beyond the washout performance, we also assessed the shear stresses on the blood inside the HM3 during its operation. Overall, we found that viscous stress levels were lower than in other clinical pumps for all our investigated scenarios [7]. Still, there were multiple regions with stresses high enough to lead to shear-induced blood cell damage, as outlined in chapter 1.3. Viscous stresses were also generally lower during the ‘cardiac cycle’ than during the ‘artificial pulse’ scenario. While viscous stresses were classically considered to be damaging to cells [85], there is evidence that turbulent flow structures might cause additional, possibly higher, blood damage [234]. In fact, the most notable differences between the ‘cardiac cycle’ and the ‘artificial pulse’ scenario were observed in the total stresses, which include (turbulent) Reynolds stresses in addition to viscous stresses. The artificial pulse and especially the rapid speed increase after a period of very low flow substantially increased the turbulence in the system. While the exact biological consequences of turbulent stresses on cells are still a matter of debate [88], [147]–[149], this effect might be important to consider during the design of artificial pulse features.

A current aspect of discussion in VADs is pulsatility or the lack thereof in rotary blood pumps [26], [72]. The absence or reduction of the native pulsatility was associated with negative effects on the vasculature [20], reduced washout of the left ventricular outflow tract [247], aortic valve lesion [70] and other complications. Artificial pulses as in the HM3 could be a way to overcome these limitations, but their effect on the overall hemocompatibility of the pump and resulting clinical impact remain yet to be shown. Similar to the HM3, the HVAD features such an automated speed modulation. Evidence for a positive clinical effect of this modulation has indeed been observed: Zimpfer et al. showed that while overall survival and GI bleeding rates were not affected, patients with the ‘Lavare cycle’ turned on had significantly fewer rates of strokes, sepsis and right heart failure than those with the ‘Lavare cycle’ turned off [35]. Unfortunately, similar data is not available for the HM3, since turning the artificial pulse off is not a therapeutical option. The speed changes of the HVAD’s ‘Lavare cycle’ are less extreme than those in the HM3’s artificial pulse, and it is yet an open question how this translates into clinical performance.

The computational studies presented in chapters 3 and 4 of this thesis share a common limitation, which is the still weak quantitative link between actual hemocompatibility of a device in clinical practice and the fluid stresses used for its prediction. Even though there exist a variety of numerical blood damage models, as outlined in chapter 1.3.3, they have been shown to only poorly reflect experimental data [126]. We highlighted that shortcoming also in our study on the influence of design variations (chapter 3), where we additionally assessed the statistical correlation between damage metrics suggested to indicate the same type of blood damage. Even though threshold-based and Lagrangian-tracking-based hemolysis predictions are applied to predict the same type of damage [143], [163], [172], [248], we found that they did not statistically correlate. While the lack of adequate models for absolute blood trauma performance prohibits absolute predictions of blood damage, there is no doubt that flow-induced cell damage does occur in blood pumps: blood cellular components have been shown to react to elevated shear stress levels depending on the cells' exposure time as well as on the presence of zones of recirculation and stagnation. Consequently, in our studies we used these models not as absolute predictors of blood damage, but as integrative metrics of hemodynamic features. To overcome this limitation, development of models that are capable of accurately predicting red blood cell damage, thrombus formation and the occurrence of bleeding, are clearly a major next step in improving today's VADs [26].

On the numerical side, an assumption that studies investigating the flow in entire VADs using CFD have in common, is the modelling of blood as a single-phase fluid [4], [16], [17], [142], [166], [167], [235]. In fact, however, blood is clearly a multi-phase fluid, containing various cell types and proteins dissolved in plasma. This aspect is often neglected since the global flow patterns are well captured also with the single-phase simplification and computational cost is a limiting factor. Nevertheless, particularly in view of damage models based on cellular deformation or surface strains, models capable of describing the behavior of single cells and inter-cellular interactions might be key in understanding and predicting blood damage. Several such models have been published [132], [249]–[251], and are capable of modelling physiological hematocrits [135]. To date, however, the modelled geometries for such multiscale models are usually cylindrical pipes or micro-channels. The next challenge will be to apply these models to geometries and flows as complicated as in VADS.

Another challenge from the modelling perspective is the coupling between the fluid flow and position of the rotor. The bearing type determines some general aspects of this coupling: In Pivot bearings, the gap between impeller and housing is principally constant besides potential wear [10], which makes the modelling in CFD comparably easy. An example of a VAD with a pivot bearing is the HeartMate II. In hydrodynamic bearings, a fluid film between rotor and stator generates hydrodynamic forces that levitate the impeller. The HVAD features such a hydrodynamic bearing in combination with passive magnets [33]. The actual gap size here depends on the relation between magnetic forces, pressure distributions and flow momentum [12] and changes e.g. during the 'Lavare cycle'. Likewise, fully magnetically levitated bearings, as they are for example used in the HM3, allow for a contactless design. The impeller position in the HM3 is actively controlled in radial direction but only passively stabilized in axial direction. Similar to hydrodynamic bearings, the resulting gap size depends on the interaction between the different forces acting on the impeller and may thus vary during physiological operation. To date, CFD studies in the VAD field do not account for these dynamic variations in gap size. Coupling the structural components of the VAD to the fluid is principally possible, but computationally expensive and is usually applied if the interaction between fluid and structure is a fundamental characteristic of the mechanism under investigation. In the field of cardiovascular implants, so far this was considered relevant mostly for mechanical heart valves [99], [212], [252] and pulsatile mechanical circulatory assist devices [158]. However, it might be necessary to devise possible solutions to account for variations in rotor position also in rotary blood pumps, since the gap size directly influences the stress fields and thus potential shear-mediated damage, as we have also highlighted in chapter 3. This will be especially relevant for studies spanning different operating points, as in our investigation of the HM3 dynamics.

6 Conclusion and Outlook

While enhancing hemocompatibility is a key aspect in improving today's VADs, other important areas of research include physiological control, sensor technology, transcutaneous energy transmission and enhanced biocompatibility of the pump's material. The *Zurich Heart* project [179], which this thesis project is part of, is a collaborative research endeavor and intends to improve the state of the art in these and other areas.

In the here presented PhD thesis, we provide insights into flow-related aspects of hemocompatibility, both from an experimental and a computational perspective. In the first part of this thesis, we assessed the effect of mechanical stresses on red blood cells during handling and processing steps. The next step will be the utilization of this knowledge for the design of experimental protocols that quantify mechanical RBC damage in highly dynamic shear stress environments, as they occur in VADs. While such experiments would be conducted on cells from healthy donors to start with, a meaningful next step could be the investigation of blood and its cellular components from heart failure patients. Clearly, the impact of the employed handling and processing steps on these cells would have to be carefully monitored. These findings might not only be relevant for the VAD field, but for the development of cardiovascular implants in general. Besides red blood cells, also other blood components, such as platelets or the von Willebrand factor, are critically influenced by the supra-physiological shear stresses in these devices. Advances in the characterization of their shear- or otherwise device-related damage will surely be important to improve the state-of-the-art of cardiovascular implants.

In the second and third part of this thesis, we developed a high-resolution computational fluid dynamics framework to model the flow inside blood pumps. We applied this framework to a conceptual pump design and assessed the systematic effect of selected design variations, providing general principles to guide designers in their choices about VAD geometrical features. Next to this more academic and general approach, we investigated the fluid dynamics in the latest clinical VAD, the HeartMate 3. While the former study had the advantage that it was not constrained by specific choices for e.g. bearing or actuation design, the latter study could make use of the availability of clinical data. Combined, the findings reported in these studies shall aid the design of geometrical, but also operational features for a next generation VAD with improved hemocompatibility. Clearly, an important next step is the development of more accurate models to predict hemocompatibility based on the flow structures and stresses in VADs. Besides that, coupling of the fluid with the rotor dynamics might be devised for simulations spanning multiple operating points. Finally, modelling the actual deformations of blood cellular components in the complex environment of a blood pump will certainly be a challenging, but important task to further understand the biophysical interaction between blood and device.

7 References

[1] E. Braunwald, “The war against heart failure: the Lancet lecture,” *Lancet*, vol. 385, no. 9970, pp. 812–824, 2015.

[2] S. A. Hunt and E. Rose, “The REMATCH trial: Long-term use of a left ventricular assist device for end-stage heart failure,” *J. Card. Fail.*, vol. 8, no. 2, pp. 59–60, 2002.

[3] J. K. Kirklin *et al.*, “Sixth INTERMACS annual report: A 10,000-patient database,” *J. Hear. Lung Transplant.*, vol. 33, no. 6, pp. 555–564, 2014.

[4] K. Bourque *et al.*, “Design Rationale and Pre-Clinical Evaluation of the HeartMate 3 Left Ventricular Assist System for Hemocompatibility.,” *ASAIO J.*, vol. 62, no. 4, pp. 375–383, 2016.

[5] L. W. Stevenson *et al.*, “INTERMACS Profiles of Advanced Heart Failure: The Current Picture,” *J. Hear. Lung Transplant.*, vol. 28, no. 6, pp. 535–541, 2009.

[6] J. K. Kirklin *et al.*, “Eighth annual INTERMACS report: Special focus on framing the impact of adverse events,” *J. Hear. Lung Transplant.*, vol. 36, no. 10, pp. 1080–1086, 2017.

[7] B. Thamsen *et al.*, “Numerical Analysis of Blood Damage Potential of the HeartMate II and HeartWare HVAD Rotary Blood Pumps,” *Artif. Organs*, vol. 39, no. 8, pp. 651–659, 2015.

[8] A. Molteni, Z. P. H. Masri, K. W. Q. Low, H. N. Yousef, J. Sienz, and K. H. Fraser, “Experimental measurement and numerical modelling of dye washout for investigation of blood residence time in ventricular assist devices,” *Int. J. Artif. Organs*, 2018.

[9] N. Moazami *et al.*, “Axial and centrifugal continuous-flow rotary pumps: A translation from pump mechanics to clinical practice,” *J. Hear. Lung Transplant.*, vol. 32, no. 1, pp. 1–11, 2013.

[10] K. S. Sundareswaran, S. H. Reichenbach, K. B. Masterson, K. C. Butler, and D. J. Farrar, “Low bearing wear in explanted HeartMate II left ventricular assist devices after chronic clinical support.,” *ASAIO J.*, vol. 59, no. 1, pp. 41–45, 2013.

[11] D. Timms, “A review of clinical ventricular assist devices,” *Med. Eng. Phys.*, vol. 33, no. 9, pp. 1041–1047, 2011.

[12] B. Thamsen *et al.*, “Investigation of the Axial Gap Clearance in a Hydrodynamic-Passive Magnetically Levitated Rotary Blood Pump Using X-Ray Radiography,” *Artif. Organs*, vol. 00, no. 3, pp. 0–5, 2018.

[13] A. Arvand, N. Hahn, M. Hormes, M. Akdis, M. Martin, and H. Reul, “Comparison of hydraulic and hemolytic properties of different impeller designs of an implantable rotary blood pump by computational fluid dynamics,” *Artif. Organs*, vol. 28, no. 10, pp. 892–898, 2004.

[14] G. Paul, A. Rezaienia, and E. Avital, “Machinability and optimisation of shrouded centrifugal impellers for implantable blood pumps,” vol. 11, no. c, pp. 1–7, 2017.

[15] J. F. Gülich, *Centrifugal Pumps*. Berlin Heidelberg: Springer, 2010.

[16] T. Korakianitis, M. A. Rezaienia, G. M. Paul, A. Rahideh, M. T. Rothman, and S.

Mozafari, “Optimization of Centrifugal Pump Characteristic Dimensions for Mechanical Circulatory Support Devices.,” *ASAIO J.*, p. 1, 2016.

[17] S. Mozafari, M. A. Rezaienia, G. M. Paul, M. T. Rothman, P. Wen, and T. Korakianitis, “The Effect of Geometry on the Efficiency and Hemolysis of Centrifugal Implantable Blood Pumps,” *ASAIO J.*, p. 1, 2016.

[18] C. H. H. Chan, A. Hilton, G. Foster, K. M. Hawkins, N. Badiei, and C. A. Thornton, “The evaluation of leukocytes in response to the in vitro testing of ventricular assist devices,” *Artif. Organs*, vol. 37, no. 9, pp. 793–801, 2013.

[19] J. Suarez, C. B. Patel, G. M. Felker, R. Becker, A. F. Hernandez, and J. G. Rogers, “Mechanisms of Bleeding and Approach to Patients With Axial-Flow Left Ventricular Assist Devices,” *Circ. Hear. Fail.*, vol. 4, no. 6, pp. 779–784, 2011.

[20] K. Muthiah *et al.*, “Increased incidence of angiodysplasia of the gastrointestinal tract and bleeding in patients with continuous flow left ventricular assist devices (LVADs),” *Int. J. Artif. Organs*, vol. 36, no. 7, pp. 449–454, 2013.

[21] D. Saeed, B. Maxhera, N. Sadat, G. Petrov, A. Albert, and A. Lichtenberg, “Gastrointestinal Bleeding in Patients with HeartWare Ventricular Assist Device,” *ASAIO J.*, vol. 64, no. 1, pp. 126–128, 2018.

[22] U. Geisen *et al.*, “Non-surgical bleeding in patients with ventricular assist devices could be explained by acquired von Willebrand disease,” *Eur. J. Cardio-Thoracic Surg. Off. J. Eur. Assoc. Cardio-Thoracic Surg.*, vol. 33, no. 4, pp. 679–684, 2008.

[23] M. Bedi, R. Kormos, S. Winowich, D. M. McNamara, M. A. Mathier, and S. Murali, “Ventricular Arrhythmias During Left Ventricular Assist Device Support,” *Am. J. Cardiol.*, vol. 99, no. 8, pp. 1151–1153, 2007.

[24] N. Yuan *et al.*, “The spectrum of complications following left ventricular assist device placement,” *J. Card. Surg.*, vol. 27, no. 410, pp. 630–638, 2012.

[25] J. G. Rogers, “Balancing Bleeding and Clotting,” pp. 1–3.

[26] M. R. Mehra, “The burden of haemocompatibility with left ventricular assist systems: a complex weave,” *Eur. Heart J.*, no. December, pp. 1–5, 2017.

[27] P. Shah, U. S. Tantry, K. P. Bliden, and P. A. Gurbel, “Bleeding and Thrombosis Associated with Ventricular Assist Device Therapy: A State of the Art Review,” *J. Hear. Lung Transplant.*, 2017.

[28] M. R. Mehra *et al.*, “A Fully Magnetically Levitated Circulatory Pump for Advanced Heart Failure,” *N. Engl. J. Med.*, vol. 376, no. 5, pp. 440–450, 2017.

[29] S. E. Sandner *et al.*, “Renal Function After Implantation of Continuous Versus Pulsatile Flow Left Ventricular Assist Devices,” *J. Hear. Lung Transplant.*, vol. 27, no. 5, pp. 469–473, 2008.

[30] A. M. Patel, G. A. Adeseun, I. Ahmed, N. Mitter, J. E. Rame, and M. R. Rudnick, “Renal Failure in Patients with Left Ventricular Assist Devices,” *Clin. J. Am. Soc. Nephrol.*, vol. 8, no. 3, pp. 484–496, 2013.

[31] E. V Potapov, A. Stepanenko, T. Krabatsch, and R. Hetzer, “Managing long-term

complications of left ventricular assist device therapy.," *Curr. Opin. Cardiol.*, vol. 26, no. 3, pp. 237–244, 2011.

[32] B. P. Griffith *et al.*, "HeartMate II left ventricular assist system: From concept to first clinical use," *Ann Thorac Surg*, vol. 71, no. 00, pp. S116–S120, 2001.

[33] J. a Larose, D. Tamez, M. Ashenuga, and C. Reyes, "Design concepts and principle of operation of the HeartWare ventricular assist system.," *ASAIO J.*, vol. 56, no. March, pp. 285–289, 2010.

[34] M. Strueber *et al.*, "Results of the post-market Registry to Evaluate the HeartWare Left Ventricular Assist System (ReVOLVE)," *J. Hear. Lung Transplant.*, vol. 33, no. 5, pp. 486–491, 2014.

[35] D. Zimpfer *et al.*, "Evaluation of the HeartWare ventricular assist device Lavare cycle in a particle image velocimetry model and in clinical practice," *Eur. J. Cardio-thoracic Surg.*, vol. 50, no. 5, pp. 839–848, 2016.

[36] K. Bourque *et al.*, "HeartMate III: Pump Design for a Centrifugal LVAD with a Magnetically Levitated Rotor," *ASAIO J.*, vol. 47, no. 4, pp. 401–405, 2001.

[37] C. Y. Schüle *et al.*, "Experimental and Numerical Investigation of an Axial Rotary Blood Pump," *Artif. Organs*, vol. 40, no. 11, pp. E192–E202, 2016.

[38] S. Sathishkumar, R. Kodavatiganti, S. Plummer, and K. High, "Perioperative management of a patient with an axial-flow rotary ventricular assist device for laparoscopic ileo-colectomy," *J. Anaesthesiol. Clin. Pharmacol.*, vol. 28, no. 1, p. 101, 2012.

[39] B. Lima, M. Mack, and G. V. Gonzalez-Stawinski, "Ventricular assist devices: The future is now," *Trends Cardiovasc. Med.*, vol. 25, no. 4, pp. 360–369, 2015.

[40] D. Zimpfer *et al.*, "Multicentre clinical trial experience with the HeartMate 3 left ventricular assist device: 30-day outcomes," *Eur. J. Cardio-thoracic Surg.*, vol. 50, no. 3, pp. 548–554, 2016.

[41] S. D. Lalonde *et al.*, "Clinical Differences between continuous flow ventricular assist devices: A comparison between HeartMate II and HeartWare HVAD," *J. Card. Surg.*, vol. 28, no. 5, pp. 604–610, 2013.

[42] J. M. Stulak *et al.*, "Adverse events in contemporary continuous-flow left ventricular assist devices: A multi-institutional comparison shows significant differences," *J. Thorac. Cardiovasc. Surg.*, vol. 151, no. 1, pp. 177–189, 2016.

[43] R. C. Starling *et al.*, "Unexpected abrupt increase in left ventricular assist device thrombosis.," *N. Engl. J. Med.*, vol. 370, no. 1, pp. 33–40, 2014.

[44] N. Jeffries, M. A. Miller, W. C. Taddei-peters, C. Burke, J. T. Baldwin, and J. B. Young, "What is the truth behind pump thrombosis in the HeartMate II device ? A National Heart , Lung , and Blood Institute perspective based on data from the Interagency Registry for Mechanically Assisted Circulatory Support," *J. Hear. Lung Transplant.*, vol. 34, no. 12, pp. 1505–1510, 2015.

[45] M. R. Mehra *et al.*, "Two-Year Outcomes with a Magnetically Levitated Cardiac Pump in Heart Failure," *N. Engl. J. Med.*, vol. 378, pp. 1386–1395, 2018.

[46] C. N. Bagot and R. Arya, “Virchow and his triad: A question of attribution,” *Br. J. Haematol.*, vol. 143, no. 2, pp. 180–190, 2008.

[47] C. Olin, “Titanium in Cardiac and Cardiovascular Applications,” in *Titanium in Medicine: Material Science, Surface Science, Engineering, Biological Responses and Medical Applications*, Berlin, Heidelberg: Springer Berlin Heidelberg, 2001, pp. 889–907.

[48] L. I. Mikhalovska *et al.*, “Fibrinogen adsorption and platelet adhesion to metal and carbon coatings,” *Thromb. Haemost.*, vol. 92, no. 5, pp. 1032–1039, 2004.

[49] A. de Biasi, K. Manning, and A. Salemi, “Science for surgeons: Understanding pump thrombogenesis in continuous-flow left ventricular assist devices,” *J. Thorac. Cardiovasc. Surg.*, vol. 149, no. 3, pp. 667–673, 2015.

[50] V. G. Nielsen *et al.*, “Mechanical circulatory device thrombosis: A new paradigm linking hypercoagulation and hypofibrinolysis,” *ASAIO Journal*, vol. 54, no. 4. pp. 351–358, 2008.

[51] T. Krabatsch, T. Drews, E. Potapov, Y. Weng, M. Pasic, and R. Hetzer, “Different surgical strategies for implantation of continuous-flow VADs—Experience from Deutsches Herzzentrum Berlin,” *Annals of Cardiothoracic Surgery*, vol. 3, no. 5. pp. 472–474, Sep-2014.

[52] M. Laumen *et al.*, “Flow analysis of ventricular assist device inflow and outflow cannula positioning using a naturally shaped ventricle and aortic branch.,” *Artif. Organs*, vol. 34, no. 10, pp. 798–806, 2010.

[53] M. Neidlin *et al.*, “Hemodynamic analysis of outflow grafting positions of a ventricular assist device using closed-loop multiscale CFD simulations: Preliminary results,” *J. Biomech.*, vol. 49, no. 13, pp. 2718–2725, 2016.

[54] M. Granegger *et al.*, “Interaction of a Transapical Miniaturized Ventricular Assist Device With the Left Ventricle: Hemodynamic Evaluation and Visualization in an Isolated Heart Setup,” *Artif. Organs*, vol. 40, no. 12, pp. 1113–1120, 2016.

[55] S. Liao *et al.*, “Numerical prediction of thrombus risk in an anatomically dilated left ventricle: the effect of inflow cannula designs,” *Biomed. Eng. Online*, vol. 15, no. S2, pp. 587–604, 2016.

[56] N. K. Mondal *et al.*, “Systemic Inflammatory Response Syndrome in End-Stage Heart Failure Patients Following Continuous-Flow Left Ventricular Assist Device Implantation: Differences in Plasma Redox Status and Leukocyte Activation,” *Artif. Organs*, vol. 40, no. 5, pp. 434–443, 2016.

[57] C. N. Pierce and D. F. Larson, “Inflammatory cytokine inhibition of erythropoiesis in patients implanted with a mechanical circulatory assist device,” *Perfusion*, vol. 20, no. 2, pp. 83–90, 2005.

[58] D. Feldman *et al.*, “The 2013 International Society for Heart and Lung Transplantation Guidelines for mechanical circulatory support: Executive summary,” *J. Hear. Lung Transplant.*, vol. 32, pp. 157–187, 2013.

[59] S. Susen, A. Rauch, E. Van Belle, A. Vincentelli, and P. J. Lenting, “Circulatory

support devices: Fundamental aspects and clinical management of bleeding and thrombosis," *J. Thromb. Haemost.*, vol. 13, no. 10, pp. 1757–1767, 2015.

[60] A. Nascimbene, S. Neelamegham, O. H. Frazier, J. L. Moake, and J. Dong, "Acquired von Willebrand syndrome associated with left ventricular assist device," vol. 127, no. 25, pp. 3133–3142, 2016.

[61] C. R. Bartoli *et al.*, "Clinical and In Vitro Evidence That Subclinical Hemolysis Contributes to LVAD Thrombosis," *Ann. Thorac. Surg.*, 2017.

[62] P. Jilma-Stohlawetz *et al.*, "Acquired von Willebrand factor deficiency caused by LVAD is ADAMTS-13 and platelet dependent," *Thromb. Res.*, vol. 137, pp. 196–201, 2016.

[63] B. Steinlechner *et al.*, "Platelet Dysfunction in Outpatients With Left Ventricular Assist Devices," *Ann. Thorac. Surg.*, vol. 87, no. 1, pp. 131–137, 2009.

[64] C. Heilmann *et al.*, "Acquired von Willebrand syndrome in patients with ventricular assist device or total artificial heart," *Thromb. Haemost.*, vol. 103, no. 5, pp. 962–967, 2010.

[65] C. Menichini and X. Y. Xu, "Mathematical modeling of thrombus formation in idealized models of aortic dissection: initial findings and potential applications," *J. Math. Biol.*, vol. 73, no. 5, pp. 1205–1226, 2016.

[66] R. L. Replogle, H. J. Meiselman, and E. W. Merrill, "SPECIAL ARTICLE: Clinical Implications of Blood Rheology Studies," *Circulation*, vol. 36, no. 1, pp. 148–160, 1967.

[67] J. F. Antaki, O. Ghattas, G. W. Burgreen, and B. He, "Computational flow optimization of rotary blood pump components.," *Artif. Organs*, vol. 19, no. 7, pp. 608–15, 1995.

[68] D. Bluestein, "Research approaches for studying flow-induced thromboembolic complications in blood recirculating devices," *Expert Rev. Med. Devices*, vol. 1, no. 1, pp. 65–80, 2004.

[69] N. Moazami *et al.*, "Does pulsatility matter in the era of continuous-flow blood pumps?," *J. Hear. Lung Transplant.*, vol. 34, no. 8, pp. 999–1004, 2015.

[70] J. Cowger, F. D. Pagani, J. W. Haft, M. A. Romano, K. D. Aaronson, and T. J. Kolias, "The development of aortic insufficiency in left ventricular assist device-supported patients," *Circ. Hear. Fail.*, vol. 3, no. 6, pp. 668–674, 2010.

[71] T. Krabatsch *et al.*, "Is bridge to recovery more likely with pulsatile left ventricular assist devices than with nonpulsatile-flow systems?," *Ann. Thorac. Surg.*, vol. 91, no. 5, pp. 1335–1340, 2011.

[72] K. G. Soucy, S. C. Koenig, G. A. Giridharan, M. A. Sobieski, and M. S. Slaughter, "Rotary pumps and diminished pulsatility: Do we need a pulse?," *ASAIO J.*, vol. 59, no. 4, pp. 355–366, 2013.

[73] L. Jia, C. Bonaventura, J. Bonaventura, and J. S. Stamler, "S-nitrosohaemoglobin: a dynamic activity of blood involved in vascular control," *Nature*, vol. 380, p. 221, Mar. 1996.

[74] J. R. Pawloski, D. T. Hess, and J. S. Stamler, “Export by red blood cells of nitric oxide bioactivity,” *Nature*, vol. 409, p. 622, Feb. 2001.

[75] J. Wan, W. D. Ristenpart, and H. A. Stone, “Dynamics of shear-induced ATP release from red blood cells,” *Proc. Natl. Acad. Sci.*, vol. 105, no. 43, p. 16432 LP – 16437, Oct. 2008.

[76] J. D. Litster, “Stability of lipid bilayers and red blood cell membranes,” *Phys. Lett. A*, vol. 53, no. 3, pp. 193–194, 1975.

[77] N. Mohandas, M. R. Clark, M. S. Jacobs, and S. B. Shohet, “Analysis of factors regulating erythrocyte deformability.,” *J. Clin. Invest.*, vol. 66, no. 3, pp. 563–73, 1980.

[78] R. P. Rand, “Mechanical Properties of the Red Cell Membrane: II. Viscoelastic Breakdown of the Membrane,” *Biophys. J.*, vol. 4, no. 4, pp. 303–316, Jul. 1964.

[79] E. A. Evans and L. La Celle, “Intrinsic Material Properties of the Erythrocyte Membrane Indicated by Mechanical Analysis of Deformation,” *Blood*, vol. 45, no. 1, 1975.

[80] R. Zhao, J. F. Antaki, T. Naik, T. N. Bachman, M. V Kameneva, and Z. J. Wu, “Microscopic investigation of erythrocyte deformation dynamics,” *Biorheology*, vol. 43, no. 6, pp. 747–765, 2006.

[81] R. P. Rother, L. Bell, P. Hillmen, and M. T. Gladwin, “The Clinical Sequelae of Intravascular Hemolysis and Extracelullar Plasma Hemoglobin,” *JAMA*, vol. 293, no. 13, pp. 1653–1662, 2015.

[82] V. Tchantchaleishvili, F. Sagebin, R. E. Ross, W. Hallinan, K. Q. Schwarz, and H. T. Massey, “Evaluation and treatment of pump thrombosis and hemolysis,” *Ann Cardiothorac Surg*, vol. 3, no. 5, pp. 490–495, 2014.

[83] N. Sutton, M. C. Tracey, I. D. Johnston, R. S. Greenaway, and M. W. Rampling, “TECHNICAL REPORT A Novel Instrument for Studying the Flow Behaviour of Erythrocytes through Microchannels Simulating Human Blood Capillaries,” *Microvasc. Res.*, vol. 53, no. 3, pp. 272–281, 1997.

[84] N. Korin, A. Bransky, and U. Dinnar, “Theoretical model and experimental study of red blood cell (RBC) deformation in microchannels,” *J. Biomech.*, vol. 40, pp. 2088–2095, 2007.

[85] L. Leverett, J. Hellums, C. Alfrey, and E. C. Lynch, “Red blood cell damage by shear stress,” *Biophys. J.*, vol. 12, pp. 257–273, 1972.

[86] R. Paul, J. Apel, S. Klaus, F. Schügner, P. Schwindke, and H. Reul, “Shear stress related blood damage in laminar Couette flow,” *Artif. Organs*, vol. 27, no. 6, pp. 517–529, 2003.

[87] J. Ding, S. Niu, Z. Chen, T. Zhang, B. P. Griffith, and Z. J. Wu, “Shear-Induced Hemolysis: Species Differences,” *Artif. Organs*, vol. 39, no. 9, pp. 795–802, 2015.

[88] N. J. Quinlan and P. N. Dooley, “Models of flow-induced loading on blood cells in laminar and turbulent flow, with application to cardiovascular device flow,” *Ann. Biomed. Eng.*, vol. 35, no. 8, pp. 1347–1356, 2007.

[89] S. E. Olia, T. M. Maul, J. F. Antaki, and M. V. Kameneva, “Mechanical blood trauma in assisted circulation: sublethal RBC damage preceding hemolysis,” *Int. J. Artif. Organs*, vol. 00, no. 00, pp. 0–0, 2016.

[90] N. F. Zeng and W. D. Ristenpart, “Mechanical response of red blood cells entering a constriction,” *Biomicrofluidics*, vol. 8, no. 6, pp. 1–17, 2014.

[91] X. Bao, C. Lu, and J. A. Frangos, “Temporal gradient in shear but not steady shear stress induces PDGF-A and MCP-1 expression in endothelial cells: role of NO, NFκB, and egr-1,” *Arterioscler. Thromb. Vasc. Biol.*, vol. 19, no. 4, pp. 996–1003, 1999.

[92] J. a LaMack and M. H. Friedman, “Individual and combined effects of shear stress magnitude and spatial gradient on endothelial cell gene expression,” *Am. J. Physiol. Heart Circ. Physiol.*, vol. 293, no. 5, pp. H2853–H2859, 2007.

[93] S. S. Kay, A. M. Bilek, K. C. Dee, and D. P. Gaver, “Pressure gradient, not exposure duration, determines the extent of epithelial cell damage in a model of pulmonary airway reopening.,” *J. Appl. Physiol.*, vol. 97, no. March 2004, pp. 269–276, 2004.

[94] T. Nagel, N. Resnick, C. F. Dewey Jr., and M. A. Gimbrone Jr., “Vascular endothelial cells respond to spatial gradients in fluid shear stress by enhanced activation of transcription factors,” *Arterioscler. Thromb. Vasc. Biol.*, vol. 19, no. 8, pp. 1825–1834, 1999.

[95] M. H. Kroll, J. D. Hellums, L. V McIntire, A. I. Schafer, and J. L. Moake, “Platelets and Shear Stress,” *Blood*, vol. 80, no. 5, pp. 1105–1115, 1992.

[96] J. D. Hellums, “1993 Whitaker lecture: Biorheology in thrombosis research,” *Ann. Biomed. Eng.*, vol. 22, no. 5, pp. 445–455, 1994.

[97] J. Ding *et al.*, “Quantification of Shear-Induced Platelet Activation: High Shear Stresses for Short Exposure Time,” *Artif. Organs*, vol. 39, no. 7, pp. 576–583, 2015.

[98] J. Sheriff, J. S. Soares, M. Xenos, J. Jesty, and D. Bluestein, “Evaluation of shear-induced platelet activation models under constant and dynamic shear stress loading conditions relevant to devices,” *Ann. Biomed. Eng.*, vol. 41, no. 6, pp. 1279–1296, 2013.

[99] M. Nobili *et al.*, “Numerical simulation of the dynamics of a bileaflet prosthetic heart valve using a fluid–structure interaction approach,” *J. Biomech.*, vol. 41, no. 11, pp. 2539–2550, 2008.

[100] F. Consolo *et al.*, “High Frequency Components of Hemodynamic Shear Stress Profiles are a Major Determinant of Shear-Mediated Platelet Activation in Therapeutic Blood Recirculating Devices,” *Sci. Rep.*, vol. 7, no. 1, 2017.

[101] Z. Chen, N. K. Mondal, J. Ding, J. Gao, B. P. Griffith, and Z. J. Wu, “Shear-induced platelet receptor shedding by non-physiological high shear stress with short exposure time: glycoprotein Ibα and glycoprotein VI,” *Thromb. Res.*, vol. 135, no. 4, pp. 692–698, 2015.

[102] T. A. Springer, “von Willebrand factor, Jedi knight of the bloodstream,” *Blood*, vol. 113, no. 21, pp. 5049–5058, 2016.

[103] S. Crow *et al.*, “Acquired von Willebrand syndrome in continuous-flow ventricular

assist device recipients," *Ann. Thorac. Surg.*, vol. 90, no. 4, pp. 1263–1269, 2010.

[104] C. Heilmann *et al.*, "Acquired Von Willebrand syndrome is an early-onset problem in ventricular assist device patients," *Eur. J. Cardio-thoracic Surg.*, vol. 40, no. 6, pp. 1328–1333, 2011.

[105] M. Goda *et al.*, "Time course of acquired von Willebrand disease associated with two types of continuous-flow left ventricular assist devices: HeartMate II and CircuLite Synergy Pocket Micro-pump," *J. Hear. Lung Transplant.*, vol. 32, no. 5, pp. 539–545, 2013.

[106] M. E. Davis, N. a Haglund, N. M. Tricarico, A. Matafonov, D. Gailani, and S. Maltais, "Immediate Recovery of Acquired von Willebrand Syndrome after Left Ventricular Assist Device Explantation: Implications for Heart Transplantation.," *ASAIO J.*, pp. 1–4, 2014.

[107] S. Crow *et al.*, "Comparative analysis of von Willebrand factor profiles in pulsatile and continuous left ventricular assist device recipients.," *ASAIO J.*, vol. 56, no. 5, pp. 441–5, 2010.

[108] C. R. Bartoli, D. J. Restle, D. M. Zhang, M. A. Acker, and P. Atluri, "Pathologic von Willebrand factor degradation with a left ventricular assist device occurs via two distinct mechanisms: Mechanical demolition and enzymatic cleavage," *J. Thorac. Cardiovasc. Surg.*, vol. 149, no. 1, pp. 281–289, 2015.

[109] H. M. Tsai, I. I. Sussman, and R. L. Nagel, "Shear stress enhances the proteolysis of von Willebrand factor in normal plasma.," *Blood*, vol. 83, no. 8, pp. 2171–9, 1994.

[110] C. a Siedlecki, B. J. Lestini, K. K. Kottke-Marchant, S. J. Eppell, D. L. Wilson, and R. E. Marchant, "Shear-dependent changes in the three-dimensional structure of human von Willebrand factor.," *Blood*, vol. 88, no. 8, pp. 2939–50, 1996.

[111] M. Giersiepen, L. J. Wurzinger, R. Opitz, and H. Reul, "Estimation of shear stress-related blood damage in heart valve prostheses - in vitro comparison of 25 aortic valves," *Int. J. Artif. Organs*, vol. 13, no. 5, pp. 300–306, 1990.

[112] T. Zhang *et al.*, "Study of Flow-Induced Hemolysis Using Novel Couette-Type Blood-Shearing Devices," *Artif. Organs*, vol. 35, no. 12, pp. 1180–1187, 2011.

[113] M. Grigioni, C. Daniele, U. Morbiducci, G. D'Avenio, G. Di Benedetto, and V. Barbaro, "The power-law mathematical model for blood damage prediction: Analytical developments and physical inconsistencies," *Artif. Organs*, vol. 28, no. 5, pp. 467–475, 2004.

[114] K. K. Yeleswarapu, J. F. Antaki, M. V Kameneva, and K. R. Rajagopal, "A Mathematical Model for Shear-Induced Hemolysis," *Artif. Organs*, vol. 19, no. 7, pp. 576–582, 1995.

[115] A. Garon and M.-I. Farinas, "Fast three-dimensional numerical hemolysis approximation.," *Artif. Organs*, vol. 28, no. 11, pp. 1016–25, 2004.

[116] D. Arora, M. Behr, and M. Pasquali, "A tensor-based measure for estimating blood damage," *Artif. Organs*, vol. 28, no. 11, pp. 1002–1015, 2004.

[117] H. M. Ezzeldin, M. D. de Tullio, M. Vanella, S. D. Solares, and E. Balaras, "A Strain-

Based Model for Mechanical Hemolysis Based on a Coarse-Grained Red Blood Cell Model," *Ann. Biomed. Eng.*, vol. 43, no. 6, pp. 1398–1409, 2015.

[118] Y. Chen and M. K. Sharp, "A Strain-Based Flow-Induced Hemolysis Prediction Model Calibrated by In Vitro Erythrocyte Deformation Measurements," *Artif. Organs*, vol. 35, no. 2, pp. 145–156, 2011.

[119] H. Yu and S. Engel, "A Review of Hemolysis Prediction Models for Computational Fluid Dynamics," vol. 00, no. 0, 2017.

[120] A. L. Fogelson and K. B. Neeves, "Fluid Mechanics of Blood Clot Formation," *Annu. Rev. Fluid Mech.*, vol. 47, no. 1, 2015.

[121] J. S. Soares, J. Sheriff, and D. Bluestein, "A novel mathematical model of activation and sensitization of platelets subjected to dynamic stress histories," *Biomech. Model. Mechanobiol.*, vol. 12, no. 6, pp. 1127–1141, 2013.

[122] Y. Alemu and D. Bluestein, "Flow-induced platelet activation and damage accumulation in a mechanical heart valve: Numerical studies," *Artif. Organs*, vol. 31, no. 9, pp. 677–688, 2007.

[123] P. D. Goodman, E. T. Barlow, P. M. Crapo, S. F. Mohammad, and K. A. Solen, "Computational model of device-induced thrombosis and thromboembolism," *Ann. Biomed. Eng.*, vol. 33, no. 6, pp. 780–797, 2005.

[124] W. Wang and M. R. King, "Multiscale modeling of platelet adhesion and thrombus growth," *Ann. Biomed. Eng.*, vol. 40, no. 11, pp. 2345–2354, 2012.

[125] Z. Xu, M. Kamocka, M. Alber, and E. D. Rosen, "Computational approaches to studying thrombus development," *Arterioscler. Thromb. Vasc. Biol.*, vol. 31, no. 3, pp. 500–505, 2011.

[126] M. E. Taskin, K. H. Fraser, T. Zhang, C. Wu, B. P. Griffith, and Z. J. Wu, "Evaluation of Eulerian and Lagrangian Models for Hemolysis Estimation," *ASAIO J.*, vol. 58, no. 4, pp. 363–372, 2012.

[127] W. S. Nesbitt *et al.*, "A shear gradient–dependent platelet aggregation mechanism drives thrombus formation," *Nat. Med.*, vol. 15, no. 6, pp. 665–673, 2009.

[128] G. Girdhar and D. Bluestein, "Biological effects of dynamic shear stress in cardiovascular pathologies and devices," *Expert Rev. Med. Devices*, vol. 5, no. 2, p. 167, 2008.

[129] F. R. Menter, "Two-equation eddy-viscosity turbulence models for engineering applications," *AIAA J.*, vol. 32, no. 8, pp. 1598–1605, 1994.

[130] K. H. Fraser, M. E. Taskin, B. P. Griffith, and Z. J. Wu, "The use of computational fluid dynamics in the development of ventricular assist devices.," *Med. Eng. Phys.*, vol. 33, no. 3, pp. 263–280, 2011.

[131] Siemens, *StarCCM+ User Guide*. Munich, Germany, 2018.

[132] D. A. Fedosov, B. Caswell, and G. E. Karniadakis, "A Multiscale Red Blood Cell Model with Accurate Mechanics, Rheology, and Dynamics," *Biophys. J.*, vol. 98, no. 10, pp. 2215–2225, 2010.

[133] T. W. Secomb, B. Styp-Rekowska, and A. R. Pries, “Two-dimensional simulation of red blood cell deformation and lateral migration in microvessels.,” *Ann. Biomed. Eng.*, vol. 35, no. 5, pp. 755–65, 2007.

[134] M. Ju *et al.*, “A review of numerical methods for red blood cell flow simulation,” *Comput. Methods Biomech. Biomed. Engin.*, vol. 18, no. 2, pp. 130–140, 2015.

[135] D. A. Fedosov, H. Noguchi, and G. Gompper, “Multiscale Modeling of Blood Flow: From Single Cells to Blood Rheology,” *Biomech. Model. Mechanobiol.*, vol. 13, no. 2, pp. 239–58, 2014.

[136] S. Chien, “Red cell deformability and its relevance to blood flow.,” *Annu. Rev. Physiol.*, vol. 49, pp. 177–192, 1987.

[137] S. Chien, S. Usami, R. J. Dellenback, M. I. Gregersen, L. B. Nanninga, and M. Mason Guest, “Blood viscosity: Influence of erythrocyte aggregation,” *Science (80-.).*, vol. 157, no. 3790, pp. 829–831, 1967.

[138] O. K. Baskurt, D. Ph, H. J. Meiselman, and D. Sc, “Blood Rheology and Hemodynamics,” *Semin. Thromb. Hemost.*, vol. 29, no. 5, pp. 435–450, 2003.

[139] M. Perschall, J. B. Drevet, T. Schenkel, and H. Oertel, “The Progressive Wave Pump: Numerical Multiphysics Investigation of a Novel Pump Concept With Potential to Ventricular Assist Device Application,” *Artif Organs*, vol. 36, no. 9, pp. E179–E190, 2012.

[140] C.-H. Hsu, H.-H. Vu, and Y.-H. Kang, “The Rheology of Blood Flow in a Branched Arterial System with Three-Dimensional Model: A Numerical Study,” *J. Mech.*, vol. 25, no. 04, pp. N21–N24, 2009.

[141] E. W. Merrill, “Rheology of blood,” *Physiol. Rev.*, vol. 49, no. 4, pp. 836–886, 1969.

[142] X. Song, A. L. Throckmorton, H. G. Wood, J. F. Antaki, and D. B. Olsen, “Computational Fluid Dynamics Prediction of Blood Damage in a Centrifugal Pump,” *Artif. Organs*, vol. 27, no. 10, pp. 938–941, 2003.

[143] J. B. Anderson, H. G. Wood, P. E. Allaire, J. C. Mcdaniel, D. B. Olsen, and B. G., “Numerical studies of blood shear and washing in a continuous flow ventricular assist device,” *ASAIO J.*, vol. 46, no. 4, pp. 486–494, 2000.

[144] A. L. Throckmorton and A. Untaroiu, “CFD analysis of a mag-lev ventricular assist device for infants and children: Fourth generation design,” *ASAIO J.*, vol. 54, no. 4, pp. 423–431, 2008.

[145] F. Menter, “Zonal Two Equation k-w Turbulence Models For Aerodynamic Flows,” in *23rd Fluid Dynamics, Plasmadynamics, and Lasers Conference*, American Institute of Aeronautics and Astronautics, 1993.

[146] X. Song, H. G. Wood, S. W. Day, and D. B. Olsen, “Studies of Turbulence Models in a Computational Fluid Dynamics Model of a Blood Pump,” *Artif. Organs*, vol. 27, no. 10, pp. 935–937, 2003.

[147] P. C. Lu, H. C. Lai, and J. S. Liu, “A reevaluation and discussion on the threshold limit for hemolysis in a turbulent shear flow,” *J. Biomech.*, vol. 34, no. 10, pp. 1361–1364, 2001.

[148] A. M. Sallam and N. H. Hwang, "Human red blood cell hemolysis in a turbulent shear flow: contribution of Reynolds shear stresses.," *Biorheology*, vol. 21, no. 6, pp. 783–797, 1984.

[149] L. Ge, L. P. Dasi, F. Sotiropoulos, and A. P. Yoganathan, "Characterization of hemodynamic forces induced by mechanical heart valves: Reynolds vs. viscous stresses," *Ann. Biomed. Eng.*, vol. 36, no. 2, pp. 276–297, 2008.

[150] J. S. Liu, P. C. Lu, and S. H. Chu, "Turbulence Characteristics Downstream of Bileaflet Aortic Valve Prostheses," *J. Biomech. Eng.*, vol. 122, pp. 118–124, 2000.

[151] A. Aziz, B. C. Werner, K. L. Epting, C. D. Agosti, and W. R. Curtis, "The cumulative and sublethal effects of turbulence on erythrocytes in a stirred-tank model," *Ann. Biomed. Eng.*, vol. 35, no. 12, pp. 2108–2120, 2007.

[152] L. Antiga and D. A. Steinman, "Rethinking turbulence in blood," *Biorheology*, vol. 46, no. 2, pp. 77–81, 2009.

[153] R. A. Malinauskas *et al.*, "FDA Benchmark Medical Device Flow Models for CFD Validation," *ASAIO J.*, 2017.

[154] S. F. C. Stewart *et al.*, "Assessment of CFD Performance in Simulations of an Idealized Medical Device: Results of FDA's First Computational Interlaboratory Study," *Cardiovasc. Eng. Technol.*, vol. 3, no. 2, pp. 139–160, 2012.

[155] J. González, J. Fernández, E. Blanco, and C. Santolaria, "Numerical Simulation of the Dynamic Effects Due to Impeller-Volute Interaction in a Centrifugal Pump," *J. Fluids Eng.*, vol. 124, no. 2, p. 348, 2002.

[156] J. González and C. Santolaria, "Unsteady Flow Structure and Global Variables in a Centrifugal Pump," *J. Fluids Eng.*, vol. 128, no. 5, p. 937, 2006.

[157] K. Majidi, "Numerical Study of Unsteady Flow in a Centrifugal Pump," *J. Turbomach.*, vol. 127, no. 2, p. 363, 2005.

[158] S. J. Sonntag *et al.*, "Simulation of a pulsatile total artificial heart: Development of a partitioned Fluid Structure Interaction model," *J. Fluids Struct.*, vol. 38, pp. 187–204, 2013.

[159] R. J. Adrian, "Particle-Imaging Techniques for Experimental Fluid Mechanics," *Annu. Rev. Fluid Mech.*, vol. 23, no. 1, pp. 261–304, 1991.

[160] H. G. Maas, A. Gruen, and D. Papantoniou, "Particle tracking velocimetry in 3-dimensional flows. Part 1. Photogrammetric determination of particle coordinates," *Exp. Fluids*, vol. 15, no. 2, pp. 133–146, 1993.

[161] G. Ochsner *et al.*, "A novel interface for hybrid mock circulations to evaluate ventricular assist devices," *IEEE Trans. Biomed. Eng.*, vol. 60, no. 2, pp. 507–516, 2013.

[162] S. R. Shah, S. V. Jain, R. N. Patel, and V. J. Lakhera, "CFD for centrifugal pumps: A review of the state-of-the-art," *Procedia Eng.*, vol. 51, no. NUiCONE 2012, pp. 715–720, 2013.

[163] R. Graefe, A. Henseler, and U. Steinseifer, "Multivariate Assessment of the Effect of

Pump Design and Pump Gap Design Parameters on Blood Trauma," *Artif. Organs*, vol. 40, no. 6, pp. 568–576, 2016.

[164] W. K. Chan, Y. W. Wong, Y. Ding, L. P. Chua, and S. C. M. Yu, "Numerical investigation of the effect of blade geometry on blood trauma in a centrifugal blood pump," *Artif. Organs*, vol. 26, no. 9, pp. 785–793, 2002.

[165] H. Yu, G. Janiga, and D. Thévenin, "Computational Fluid Dynamics-Based Design Optimization Method for Archimedes Screw Blood Pumps," *Artif. Organs*, vol. 40, no. 4, pp. 341–352, 2016.

[166] J. Wu, K. Shimmei, K. Tani, K. Niikura, and J. Sato, "CFD-Based Design Optimization for Hydro Turbines," *J. Fluids Eng.*, vol. 129, no. February 2007, pp. 159–168, 2007.

[167] J. Wu, J. F. Antaki, W. R. Wagner, T. a Snyder, B. E. Paden, and H. S. Borovetz, "Elimination of adverse leakage flow in a miniature pediatric centrifugal blood pump by computational fluid dynamics-based design optimization.," *ASAIO J.*, vol. 51, no. 5, pp. 636–643, 2005.

[168] J. Wu, B. E. Paden, H. S. Borovetz, and J. F. Antaki, "Computational fluid dynamics analysis of blade tip clearances on hemodynamic performance and blood damage in a centrifugal ventricular assist device," *Artif. Organs*, vol. 34, no. 5, pp. 402–411, 2009.

[169] J. Wu, J. F. Antaki, J. Verkaik, S. Snyder, and M. Ricci, "Computational Fluid Dynamics-Based Design Optimization for an Implantable Miniature Maglev Pediatric Ventricular Assist Device," *J. Fluids Eng.*, vol. 134, no. April 2012, p. 041101, 2012.

[170] M. Denisov, A. Pugovkin, S. Selishchev, and I. Nesterenko, "The Progress in the Novel Pediatric Rotary Blood Pump Sputnik Development," no. 1, 2018.

[171] S. V. Selishchev and D. V. Telyshev, "Optimisation of the Sputnik-VAD design," *Int. J. Artif. Organs*, vol. 39, no. 8, pp. 407–414, 2016.

[172] X. Song, A. L. Throckmorton, H. G. Wood, J. F. Antaki, and D. B. Olsen, "Quantitative Evaluation of Blood Damage in a Centrifugal VAD by Computational Fluid Dynamics," *J. Fluids Eng.*, vol. 126, no. 3, p. 410, 2004.

[173] T. Yamane, T. Miyamoto, T. Tajima, and K. Yamazaki, "A comparative study between flow visualization and computational fluid dynamic analysis for the Sun Medical centrifugal blood pump," *Artif Organs*, vol. 28, no. 5, pp. 458–466, 2004.

[174] K. H. Fraser, T. Zhang, M. E. Taskin, B. P. Griffith, and Z. J. Wu, "A Quantitative Comparison of Mechanical Blood Damage Parameters in Rotary Ventricular Assist Devices: Shear Stress, Exposure Time and Hemolysis Index," *J. Biomech. Eng.*, vol. 134, no. 8, p. 081002, 2012.

[175] Z. Chen *et al.*, "Flow features and device-induced blood trauma in CF-VADs under a pulsatile blood flow condition: A CFD comparative study," *Int. j. numer. method. biomed. eng.*, vol. 34, p. e2924, 2018.

[176] X. Song, A. L. Throckmorton, H. G. Wood, P. E. Allaire, and D. B. Olsen, "Transient and quasi-steady computational fluid dynamics study of a left ventricular assist device," *ASAIO J.*, vol. 50, no. 5, pp. 410–417, 2004.

[177] T. Masuzawa, A. Ohta, N. Tanaka, Y. Qian, and T. Tsukiya, “Estimation of changes in dynamic hydraulic force in a magnetically suspended centrifugal blood pump with transient computational fluid dynamics analysis,” *J. Artif. Organs*, vol. 12, no. 3, pp. 150–159, 2009.

[178] B. Torner, S. Hallier, M. Witte, and F.-H. Wurm, “Large-Eddy and Unsteady Reynolds-Averaged Navier-Stokes Simulations of an Axial Flow Pump for Cardiac Support,” *ASME Turbine Tech. conf. Expo.*, pp. 1–11, 2017.

[179] “Zurich Heart Project.” [Online]. Available: http://www.hochschulmedizin.uzh.ch/de/projekte/zurichheart.html.

[180] L. Wiegmann *et al.*, “Influence of Standard Laboratory Procedures on Measures of Erythrocyte Damage,” *Front. Physiol.*, vol. 8, p. 731, 2017.

[181] L. Wiegmann *et al.*, “Blood Pump Design Variations and Their Influence on Hydraulic Performance and Indicators of Hemocompatibility,” *Ann. Biomed. Eng.*, vol. 46, p. 417, 2018.

[182] Y. Shapira, M. Vaturi, and A. Sagie, “Hemolysis associated with prosthetic heart valves: a review.,” *Cardiol. Rev.*, vol. 17, no. 3, pp. 121–4, 2009.

[183] J. K. Kirklin *et al.*, “Seventh INTERMACS annual report: 15,000 patients and counting,” *J. Hear. Lung Transplant.*, vol. 34, no. 12, pp. 1495–1504, 2015.

[184] S. M. Cahalan, V. Lukacs, S. S. Ranade, S. Chien, M. Bandell, and A. Patapoutian, “Piezo1 links mechanical forces to red blood cell volume,” *Elife*, vol. 4, no. MAY, pp. 1–12, 2015.

[185] S. Rao, S. Bálint, B. Cossins, V. Guallar, and D. Petrov, “Raman Study of Mechanically Induced Oxygenation State Transition of Red Blood Cells Using Optical Tweezers,” *Biophys. J.*, vol. 96, no. 1, pp. 209–216, 2009.

[186] M. Plebani, “Errors in laboratory medicine and patient safety: The road ahead,” *Clin. Chem. Lab. Med.*, vol. 45, no. 6, pp. 700–707, 2007.

[187] G. Lippi, G. C. Guidi, C. Mattiuzzi, and M. Plebani, “Preanalytical variability: The dark side of the moon in laboratory testing,” *Clin. Chem. Lab. Med.*, vol. 44, no. 4, pp. 358–365, 2006.

[188] E. W. Gunter, B. A. Bowman, S. P. Caudill, D. B. Twite, M. J. Adams, and E. J. Sampson, “Results of an international round robin for serum and whole-blood folate.,” *Clin. Chem.*, vol. 42, no. 10, pp. 1689 –1694, Oct. 1996.

[189] D. J. Quinn *et al.*, “Combined Simulation and Experimental Study of Large Deformation of Red Blood Cells in Microfluidic Systems,” *Ann. Biomed. Eng.*, vol. 39, no. 3, pp. 1041–1050, 2011.

[190] I. I. Katkov and P. Mazur, “Influence of centrifugation regimes on motility, yield and cell assications of mouse spermatozoa,” *J. Androl.*, vol. 19, no. 2, pp. 232–241, 1998.

[191] G. A. Ferraro *et al.*, “Effects of a new centrifugation method on adipose cell viability for autologous fat grafting,” *Aesthetic Plast. Surg.*, vol. 35, no. 3, pp. 341–348, 2011.

[192] B. C. Heng, H. Liu, Z. Ge, and T. Cao, “Mechanical dissociation of human embryonic

stem cell colonies by manual scraping after collagenase treatment is much more detrimental to cellular viability than is trypsinization with gentle pipetting.," *Biotechnol. Appl. Biochem.*, vol. 47, no. Pt 1, pp. 33–37, 2007.

[193] G. Bai, J. S. Bee, J. G. Biddlecombe, Q. Chen, and W. T. Leach, "Computational fluid dynamics (CFD) insights into agitation stress methods in biopharmaceutical development," *Int. J. Pharm.*, vol. 423, no. 2, pp. 264–280, 2012.

[194] S. O. Sowemimo-Coker, "Red Blood Cell Hemolysis During Processing," *Transfus. Med. Rev.*, vol. 16, no. 1, pp. 46–60, 2002.

[195] A. Makhro *et al.*, "Red cell properties after different modes of blood transportation," *Front. Physiol.*, vol. 7, no. JUL, 2016.

[196] O. Baskurt *et al.*, "New guidelines for hemorheological laboratory techniques," *Clin. Hemorheol. Microcirc.*, vol. 42, no. 2, pp. 75–97, 2009.

[197] V. F. Fairbanks, S. C. Ziesmer, and P. C. O'Brien, "Methods for measuring plasma hemoglobin in micromolar concentration compared," *Clin. Chem.*, vol. 38, no. 1, pp. 132–140, 1992.

[198] F. E. Boas, L. Forman, and E. Beutler, "Phosphatidylserine exposure and red cell viability in red cell aging and in hemolytic anemia.," *Proc. Natl. Acad. Sci. U. S. A.*, vol. 95, no. March, pp. 3077–3081, 1998.

[199] H. U. Lutz and A. Bogdanova, "Mechanisms tagging senescent red blood cells for clearance in healthy humans," *Front. Physiol.*, vol. 4, pp. 1–15, 2013.

[200] F. A. Kuypers *et al.*, "Detection of altered membrane phospholipid asymmetry in subpopulations of human red blood cells using fluorescently labeled annexin V.," *Blood*, vol. 87, no. 3, pp. 1179–87, 1996.

[201] J. W. Tukey, "Exploratory Data Analysis," in *Addison-Wesley Series in Behavioral Science: Quantitative Methods*, 1977, pp. 5–23.

[202] Z. Zhang, Y. Chisti, and M. Moo-young, "Effects of the hydrodynamic environment and shear protectants on survival of erythrocytes in suspension," *J. Biotechnol.*, vol. 43, no. 1, pp. 33–40, 1995.

[203] Y. Miao and L. Jiang, "Transient expression of fluorescent fusion proteins in protoplasts of suspension cultured cells," *Nat. Protoc.*, vol. 2, no. 10, pp. 2348–2353, Oct. 2007.

[204] A. Exadactylos, A. J. Geffen, and P. Panagiotaki, "Population structure of Dover sole Solea solea: RAPD and allozyme data indicate divergence in European stocks ," *Mar. Ecol. Prog. Ser.*, vol. 246, pp. 253–264, 2003.

[205] A. Urbina, R. Godoy-Silva, M. Hoyos, and M. Camacho, "Acute hydrodynamic damage induced by SPLITT fractionation and centrifugation in red blood cells," *J. Chromatogr. B*, vol. 1020, pp. 53–61, 2016.

[206] M. V Kameneva, M. J. Watach, and H. S. Borovetz, "Gender difference in rheologic properties of blood and risk of cardiovascular diseases.," *Clin. Hemorheol. Microcirc.*, vol. 21, pp. 357–363, 1999.

[207] S. P. Sutera *et al.*, "Age-related changes in deformability of human erythrocytes," *Blood*, vol. 65, no. 2, pp. 275–282, 1985.

[208] D. Sakota *et al.*, "Mechanical damage of red blood cells by rotary blood pumps: Selective destruction of aged red blood cells and subhemolytic trauma," *Artif. Organs*, vol. 32, no. 10, pp. 785–791, 2008.

[209] A. Bogdanova, A. Makhro, J. Wang, P. Lipp, and L. Kaestner, "Calcium in red blood cells-a perilous balance," *Int. J. Mol. Sci.*, vol. 14, no. 5, pp. 9848–9872, 2013.

[210] A. G. Macdonald, "The effects of pressure on the molecular structure and physiological functions of cell membranes," *Phil. Trans. R. Soc. L.*, vol. 304, pp. 47–68, 1984.

[211] N. J. Kim, C. Diao, K. H. Ahn, S. J. Lee, M. V. Kameneva, and J. F. Antaki, "Parametric study of blade tip clearance, flow rate, and impeller speed on blood damage in rotary blood pump," *Artif. Organs*, vol. 33, no. 6, pp. 468–474, 2009.

[212] U. Morbiducci *et al.*, "Blood damage safety of prosthetic heart valves. Shear-induced platelet activation and local flow dynamics: A fluid-structure interaction approach," *J. Biomech.*, vol. 42, no. 12, pp. 1952–1960, 2009.

[213] S. Boës, G. Ochsner, R. Amacher, A. Petrou, M. Meboldt, and M. Schmid Daners, "Control of the fluid viscosity in a mock circulation," *Artif. Organs*, 2017.

[214] J. D. Schmitto, J. S. Hanke, S. V. Rojas, M. Avsar, and A. Haverich, "First implantation in man of a new magnetically levitated left ventricular assist device (HeartMate III)," *J. Hear. Lung Transplant.*, vol. 34, no. 6, pp. 858–860, 2015.

[215] D. Bluestein, K. B. Chandran, and K. B. Manning, "Towards non-thrombogenic performance of blood recirculating devices," *Ann. Biomed. Eng.*, vol. 38, no. 3, pp. 1236–1256, 2010.

[216] C. Bludszuweit, "Three Dimensional Numerical Prediction of Stress Loading of Blood Particles in a Centrifugal Pump," *Artif. Organs*, vol. 19, no. 7, pp. 590–596, 1995.

[217] G. Heuser and R. Opitz, "A Couette viscometer for short time shearing of blood.," *Biorheology*, vol. 17, no. 1–2, pp. 17–24, 1980.

[218] P. Hochareon, K. B. Manning, A. a Fontaine, J. M. Tarbell, and S. Deutsch, "Correlation of in vivo clot deposition with the flow characteristics in the 50 cc penn state artificial heart: a preliminary study.," *ASAIO J.*, vol. 50, no. 6, pp. 537–542, 2004.

[219] T. S. Dewitz, T. C. Hung, R. R. Martin, and L. V McIntire, "Mechanical trauma in leukocytes.," *J. Lab. Clin. Med.*, vol. 90, no. 4, pp. 728–736, Oct. 1977.

[220] J. F. Antaki, C. G. Diao, F. J. Shu, J. C. Wu, R. Zhao, and M. V. Kameneva, "Microhaemodynamics within the blade tip clearance of a centrifugal turbodynamic blood pump," *Proc. Inst. Mech. Eng. Part H J. Eng. Med.*, vol. 222, no. 4, pp. 573–581, 2008.

[221] T. Krabatsch *et al.*, "Heartmate 3 fully magnetically levitated left ventricular assist device for the treatment of advanced heart failure-1 year results from the CE mark trial," *J. Cardiothorac. Surg.*, vol. 12, no. 23, p. S9, 2017.

[222] J. G. Rogers *et al.*, "Intrapericardial Left Ventricular Assist Device for Advanced Heart

Failure," *N. Engl. J. Med.*, vol. 376, no. 5, pp. 451–460, 2017.

[223] I. Netuka *et al.*, "Evaluation of von Willebrand factor with a fully magnetically levitated centrifugal continuous-flow left ventricular assist device in advanced heart failure," *J. Hear. Lung Transplant.*, vol. 35, no. 7, pp. 860–867, 2016.

[224] S. Gupta *et al.*, "Normalisation of haemodynamics in patients with end-stage heart failure with continuous-flow left ventricular assist device therapy," *Hear. Lung Circ.*, vol. 23, no. 10, pp. 963–969, 2014.

[225] F. M. Colacino, F. Moscato, F. Piedimonte, M. Arabia, and G. A. Danieli, "Left ventricle load impedance control by apical VAD can help heart recovery and patient perfusion; a numerical study," *ASAIO J.*, vol. 53, pp. 263–277, 2007.

[226] D. Burkhoff *et al.*, "Left Atrial Decompression Pump for Severe Heart Failure With Preserved Ejection Fraction: Theoretical and Clinical Considerations," *JACC Hear. Fail.*, vol. 3, no. 4, pp. 275–282, 2015.

[227] L. Fresiello, B. Meyns, A. Di Molfetta, and G. Ferrari, "A model of the cardiorespiratory response to aerobic exercise in healthy and heart failure conditions," *Front. Physiol.*, vol. 7, no. JUN, pp. 1–17, 2016.

[228] F. Moscato, C. Wirrmann, M. Granegger, F. Eskandary, D. Zimpfer, and H. Schima, "Use of continuous flow ventricular assist devices in patients with heart failure and a normal ejection fraction: a computer-simulation study.," *J. Thorac. Cardiovasc. Surg.*, vol. 145, no. 5, pp. 1352–8, 2013.

[229] N. Westerhof, J.-W. Lankhaar, and B. E. Westerhof, "The arterial Windkessel.," *Med. Biol. Eng. Comput.*, vol. 47, no. 2, pp. 131–41, Feb. 2009.

[230] M. Granegger, F. Moscato, F. Casas, G. Wieselthaler, and H. Schima, "Development of a pump flow estimator for rotary blood pumps to enhance monitoring of ventricular function," *Artif. Organs*, vol. 36, no. 8, pp. 691–699, 2012.

[231] F. Moscato, G. A. Danieli, and H. Schima, "Dynamic modeling and identification of an axial flow ventricular assist device.," *Int. J. Artif. Organs*, vol. 32, no. 6, pp. 336–43, 2009.

[232] W. E. Cohn, I. D. Gregoric, and O. H. Frazier, "Reinforcement of Left Ventricular Assist Device Outflow Grafts to Prevent Kinking," *Ann. Thorac. Surg.*, vol. 84, no. 1, pp. 301–302, 2007.

[233] M. M. Faghih and M. K. Sharp, "Extending the Power-Law Hemolysis Model to Complex Flows," *J. Biomech. Eng.*, vol. 138, no. 12, p. 124504, 2016.

[234] M. V Kameneva, G. W. Burgreen, K. Kono, B. Repko, J. F. Antaki, and M. Umezu, "Effects of turbulent stresses upon mechanical hemolysis: experimental and computational analysis.," *ASAIO J.*, vol. 50, no. 5, pp. 418–423, 2004.

[235] X. Song, H. G. Wood, and D. Olsen, "Computational Fluid Dynamics (CFD) study of the 4th generation prototype of a continuous flow Ventricular Assist Device (VAD).," *J. Biomech. Eng.*, vol. 126, no. 2, pp. 180–187, 2004.

[236] H. Houng *et al.*, "The Effect of Shear Stress on the Size , Structure , and Function of Human von Willebrand Factor," *Artif. Organs*, vol. 38, no. 9, pp. 741–750, 2014.

[237] D. Bluestein, “Towards optimization of the thrombogenic potential of blood recirculating cardiovascular devices using modeling approaches,” *Expert Rev. Med. Devices*, vol. 3, no. 3, pp. 267–270, 2006.

[238] J. Friend and L. Yeo, “Fabrication of microfluidic devices using polydimethylsiloxane,” *Biomicrofluidics*, vol. 4, no. 2, pp. 1–5, 2010.

[239] G. M. Whitesides, “The origins and the future of microfluidics.,” *Nature*, vol. 442, no. 7101, pp. 368–73, 2006.

[240] F. Consolo *et al.*, “Microfluidic approaches for the assessment of blood cell trauma: a focus on thrombotic risk in mechanical circulatory support devices,” vol. 00, no. 00, 2016.

[241] G. Minetti *et al.*, “Red cell investigations: Art and artefacts,” *Blood Rev.*, vol. 27, no. 2, pp. 91–101, 2013.

[242] R. A. Freitas Jr., “Basic Capabilities,” in *Nanomedicine, Volume I*, Georgetown TX: Landes Bioscience, 1999.

[243] S. J. Hostetter and C. B. Andreasen, *Evaluation of Erythrocytes*. Elsevier Inc., 2004.

[244] N. K. Mondal, E. Sorensen, N. Hiivala, E. Feller, B. Griffith, and Z. J. Wu, “Oxidative stress, DNA damage and repair in heart failure patients after implantation of continuous flow left ventricular assist devices.,” *Int. J. Med. Sci.*, vol. 10, no. 7, pp. 883–93, 2013.

[245] D. A. Pascual-Figal *et al.*, “Red blood cell distribution width predicts long-term outcome regardless of anaemia status in acute heart failure patients,” *Eur. J. Heart Fail.*, vol. 11, no. 9, pp. 840–846, 2009.

[246] W.-T. Wu, F. Yang, J. Wu, N. Aubry, M. Massoudi, and J. F. Antaki, “High fidelity computational simulation of thrombus formation in Thoratec HeartMate II continuous flow ventricular assist device,” *Sci. Rep.*, vol. 6, no. December, pp. 1–11, 2016.

[247] K. Wong *et al.*, “Intraventricular flow patterns and stasis in the LVAD-assisted heart,” *J. Biomech.*, vol. 47, no. 6, pp. 1485–1494, 2014.

[248] J. Zhang *et al.*, “Computational and experimental evaluation of the fluid dynamics and hemocompatibility of the centrimag blood pump,” *Artif. Organs*, vol. 30, no. 3, pp. 168–177, 2006.

[249] D. A. Fedosov, M. Dao, G. E. Karniadakis, and S. Suresh, “Computational biorheology of human blood flow in health and disease,” *Ann. Biomed. Eng.*, vol. 42, no. 2, pp. 368–387, 2014.

[250] T. AlMomani, H. S. Udaykumar, J. S. Marshall, and K. B. Chandran, “Micro-scale dynamic simulation of erythrocyte-platelet interaction in blood flow,” *Ann. Biomed. Eng.*, vol. 36, no. 6, pp. 905–920, 2008.

[251] M. Gusenbauer *et al.*, “Cell Damage Index as Computational Indicator for Blood Cell Activation and Damage,” *Artif. Organs*, vol. 00, no. 2, 2018.

[252] A. P. Yoganathan, Z. He, and S. Casey Jones, “Fluid mechanics of heart valves,” *Annu. Rev. Biomed. Eng.*, vol. 6, pp. 331–362, 2004.

8 Curriculum Vitae

Name: WIEGMANN

Vornamen: Lena Alexandra

Geburtsdatum: 06.06.1990

Heimatort: Zürich ZH und Deutschland

Ausbildung

2014-2018	Doktorandin, Physiologisches Institut, Universität Zürich
2012-2014	Master of Science ETH Maschinenbau, D-MAVT, ETH Zürich Masterarbeit: „Development of a multi-scale simulation framework for bone failure prediction“
2008-2011	Bachelor of Science ETH Maschinenbau, D-MAVT, ETH Zürich
2004-2008	Mathematisch- Naturwissenschaftliches Gymnasium Rämibühl, Zürich

Publikationsliste

Wiegmann L, Boës S, de Zélicourt D, Thamsen B, Schmid Daners M, Meboldt M and Kurtcuoglu V, “Blood Pump Design Variations and Their Influence on Hydraulic Performance and Indicators of Hemocompatibility”, *Ann. Biomed. Eng.*, vol 46, p. 417, 2018.

Wiegmann L, de Zélicourt D, Speer O, Muller A, Goede JS, Seifert B and Kurtcuoglu V, “Influence of Standard Laboratory Procedures on Measures of Erythrocyte Damage”, *Front. Physiol.*, vol. 8, p. 731, 2017.